Radioactive Particle Tracking in a Stirred Tank using SPECT

J. Grasmeijer

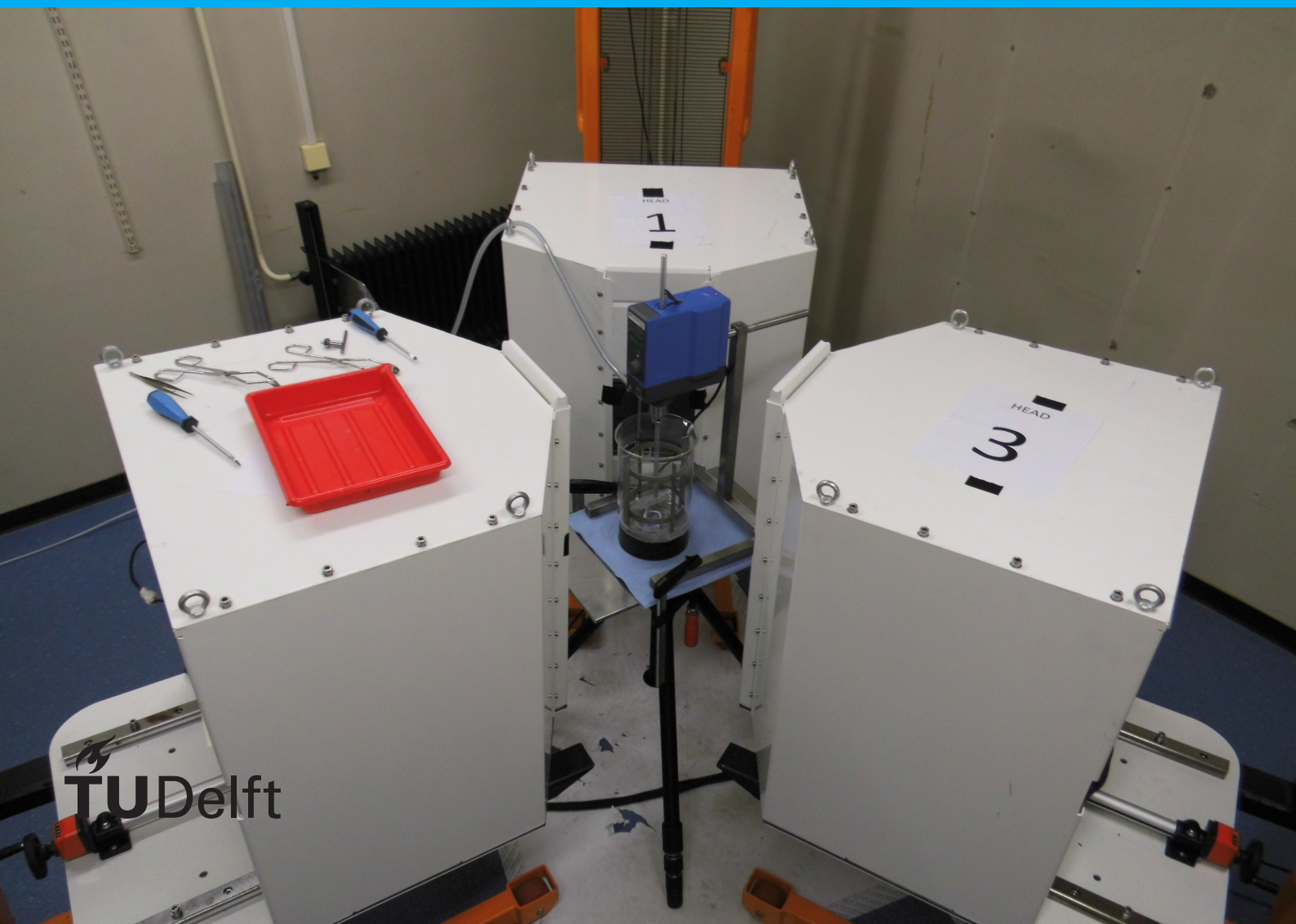

TU Delft

Radioactive Particle Tracking in a Stirred Tank using SPECT

by

J. Grasmeijer

to obtain the degree of Master of Science
at the Delft University of Technology,
to be defended publicly on Friday September 15, 2017 at 14:30.

Student number:	4162781	
Project duration:	October 17, 2016 – September 15, 2017	
Thesis committee:	Prof. dr. R. F. Mudde,	TP/ChemE/TU Delft, supervisor
	Dr. eng. L. Portela,	TP/ChemE/TU Delft
	Dr. ir. M. Goorden,	RST/TU Delft

An electronic version of this thesis is available at `http://repository.tudelft.nl/`.

TU Delft Delft University of Technology

Preface

Since I would not have been able to get this far all on my own, I would like to express my gratitude to some people who helped me during my Master's Thesis Project. First of all I want to thank Prof. dr. Robert F. Mudde for being my supervisor and provide me with advice whenever I needed it. I also want to thank Evert Wagner with whom I performed all of the experiments and thought of the best way to carry them out. Further I want to thank Jos Thieme for lending me some of his equipment, Reinier den Oudsten for making and helping design some of the equipment I needed, Mehmet Sarilar for arranging the activation of the sources and Henk van Doorn for checking the activity of the sources and for storing them afterwards.

J. Grasmeijer
Delft, September 2017

Abstract

Multiphase flows are often opaque. This makes it hard to obtain experimental data to expand our knowledge about them. Even doing small scale experiments is hard, since most techniques that are used to investigate fluid flows use visible light. Therefore new techniques are being developed. One of them is Radioactive Particle Tracking using Single Photon Emission Computed Tomography, better known as SPECT. SPECT is already used for medical purposes, like locating tumors.

In this research we investigated with what accuracy a radioactive tracer particle, emitting gamma rays, can be tracked while moving in a stirred tank filled with 2.5 L of water. Therefore we did some experiments using a 2 mm polystyrene sphere with a golden core. The gold is activated in the reactor of the Reactor Institute Delft (RID) of the TU Delft, after which it will start to emit gamma rays. The gamma rays are detected by three gamma cameras placed around the tank. Each has a collimator with a cross slit in front of the detector plate, to obtain information about the location of the particle, such that by combining the information from the three detectors, its position can be reconstructed. First we did an experiment with a cobalt source, with a low activity, at multiple fixed positions in air, to test the setup. After that we did some experiments with the particle with gold, with a high activity, at multiple fixed positions in air, moving along a known circular trajectory in water and when moving freely in a stirred tank. The last two experiments are also carried out with the tank being aerated.

We found out that the inaccuracy in the reconstructions increases when: the tracer particle is positioned farther away from the center of the setup, the frame rate that is used is increased or the velocity of the tracer particle increases. The error ranges from 0.5 up to 4 mm depending on the settings. The injection of air bubbles at the bottom of the tank with different air flow rates, did not seem to influence the accuracy. Although the accuracy is not that high, there are still a lot of improvements that can be made in order to increase the accuracy.

Contents

Acronyms

LDV Laser Doppler Velocimetry

MRI Magnetic Resonance Imaging

MRV Magnetic Resonance Velocimetry

PEPT Positron Emission Particle Tracking

PET Positron Emission Tomography

PIV Particle Imaging Velocimetry

PMT Photomultiplier tube

PTV Particle Tracking Velocimetry

RPT Radioactive Particle Tracking

SPECT Single Photon Emission Computed Tomography

X-PTV X-ray Particle Tracking Velocimetry

List of symbols

Alphanumeric

A Activity of radioactive source

A_0 Initial activity of radioactive source

a Proportionality constant

B Width of baffles

C Clearance of stirrer above bottom of tank

C_{aer} Clearance of aerator above bottom of tank

D Diameter of stirrer

$D_{aer,h}$ Diameter of circle on which the holes are positioned in the aerator ring

$D_{aer,in}$ Inner diameter of aerator ring

$D_{aer,out}$ Outer diameter of aerator ring

D_{bolt} Diameter of bolt fastening the stirrer to the shaft

D_{disk} Diameter of stirrer disk

D_{shaft} Diameter of the stirrer shaft

d_p Particle diameter

H Water height in the tank

E_b Binding energy

E_e Kinetic energy of electron

E_γ Energy of gamma photon

E'_γ Energy of scattered gamma photon

F Frame rate

Fl Flow number

Fl_g Gas flow number

Fr Froude number

g Gravitational acceleration

HVL Half value layer

L Length of stirrer blades

m_e Electron rest mass

N Rotational speed of stirrer (flow related) / Number of radioactive nuclei (radiation related)

N_0 Initial number of radioactive nuclei present in source

N_{sj} Just suspended rotational speed of stirrer

N_{sjg} Just suspended rotational speed of stirrer when system is gassed

Po Power number

R Radius at which source is rotating

Re Reynolds number

S Zwietering constant

St Stokes number

T Tank diameter (flow related) / Transmittance (radiation related)

t Time that has passed

th Thickness of a layer of material

th_{aer} Diameter of aerator pipe

th_b Thickness of stirrer blades

th_d Thickness of stirrer disk

u Velocity of the fluid

v Velocity of the particle

W Width of stirrer blades

X Mass ratio between solid matter and the liquid times 100

(x,y,z) The coordinates of the chosen coordinate system

(x',y',z') The coordinates of the coordinate system of the traversing device

Z Atomic number

Greek

ΔN_{js} Change in just suspended rotational speed of stirrer by adding gas

η Kolmogorov length scale

θ Scattering angle

μ Dynamic viscosity (flow related) / Linear attenuation coefficient (radiation related)

ν Kinematic viscosity

ρ_f Fluid density

ρ_l Liquid density

ρ_p Particle density

τ Particle response time

τ_f Characteristic time scale of the flow

τ_η Kolmogorov time scale

ϕ_f Fluid flow rate

ϕ_{air} Air flow rate

1 Introduction

Fluid flows have been studied for centuries. During this time various techniques have been developed, each time trying to improve the accuracy or making it possible to study new types of flows. Nowadays we have Particle Image Velocimetry (PIV), Particle Tracking Velocimetry (PTV), Magnetic Resonance Velocimetry (MRV) and Laser Doppler Velocimetry (LDV). Except for MRV, all of them use visible light. This makes these techniques unsuitable for investigating multiphase flows. Multiphase flows often contain small solid particles and/or bubbles, making the flow opaque, disabling visible light of getting through. An important example of such a multiphase flow are bioreactors. These are for instance used for fermentation, where the vessel is filled with a substance in which all kinds of biochemical reactions are happening involving microorganisms. Adequate mixing of this substance is often very important, to keep the mixture homogeneous and in some cases the air bubbles fully dispersed. This is necessary to keep the microorganisms alive and for the right reactions to happen. This will also make the reactions go faster and thus increasing the production rate. These reactors are often very large, up to 100,000 L, and the flow inside is very complex due to all the different kinds of matter in different states, which makes it also opaque. Because of that there is little knowledge about what is locally happening inside the reactor.

Therefore new techniques are being developed to do small scale experiments. Such as X-ray Particle Tracking Velocimetry (X-PTV), Position Emission Particle Tracking (PEPT) and Radioactive Particle Tracking (RPT). We will do some experiments with RPT using Single Photon Emission Computed Tomography (SPECT). SPECT is also used for medical purposes, for instance to find tumors e.g., by injecting gamma-emitting particles in the blood, which will bind to the tissue of the tumors. The gamma radiation can be detected outside the body, making it possible to locate tumors without the need of surgery. In a similar way it can be used to track radioactive particles following a fluid flow.

The technique of RPT using SPECT is already used by several students doing their thesis. Among them Noordman [24] and Bechan [1], who used it to investigate fluidized beds. Noordman was one of the first to use the radioactive tracer particle we will be using. Bechan investigated the performance of a new collimator which we also will be using. They have shown that is it possible to track a particle in a fluidized bed. With our research we will try to answer to following research question:

What accuracy can be achieved when applying Radioactive Particle Tracking using SPECT in a Stirred Tank filled with water?

And the following subquestions:

What influence does the position of the tracer particle have on the accuracy of the Radioactive Particle Tracking?

What influence does the frame rate have on the accuracy of the Radioactive Particle Tracking?

What influence does the velocity of the tracer particle have on the accuracy of the Radioactive Particle Tracking?

What influence does aeration of the tank have on the accuracy of the Radioactive Particle Tracking?

Therefore we will test the technique by doing some experiments in a stirred tank filled with 2.5 L of water. For convenience we will do our experiments with water. As radioactive tracer particle we will be using a 2 mm polystyrene particle with an golden core. The gold will be irradiated with neutrons in the reactor of the Reactor Institute Delft (RID) of the TU Delft, after which it will start to emit gamma rays. To detect the gamma rays, we will use three gamma cameras, placed around the tank. Each has a collimator with a cross slit placed in front of it. Combining the information from the three detectors will lead to a reconstructed position of the tracer particle. Dividing the measurement into time frames, makes it possible to follow the particle in time. We will do three types of experiments, one where the particle is not moving, one where the particle is moving along a known circular trajectory and one where the particle is moving freely in the stirred tank. The first two experiments are necessary to obtain knowledge about the error that will be made in the reconstructions, since therefore we need to know where the particle actually is. In the last experiment we do not have this information. Additionally the last two of the experiments, with a moving source in water, are repeated with the tank being aerated.

In the remainder of the report we will first provide the required theoretical knowledge. Ranging from different flow patterns to the radioactive tracer particle and the detection of its radiation. Subsequently we will discuss the experiments that were carried out and what is needed for that. Then the methods that are used for the post-processing and the reconstruction are explained and at last we will discuss our results, draw some conclusions and present our recommendations.

2

Theory

2.1. Flow in a non-aerated, stirred tank

The flow pattern of a non-aerated, stirred tank is shown in Figure 2.1. The tank is cylindrical and vertically mounted. The shaft of the stirrer is centered vertically in the tank. The impeller used is a flat blade disc turbine, also known as a Rushton turbine. The turbine in the figure, however, has four blades, while we will use one with of six blades instead. This will be the case in the remainder of the report. The flow patterns are very similar though. As can be seen in the figure on the left, the turbine draws water from above and below, pushing it radially outwards against the wall, which in turn pushes part of the water upwards and part of it downwards along the wall. Creating an upper and lower circulation. Along the walls four baffles are placed. These prevent the flow from becoming one big vortex, as in Figure 2.2, which is not very efficient for mixing. This phenomenon is called gross vortexing. The baffles create turbulence, enhancing the mixing [7, 29].

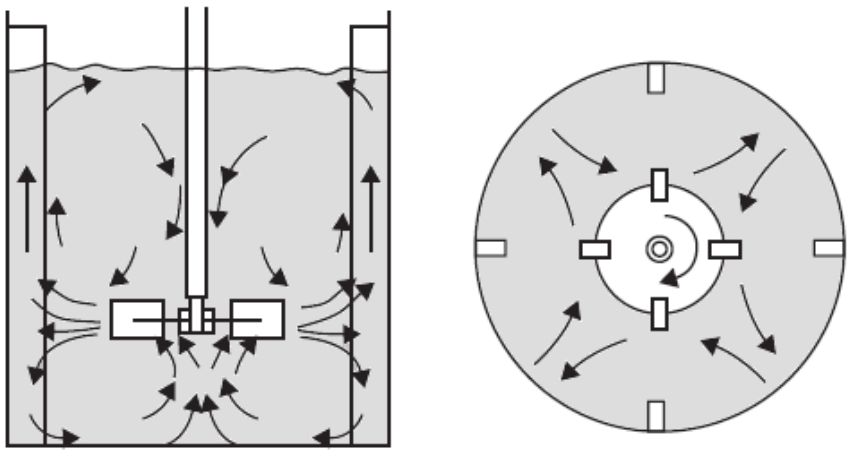

Figure 2.1: Non-aerated flow pattern in a baffled tank stirred by a Rushton turbine with four blades, with on the left a side view and on the right a top view [29].

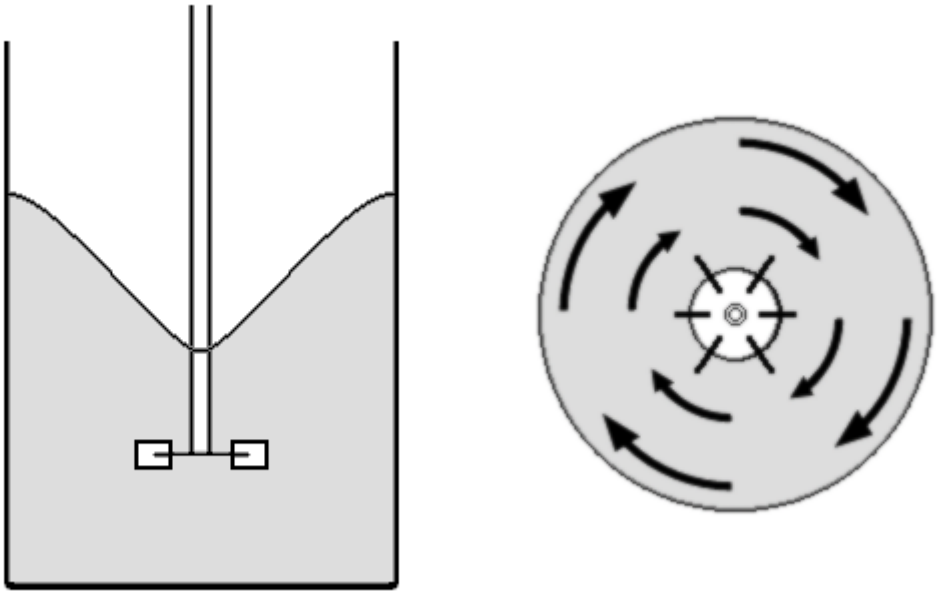

Figure 2.2: Gross vortexing in an unbaffled tank, with on the left a side view and on the right a top view.

2.2. Flow in an aerated, stirred tank

Now we add an aerator to the previous situation, positioned below the stirrer. The aerator is made of a pipe with one end bent in a circle and with little holes on top, through which air is injected into the tank. The flow pattern of an aerated, stirred tank will depend on the air flow rate, ϕ_{air}, and on the rotational speed of the stirrer, N. The different patterns are shown in Figure 2.3, with from left to right an increasing stirrer speed or decreasing air flow rate. The pattern in Figure 2.3a is called flooding. The velocity of the bubbles is too high for the stirrer to disperse them. A column of air will be formed, dominating the flow pattern. When the pattern is less dominated by the air flow (see Figure 2.3b), by increasing the stirrer speed or decreasing the air flow rate, the bubbles will, after passing the stirrer, spread radially outwards while going up. When the water flow starts to dominate (see Figure 2.3c), the bubbles will no longer move up while passing the stirrer, but will be pushed out radially. Some of the bubbles also start recirculating in the lower region. Some of the bubbles in the upper region move radially inward while rising, redistributing themselves evenly. This pattern is called loading. When the water flow becomes even more dominant (see Figure 2.3d), more and more bubbles start to recirculate in the lower region. The stirrer also start to pull bubbles down from the upper region, creating a second recirculation. Now the bubbles are fully dispersed, except for the area right below the aerator. [19, 22].

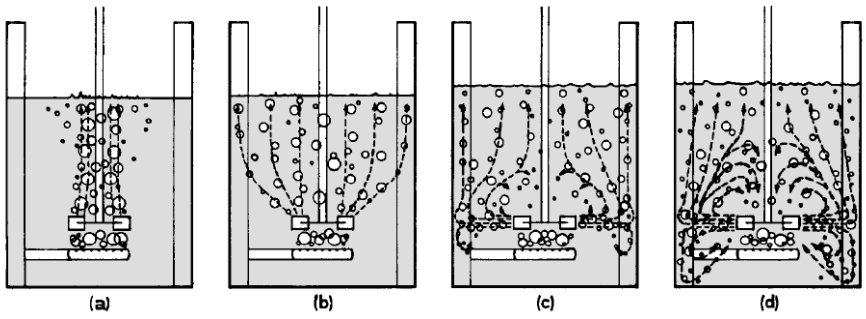

Figure 2.3: Aerated flow pattern in a baffled tank stirred by a Rushton turbine, with from left to right an increasing stirrer speed or decreasing air flow rate. Where (a) is called flooding, (b) is the transition between flooding and loading, (c) is loading and (d) is fully dispersed [19].

2.3. Important dimensionless numbers for stirred tank design

In this section we will list the most important dimensionless numbers used in the design of stirred tanks. The Reynolds number, Re, of the flow in stirred tanks is defined as:

$$Re = \frac{\rho_f u D}{\mu} = \frac{\rho_f N D^2}{\mu} = \frac{N D^2}{\nu} \tag{2.1}$$

where ρ_f is the density of the fluid, N is the rotational speed, D is the diameter of the stirrer, u is a typical velocity of the fluid, in this case equal to ND, μ is the dynamic viscosity and ν is the kinematic viscosity. Re is the ratio between the inertial and viscous forces. The Power number, Po, is defined as:

$$Po = \frac{P}{\rho_f N^3 D^5} \tag{2.2}$$

where P is the power input of the stirrer. Po is the ratio between the power input and the power actually being transferred to the flow in the form of kinetic energy. This way being a measure for the friction in the system. The Froude number, Fr, is defined as:

$$Fr = \frac{D N^2}{g} \tag{2.3}$$

where g is the gravitational acceleration. Fr is the ratio between inertial and gravitational forces. This number is only of importance when gross vortexing occurs, so for Re higher than 300 and tanks without baffles. The flow number, Fl, is defined as:

$$Fl = \frac{\phi_f}{N D^3} \tag{2.4}$$

where ϕ_f is the fluid flow rate, which can be calculated integrating the outflow in the discharge area of the stirrer. Fl is the ratio between the fluid flow rate and the pumping capacity of the stirrer. The gas flow number, Fl_g, is defined as:

$$Fl_g = \frac{\phi_{air}}{N D^3} \tag{2.5}$$

where ϕ_{air} is the air flow rate of the aerator. Fl_g is the ratio between the air flow rate and the pumping capacity of the stirrer [7, 14]. All these numbers give a global interpretation of what is happening in the flow. To improve the performance of mixing in stirred tanks more detailed information is necessary. To gain more locally specific information of the flow, velocimetry methods can be used.

2.4. Velocimetry methods

There are many techniques developed to do velocity measurements of flow dynamics. The most commonly used methods will be discussed here. Before doing so, we will look into two types of categorizations that can be made. The first makes a distinction between invasive and non-invasive techniques. Invasive techniques are based on putting some kind of probe inside the flow, to measure the local flow velocity. A big disadvantage of this is that flow is influenced by the presence of the probe. The techniques described in this paragraph will all be non-invasive. Meaning that the flow is not influenced by the flow measurement. The second categorization distinguishes two other types of groups: Eulerian and Lagrangian methods. Eulerian methods determine the velocity of the flow inside certain volumes fixed in space measured at multiple instants in time. So at different instants in time, we will know the velocity of the flow at fixed positions in space, while a different volume of fluid will be inside each volume of interest (unless the velocity inside has stayed zero in the meantime). Lagrangian methods determine the velocity of certain particles in the flow (tracer particles or fluid particles themselves) while following them at multiple instants in time. So at different instants in time, we will know the velocity of the flow at changing positions in space, since we are following particles which will be at different positions for different instants in time (unless its velocity has stayed zero in the meantime) [2].

2.4.1. Eulerian methods

Particle Imaging Velocimetry (PIV) is a method where the flow is seeded with tracer particles. One plane inside the flow is illuminated twice by a light sheet within a short period of time. The light scattered from the particles is detected, for instance by a CCD camera. The recordings are divided into subareas. For each subarea a displacement vector is determined from the displacement between two subsequent recordings of the particles inside the subarea, using auto- and cross-correlations. Together with the time delay between the two recordings, the velocity parallel to the plane can be determined for each subarea. For this technique it is beneficial to have the tracer particles homogeneously distributed through the flow, such that in each subarea there are multiple particles present to calculate the displacement with [13].

Laser Doppler Velocimetry (LDV) is an interferometric method used to measure one velocity component at a very specific point in space. To measure all three components simultaneously, multiple systems can be combined. This technique uses two intersecting laser beams, often originating from the same source. Particles passing through the intersection volume will scatter some of the light. A photodetector will register the light scattered in its direction. Since the particles are moving, the scattered light will be Doppler shifted. The measured frequency will depend on the angle between the incident beam and the velocity of the particle. Since this angle will be different for each of the two incident beams, there will be two frequencies measured. The difference between the frequencies is used to determine the velocity of the particle [30].

2.4.2. Lagrangian methods

Particle Tracking Velocimetry (PTV) goes essentially the same as PIV, illuminating tracer particles in the plane of interest, making two subsequent recordings and looking at the displacement of the particles. The difference is that the recordings are not divided into subareas, but the displacement of each particle is determined individually using the information of the neighborhood. This way creating velocity vectors parallel to the plane for each particle. For this technique there is no need for a homogeneous distribution of the particles [28].

Magnetic Resonance Velocimetry (MRV) uses the same Magnetic Resonance Imaging (MRI) scanners as are used in hospitals. These scanners generate a strong magnetic field. Nuclei with a non-zero magnetic moment will start to align with the external field and precessing at a certain frequency, called the Larmor frequency. The nuclei of hydrogen atoms, containing only a proton, are used for the imaging, since most biological tissues contain water. So do many fluid flows. After the alignment, the nuclei are excited by a radio frequency pulse, bringing their spins into the plane perpendicular to the external field. After the pulse, the spins will align again with the external field after some time. The time varying field from the changing spins induce voltages in the receiver coils, from which an image can be made. To measure the flow velocity one can look at the phase of the signal when applying a gradient in the magnetic field [3].

X-ray Particle Tracking Velocimetry (X-PTV) is based on the absorption of X-rays by the tracer particle. A beam of X-rays is created by a source outside the system and a detector at the other side of the system detects the X-rays passing through. The pixels on a line with the source and the particle, will receive a lower intensity, due to the absorption by the particle, and thus show a dark spot. Using multiple sources and detectors around the system makes it possible to reconstruct the position of the tracer particle. Huijs [12] has investigated this technique during his thesis.

Positron Emission Particle Tracking (PEPT) is derived from the medical imaging technique Positron Emission Tomography (PET). PEPT uses a tracer particle containing a radioactive isotope which decays via emitting a positron. The positron will annihilate with an electron in the nearby surroundings, generating two photons of 511 keV moving away from each other with an angle of 180°. These photons will be measured simultaneously by two opposing gamma detectors placed around the tank. With these two detections a line can be drawn on which the particle should be positioned. Using multiple of these lines from other annihilation events will make it possible to triangulate the position of the particle. Annihilations within a very short time interval should be used for this, such that the particle almost did not moved [4].

Radioactive Particle Tracking (RPT) is derived from the medical imaging technique Single Photon Emission Computed Tomography (SPECT). RPT uses a tracer particle containing a radioactive isotope which decays among other things via emitting a single gamma photon. The photons are recorded by gamma detectors placed around the tank. There are multiple ways of reconstructing the position of the particle. One is to do a calibration with the particle at various known positions and monitor the number of detections per unit of time for each detector. From this a relation can be determined between the number of detections per unit of time on the detector and the distance between the particle and the detector. Now when measuring, each detector will measure a certain amount of detections in a certain time interval, which can be translated to a certain distance from the detector. Using the knowledge from multiple detectors will result in a reconstructed

position of the particle. The second way is by using collimators in front of the detectors. The collimator will only let through photons coming from a certain direction, creating an image on the detector. The position of the image contains information about the position of the particle. Again using the knowledge from multiple detectors will result in a reconstructed position.

Since RPT using collimators is the technique that will be used in our experiments, some of the aspects will be discussed to a greater extent in the following sections.

2.5. Tracer particle

It all starts with a particle which is attempted to be tracked while it is moving in a fluid flow. The ideal tracer particle would exactly follow the flow. A measure for how good a real tracer particle follows the flow can be given with the Stokes number, St, which is defined as the ratio between the response time of the particle, τ, and the characteristic time of the flow, τ_f. With the following definitions:

$$\tau = \frac{1}{18}\frac{\rho_p - \rho_f}{\rho_f}\frac{d_p^2}{\nu} \tag{2.6}$$

where ρ_p is the density of the particle, ρ_f is the density of the fluid, d_p is the diameter of the particle and ν is the kinematic viscosity of the fluid. And:

$$\tau_f = \tau_\eta \tag{2.7}$$

where τ_η is the Kolmogorov time scale. This results in:

$$St = \frac{\tau}{\tau_f} = \frac{1}{18}\frac{\rho_p - \rho_f}{\rho_f}\frac{d_p^2}{\nu\tau_\eta} = \frac{1}{18}\frac{\rho_p - \rho_f}{\rho_f}\left(\frac{d_p}{\eta}\right)^2 \tag{2.8}$$

where η ($= \sqrt{\nu\tau_\eta}$) is the Kolmogorov length scale. For $St << 1$ the particle will follow the fluid flow very closely. When $St > 1$ the particle has not enough time to respond to the varying flow velocity, causing its velocity to be different from the fluid velocity [20, 31]. So to get a good flow follower, ρ_p should be close to ρ_f. In other words: the particle should be neutrally buoyant. We do not want the particle to sink or float. Another way to get a good flow follower is decreasing the size of the tracer particle. In practice one will most likely combine both ways.

However, the Stokes number says only how good the particle follows the flow, once it is inside the flow. When the particle reaches the bottom of the tank, it does not say whether its will be lifted up again. The no-slip condition at the walls of the tank, result in lower velocities of the flow near the walls, which makes it harder for the particle to be lifted up. To verify whether the particle will be lifted up again, we have to look at the Zwietinger criterion. This criterion defines the minimum rotational speed of the stirrer for which one or multiple solid particles in a non-aerated, stirred tank, will be completely suspended. Which is also referred to as just suspended. Complete suspension was defined by Zwietering as: "the condition ... that no solid matter rests on the bottom of the stirred vessel. ... When such a small pile [of particles] remained at rest longer than 1 or 2 seconds before being broken up the suspension was judged incomplete" [33]. However, it does not guarantee that the particles will be homogeneously distributed through the tank. They can still remain only in the lower region. Using experimental data and theoretical analyses he derived the following correlation:

$$N_{js} = S\nu^{0.1}\left[\frac{g(\rho_p - \rho_l)}{\rho_l}\right]^{0.45} X^{0.13} d_p^{0.2} D^{-0.85} \tag{2.9}$$

where N_{js} is the just suspended stirrer speed in rev/s, S is the dimensionless Zwietering constant, X is the mass ratio between the solid matter and the liquid times 100. When the tank is also aerated, the minimum stirrer speed for complete suspension increases, which is given by:

$$N_{jsg} = N_{js} + \Delta N_{js} = N_{js} + a\phi_{air} \tag{2.10}$$

where a is a proportionality constant and the air flow rate, ϕ_{air}, should be given in the units vvm, which stands for vessel volumes per minute [15, 33].

An additional feature of the tracer particle is that it should emit gamma rays. This can be done by making a tracer particle with a core made of a radioactive isotope. Which isotope to use will be discussed in the next section.

2.6. Gamma radiation

Gamma rays are a type of electromagnetic radiation. Just as visible light they consist of photons, but than with a higher energy. Gamma radiation originates mainly from two different phenomena. The first is from the annihilation of an electron and a positron, where two gamma photons of 511 keV are generated. Moving away from each other with an angle of 180°. These are used in PET and PEPT.

The second is from excited nuclei descending to a lower energy state via emitting a gamma photon. These excited nuclei are often the product of radioactive decay. The energy of the photons is very specific for each radioactive nuclei, because of the discrete energy levels allowed in the nuclei. The energy difference between these levels and thus also the energy of the gamma photons is typically 100 keV or higher [17]. These are used in SPECT and RPT.

2.6.1. Sources

The activity, A, of a source is defined as the number of nuclear decays per unit of time and is measured in the unit Becquerel (Bq). The activity is proportional to the number of radioactive nuclei present in the source, N_0. This number decreases with every decay. A measure for the rate at which the decay happen is the half-life, $t_{1/2}$. This is the time it takes for half of the initial radioactive nuclei, N_0, to decay and lose half of the initial activity, A_0 [17]. With this we can calculate the activity and number of radioactive nuclei as a function of time, t:

$$A(t) = A_0 \left(\frac{1}{2}\right)^{t/t_{1/2}} \tag{2.11}$$

$$N(t) = N_0 \left(\frac{1}{2}\right)^{t/t_{1/2}} \tag{2.12}$$

Next follow some radioisotopes that are used as source of gamma radiation in nuclear medicine:

Technetium-99m (^{99m}**Tc**) is one of the most frequently used radioisotopes for diagnostic imaging in nuclear medicine. It is produced by the decay of molybdenum-99 (^{99}Mo) which is in turn one of the byproducts of the fission of enriched uranium-235 (^{235}U) after irradiation with neutrons. ^{99m}Tc has a half-life of 6 hours and emits gamma photons of 140 keV when falling down to its ground state ^{99}Tc. The ground state is not stable either. With a half-life of $2.13 \cdot 10^5$ years it decays to the stable ruthenium-99 (^{99}Ru) [27].

Cobalt-57 (^{57}**Co**) is used in medicine for radioisotopic labeling to investigate patients with a vitamin B_{12} deficiency. One way to produce it is by the proton reaction on iron-56 (^{56}Fe), the most abundant natural isotope of iron. ^{57}Co has a half-life of 272 days and decays to an excited state of iron-57 (^{57}Fe). The excited state falls down to the stable ground state mainly via emitting a gamma photon of 122 keV [9].

Gold-198 (^{198}**Au**) is used in nuclear medicine for the treatment of many diseases. It is produced by irradiating gold-197 (^{197}Au), the only natural isotope of gold, with neutrons. ^{198}Au has a half-life of 2.7 days and decays to an excited state of mercury-198 (^{198}Hg). The excited state falls down to the stable ground state via emitting a gamma photon of 412 keV [16].

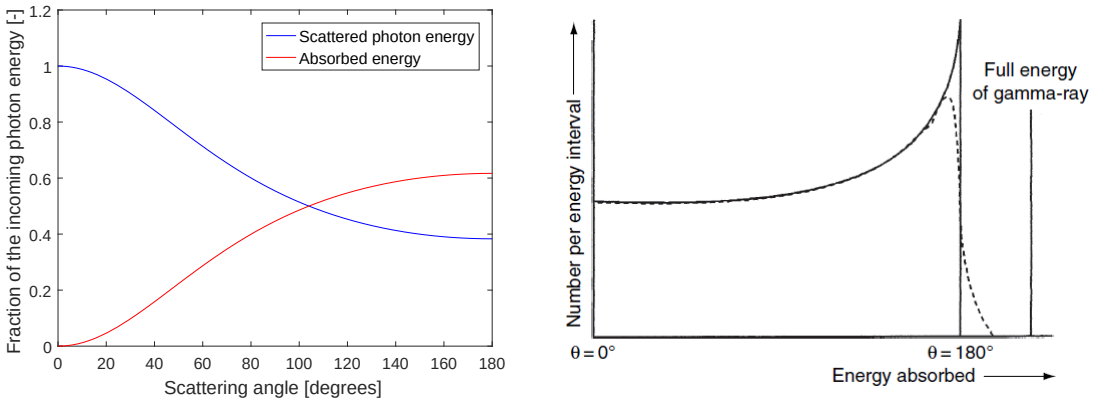

Figure 2.4: With on the left the scattered photon energy and absorbed energy due to Compton scattering as function of the scattering angle. And on the right the frequency of a certain amount of energy being absorbed [6].

2.6.2. Interaction with matter

In order to be able to detect the radiation coming from the source, the gamma photons have to travel from the source to the detector through several media and subsequently interact with the detector. Therefore we will now consider the interaction with matter in general. There are three types of interactions a gamma photon can have with matter: the photoelectric effect, Compton scattering and pair production.

The photoelectric effect occurs when a gamma photon is completely absorbed by a bound electron in an atom. This will eject the electron from the atom, making it a free electron (see Figure 2.5a). Some of the energy of the photon, E_γ, is used to overcome the binding energy, E_b. The remainder will go into the kinetic energy of the electron, E_e.

$$E_e = E_\gamma - E_b \tag{2.13}$$

The atom will be left in an excited state. Two things may happen next. The energy gets redistributed over the remaining electrons, possibly leading to more electrons being ejected. Or the vacancy of the photoelectron is filled up by an electron from a higher energy level, via emitting a fluorescent X-ray (see Figure 2.5b). Which electron is ejected depends on the energy of the gamma photon. If its energy is high enough to eject an electron from the K shell, the lowest energy level and therefore requiring the most energy [32], it is most likely to do so. If its energy is not sufficient, it will eject an electron from the L or M shell, with respectively the second and third lowest energies.

Compton scattering happens when only part of the energy of the gamma photon is absorbed by the electron. The photon will loose energy and change from direction (see Figure 2.5c). The energy of the recoil electron is given by:

$$E_e = E_\gamma - E'_\gamma = E_\gamma \left(1 - \frac{1}{1 + E_\gamma (1 - \cos\theta) / m_e c^2}\right) \tag{2.14}$$

where E'_γ is the energy of the scattered gamma photon, θ is the angle between the incoming and scattered photon, also known as the scattering angle, and m_e is the electron rest mass. On the left in Figure 2.4 is a plot of the scattered photon energy and the absorbed energy as function of the scattering angle. When $\theta = 0°$ the photon will lose no energy. The maximum amount of energy will be absorbed when the photon is backscattered, so at $\theta = 180°$, with 61.7% of the total energy being absorbed. On the right the frequency of each amount of energy being absorbed is plotted. As one can see, photons are most likely to backscatter. The solid line represents the case for assuming only free electrons and the dotted line the more realistic case taking also into account the bound electrons.

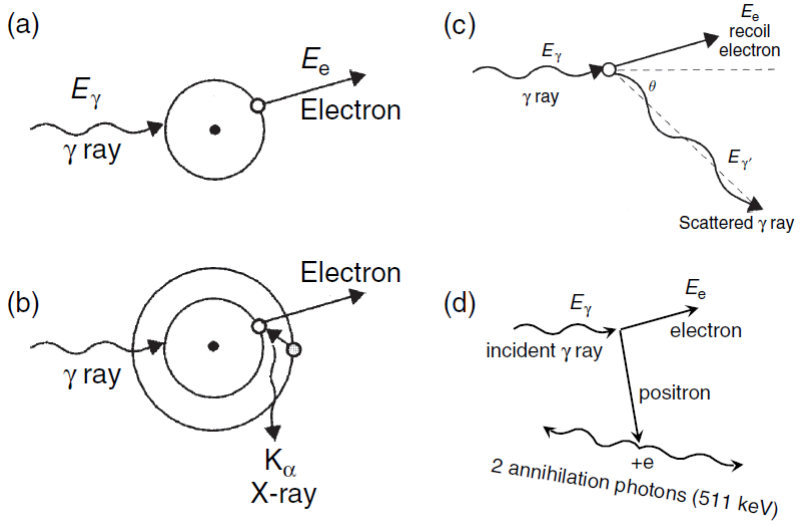

Figure 2.5: Interaction of gamma photon with matter. (a) The photoelectric effect with the electron being ejected from the atom, (b) a higher energy electron falling down into the vacancy of the photoelectron, via the emission of a fluorescent X-ray, (c) Compton scattering, (d) pair production and the annihilation of the created positron with another electron [6].

Pair production is the process where the energy of the gamma photon is turned into the creation of an electron-positron pair (see Figure 2.5d). In order to do so, the photon should at least have an energy of 1022 keV, equivalent to rest mass of the two particles via Einstein's formula $E = mc^2$. Each particle having a rest energy of 511 keV. The surplus energy of the photon is divided equally over the kinetic energy of the electron and positron. Both particles will lose this energy when they are slowed down by the medium. When it is slowed down, the positron will annihilate with a nearby electron, creating two photons of 511 keV [6].

2.6.3. Linear attenuation coefficient

Now we know how gamma photons may interact with matter, but how likely is this to happen? A measure for this is the linear attenuation coefficient, μ, which can be seen as the probability per unit length that the photon will interact with the medium. This value depends on the atomic number, Z, and the energy of the photon. This is shown in Figure 2.6 on the left for several materials: germanium (Ge), sodium iodide (NaI), lead (Pb) and silicon (Si). Each curve is different, although they show more or less the same trends. The linear attenuation coefficient shown here is the sum of three components, one for each type of interaction, as is illustrated in Figure 2.6 on the right for germanium. For photon energies below 200 keV, the photoelectric effect is dominant. For decreasing energies, there is a general trend of increasing linear attenuation coefficient. Both for the photoelectric effect component as for the total. However, there are some sudden steps down. These happen at the binding energies of the different electron shells and are called absorption edges. These happen because, as explained earlier, when the photon energy becomes lower than the binding energy of a certain shell, the electrons in this shell can no longer be ejected by the photon. Resulting in one way less for the photon to interact and thus decreasing the linear attenuation coefficient. For energies between 200 keV and 10 MeV, Compton scattering is dominant, but mostly because the photoelectric effect and pair production both are not likely to occur. Resulting in a minimum for the total linear attenuation coefficient. For energies above 10 MeV pair production dominates and the total linear attenuation coefficient starts to grow again [6].

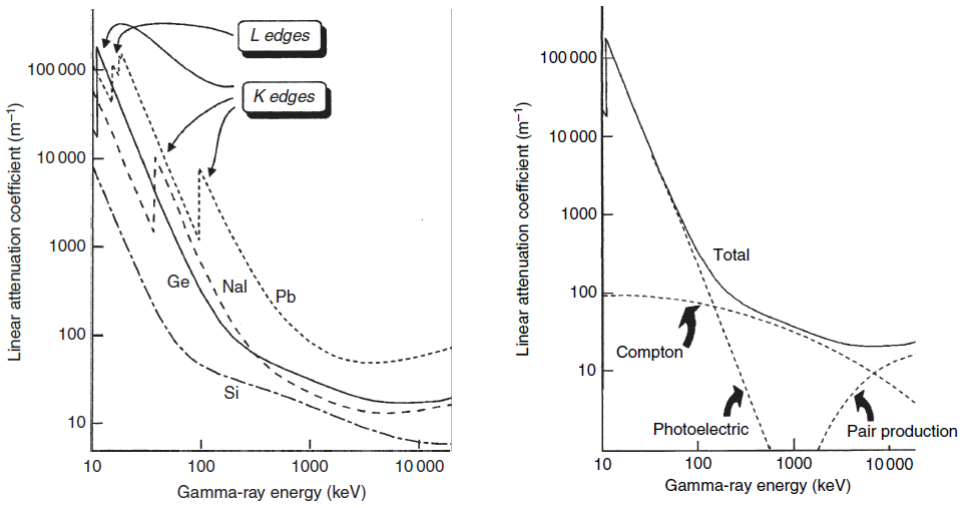

Figure 2.6: With on the left the linear attenuation coefficient of several materials plotted against the photon energy. And on the right the linear attenuation coefficient of germanium divided into the different components [6].

The total linear attenuation coefficient can be determined by doing the following experiment. Consider a layer of thickness th of a certain material, with a monochromatic gamma source on one side and a gamma detector on the other (see Figure 2.7). Both the source and the detector are narrowly collimated, such that only photons going in a straight line from the source to the detector are able to reach the detector. But on their way to the detector, part of the photons will interact with the material and will not reach the detector, since they are absorbed by an electron, converted into an electron-positron pair or scattered from their path to the detector. For a layer of thickness dx within the material the intensity of the gamma beam is reduced by a fraction:

$$-\frac{dI}{I} = \mu\, dx \tag{2.15}$$

Integrating this equation until the position x, which is the depth into the material, and defining the initial intensity of the incident beam I_0 gives the Beer-Lambert law, relating the intensity at a certain depth in the material layer to the initial intensity and the depth:

$$I(x) = I_0 e^{-\mu x} \tag{2.16}$$

Integrating over the whole thickness th leads to the intensity that will leave the material layer and reach the detector:

$$I(th) = I_0 e^{-\mu\ th} \tag{2.17}$$

So the intensity decreases exponentially with the thickness of the layer. Notice that the exponential goes rapidly to zero, but will never reach it. There will always be a change that a photon will get through. Something else to notice is that in general higher energy photons need a thicker layer to achieve the same attenuation, since they have a lower linear attenuation coefficient.

A useful quantity to define is the half value layer of a material, HVL. This is the thickness needed of that material to reduce the intensity to half its initial value. It is related to the linear attenuation coefficient as follow [11]:

$$HVL = \ln(2)/\mu \tag{2.18}$$

In Table 2.1 some values are shown for two specific energies: 122 keV of ^{57}Co and 412 keV, and for six materials: lead, NaI, Pyrex, Perspex, water and air.

Substituting the HVL into Equation 2.17 gives:

$$I(th) = I_0 \left(\frac{1}{2}\right)^{th/HVL} \tag{2.19}$$

The fraction of the initial intensity that will leave the material, is called the transmittance, T:

$$T = \frac{I(th)}{I_0} = e^{-\mu\ th} = \left(\frac{1}{2}\right)^{th/HVL} \tag{2.20}$$

The previous formulas only hold for monochromatic plane waves. Plane waves do not diverge and thus their intensity stays constant while propagating. However, usually when doing experiments with gamma photons, things are more complicated. Firstly, a real source never produces plane waves. Although when we are far enough from the source, a plane wave is a good approximation. Especially when using a collimator in front of the source. The longer the length and the smaller the diameter of the hole, the smaller the divergence of the radiation passing through the collimator, but also the lower its intensity. For small sources without collimation another approximation can be used. Namely that of a point source. This will result in the intensity being inversely proportional to the square of the radial distance from the source.

Secondly, photons that are scattered inside the layer, once or multiple times, might reach the detector. This leads to measuring more photons, than resulting from previous formulas. These additional photons have a different energy than the photons emitted from the source. Due to the scattering they have lost some of their energy. So by using energy discrimination, this effect can be eliminated.

The previous formulas are also for only one type of material layer. This is easily expanded to n layers:

$$I(th) = I_0 e^{-\sum_{i=1}^{n} \mu_i th_i} = I_0 \left(\frac{1}{2}\right)^{\sum_{i=1}^{n} th_i/HVL_i} \tag{2.21}$$

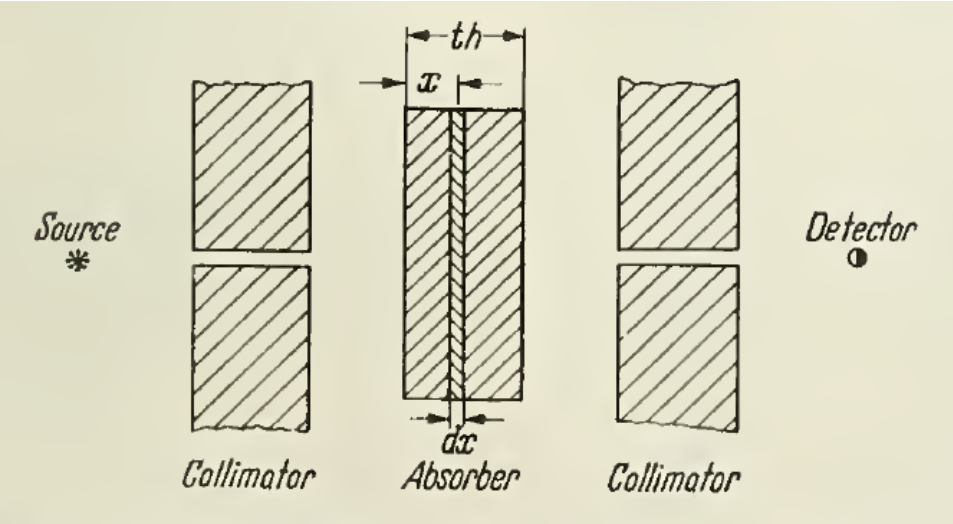

Figure 2.7: Experimental setup to determine linear attenuation coefficient according to Beer-Lambert law [11].

Table 2.1: Half Value Layers (HVLs) for the energies of the ^{57}Co and ^{198}Au source, respectively 122 keV and 412 keV, and for several materials. The values are obtained via interpolation, using the values from the website of the NIST [23].

Material	Energy (keV)	HVL (mm)
Lead	122	0.181
	412	2.76
NaI	122	1.91
	412	17.0
Pyrex	122	20.5
	412	33.0
Perspex	122	38.0
	412	57.7
Water	122	43.3
	412	66.3
Air	122	$3.97 \cdot 10^4$
	412	$6.10 \cdot 10^4$

2.7. Detection

Now we are ready to discuss the detection of the gamma photons that have reached the detector. The detectors used to detect these single gamma photons are called gamma cameras. They measure the energy of the incident photons and the time and position of the detection. Usually they consist of the following parts: a collimator, a scintillation crystal and photomultiplier tubes.

2.7.1. Gamma camera

A collimator is a sheet of an absorptive material (for example lead) with multiple holes or slits, placed in front of the detector. The purpose of the collimator is to let through only photons coming from the direction parallel to the holes. This gives information on the location of the source and reduces the detection of scattered photons. The smaller the holes or the narrower the slits, the higher the spatial resolution, but the less photons will get through and thus the lower the measured signal. The bigger the holes, the higher the signal, but the lower the spatial resolution.

A scintillation crystal is a transparent crystal which produces a flash of photons in the visible or near ultraviolet spectrum when a gamma photon interacts with it. This is the result of an energetic electron produced by either the photoelectric effect, Compton scattering or pair production. The number of photons produced is proportional to the energy of the gamma photon. Typically sodium iodide doped with thallium (NaI(Tl)) is used. This material has a very high chance of interacting with the gamma photons and thus making it possible to detect it. A thicker layer of scintillation crystal also increases the detection efficiency, but will make the location of the detected photon less accurate. This originates from the fact that the photons created in the scintillation crystal are emitted in all directions. So the thicker the layer, the more the photons can travel away from the position the gamma photon came in, before reaching the photomultiplier tubes. Resulting in a less accurate measured position.

Photomultiplier tubes (PMTs) are placed behind the scintillation crystal to convert the light photons to an electrical signal and also to amplify the signal (see Figure 2.8). When a photon hits the photocathode, a free electron is created via the photoelectric effect. A single electron is hard to measure. To amplify the signal, electrodes are placed between the cathode and the anode. These are called dynodes. At each subsequent dynode a higher voltage is applied, causing the electron to accelerate toward the next dynode. This way it gains enough energy to cause the emission of multiple electrons when it hits the dynode. These electrons are accelerated at their turn to the next dynode, causing even more electrons to be emitted. By repeating this for multiple times, a measurable signal is created.

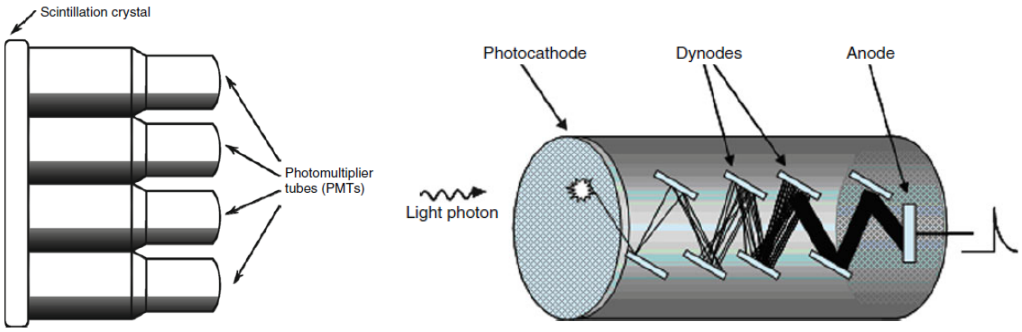

Figure 2.8: With on the left the positioning of photomultiplier tubes behind scintillation crystal [8] and on the right the amplification of the signal by a photomultiplier tube, by the emission of multiple electrons for each single electron hitting one of the succeeding dynodes [5].

The energy of the gamma photon can be determined by the amplitude of the electrical signal. The energy of the gamma photon determines the number of light photons that are created in the scintillation crystal, which determines the number of electrons there are emitted in the photocathode, which determines the magnitude of the amplified signal. The position is determined from the distribution of the signals coming from the PMTs.

Statistical fluctuations at each step in the detection process lead to uncertainties in the spatial position and measured energy of the gamma photon. The scintillation crystal used in the gamma cameras in SPECT is typically 10 mm thick, has a detection efficiency of 90% and an intrinsic spatial resolution of typically 3 mm for 140 keV gamma photons (like the ones from ^{99m}Tc) [8].

2.7.2. Measured energy distribution

When we place a source emitting gamma photons of a certain energy in front of a gamma detector, also a lot of other energies will be measured. In this section we will discuss the origin of these detections. Let us have a look at the energy distribution measured from a cesium (^{137}Cs) source emitting gamma photons of 662 keV, shown in Figure 2.9.

There is a high peak around 662 keV, corresponding to the full energy of the incident photon. This peak is called the photopeak. Although, the energies of the emitted photons from the source are very close together, the peak has a certain width. This is caused by the fact that the brightness of the flash created in the scintillation crystal by photons with the same energy may vary somewhat. Resulting in an inaccuracy in the measured energy.

Another feature that can be seen is the constant level below 400 keV. This is called the Compton continuum. This is the result of photons that Compton scatter once in the scintillation crystal and further do not interact with it. The amount of energy that is transfered from the photon to the crystal depends on the scattering angle, as is explained earlier. We see all the different scattering angles occurring. The maximum energy that can be absorbed via Compton scattering is lower than the incident photon energy. That is why there is a sudden drop after this energy. This is called the Compton edge. The counts do not go to zero, since higher energies might be absorbed by multiple Compton events. This is less likely to happen though.

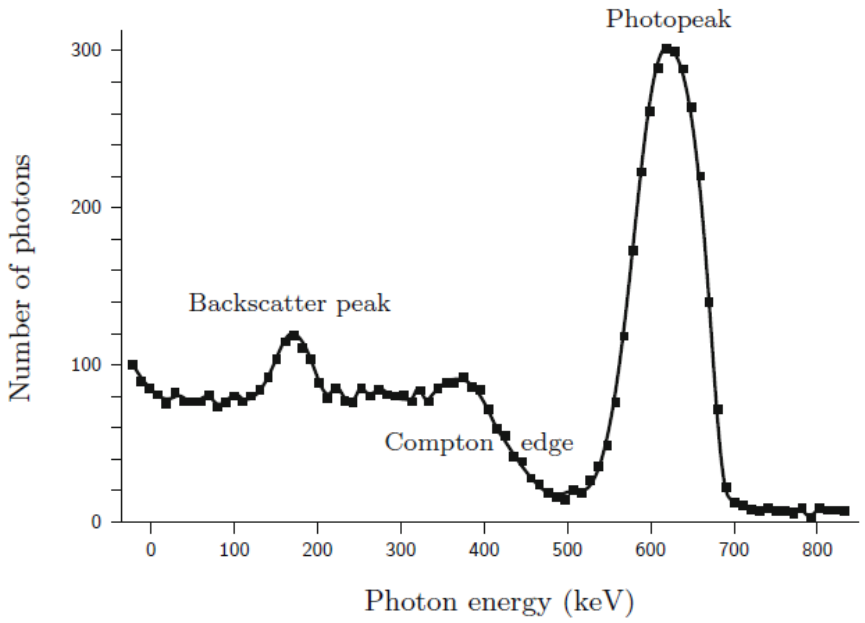

Figure 2.9: Measured energy distribution from a ^{137}Cs source emitting gamma photons at 662 keV [10].

However, not all photons that are measured, are coming from the source we are investigating. There is, for instance, always some radiation coming from other sources on earth and also from space. Most of these sources are far away, so the intensity of the radiation will be reduced a lot, due to divergence of the radiation and interactions with other matter. To further reduce the detection of this background noise, a dense material is put around the crystal, to absorb these photons and act as shielding. Often lead (Pb) is used for this. However, one would need an infinitely thick shield to absorb all background noise. So in practice one will always measure some noise.

Another source of noise happens in the electrical circuit of the detectors. This electrical noise causes the measurement of a signal while there was no interaction with a photon. This is called dark current. Due to thermionic emission of electrons at the cathode of the PMTs a pulse can be measured without the intervention of a photon, resulting in a fake detection [26].

Part of the measured photons are coming indirectly from the source. The shielding, blocking some background noise, also causes some photons to be measured we actually do not want to measure. For instance, the hump on top of the Compton continuum, which is called the backscatter peak. These are photons that do not interact with the crystal and reach the shielding at the back. Some of them might Compton scatter with an

angle of 180 ° (or a little less), sending it back to the crystal where it might interact after all. As it has lost most of its energy to the shielding, this peak occurs at a much lower energy.

Something that cannot be seen in this figure, but might happen as well, is the detection of fluorescent X-rays emitted by the shielding. These are created when the gamma photons are absorbed by the shielding via the photoelectric effect. As is explained earlier, an electron will be ejected from its atom. This is most likely an electron from the K-shell. This leaves the atom in an excited state. The vacancy of the photoelectron might be filled up by an electron from a higher energy level. The possible transitions for lead are summarized in Table 2.2. These might result in a peak or several peaks, depending on the energy resolution of the detector, in the range of 70-90 keV [6, 10].

There is also a chance that photons that interact with the detector, do not end up being recorded. The chance increases for high counting rates. It is caused by the dead time of the detector. This is the time the detector needs to measure and record a detected photon. Usually this is in the order of microseconds. During this time the detector is not able to respond to other incoming photons. The information of these photons will be lost and will lead to an underestimation of the photon count [25].

Table 2.2: Transitions in lead (Pb) of electrons from higher levels to the K-shell, emitting fluorescent X-rays.

Transition	Energy (keV)
KL_1	72.145
KL_2	72.807
KL_3	74.970
KM_1	84.156
KM_2	84.452
KM_3	84.940
KM_4	85.420
KM_5	85.521
KN_1	87.115
KN_2	87.244
KN_3	87.362
KN_4	87.571
KN_5	87.593

3

Experimental Method

In all the experiments that are performed, we tried to reconstruct the position of a radioactive particle. This was done under different conditions. To do these experiments we needed the following.

3.1. Experimental necessities

3.1.1. Radioactive tracer particle

First of all we need a radioactive tracer particle which we can follow. We have used two types of sources. The first is the same source as was used by Bechan [1]. This is a ^{57}Co source contained in a cylinder with a diameter of 10 mm and a height of 5 mm. This source will be used for a test measurement with the source at several fixed positions. The second source will be used for all other experiments. It is the same type of particle as was used by Noordman [24]. This particle consists of a 2 mm polystyrene sphere with a golden core (see Figure 3.1). A small piece of gold foil, about 2 mg, is inserted by puncturing a little hole of 0.5 mm in the polystyrene and putting the crumpled foil inside. To make sure the foil stays inside, the hole is closed with glue. This results in a particle with a total mass of 6.2 mg and an overall density of $1.48 \cdot 10^3$ kg/m^3. The density of the particle is to high to be neutrally buoyant, and thus it will tend to sink, especially for low stirrer speeds. More on this later.

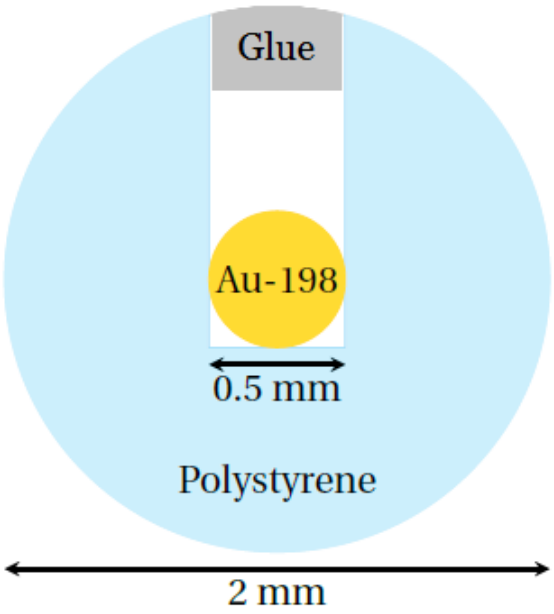

Figure 3.1: Tracer particle used in experiments. Consisting of a punctured polystyrene sphere. A little piece of gold foil, of approximately 2 mg, is crumpled and put inside the hole, after which the hole is closed with glue. Adapted from [1].

3.1.2. Gamma detectors

To be able to reconstruct the position of the tracer particle, we need to detect the gamma radiation emitted by it. This is done by three detectors facing towards each other, with approximately 120° between them (see Figure 3.2 on the left). The detectors and their casings are quite big and heavy (~ 0.7 m in each direction, weighing a few hundred kilograms). Therefore they are placed on manual forklifts such that they can be moved around and that their vertical position can be altered (see Figure 3.2 on the right).

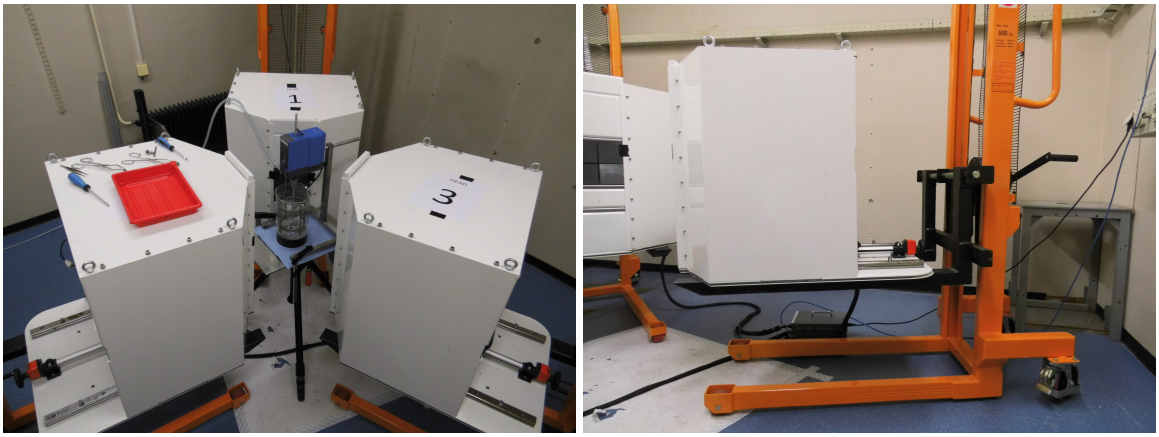

Figure 3.2: With on the left a top view of the setup with the three gamma detectors. With on the right one of a detector on a manual forklift.

More details of the detectors are shown in Figure 3.3. The gray parts are the casing made of lead. In the front of the casing there is an opening where the collimator can be placed. To fill up the remainder of the opening lead blocks and cylinders are used. Respectively the blue-gray and purple parts in the figure on the left. These parts have thickness of 25 mm. Using this and the HVL from Table 2.1 and putting them in Equation 2.19 shows that only 0.19% of the 412 keV photons gets through. For lower energetic photons this will be even less. The green part on the right is the detector plate, with the scintillator crystal and PMTs. The detector plate consists of 512x512 pixels of 1.072 mm. It measures photons in the range from 0 up to 600 keV. The blue part is a crank to adjust the distance between the detector plate and the collimator. The possible distances range from 155 up to 600 mm. During all experiments the distance is set at 400 mm.

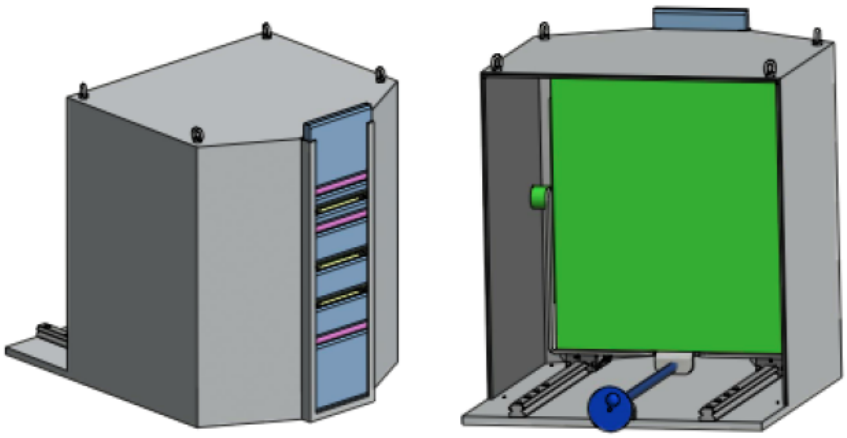

Figure 3.3: Schematic of the gamma detectors, with on the left a front view and on the right a rear view. With in gray the casing, in blue-gray and purple respectively lead blocks and cylinders, in green the detector plate and in blue a crank to adjust the distance between the detector plate and the collimator. Adapted from [21].

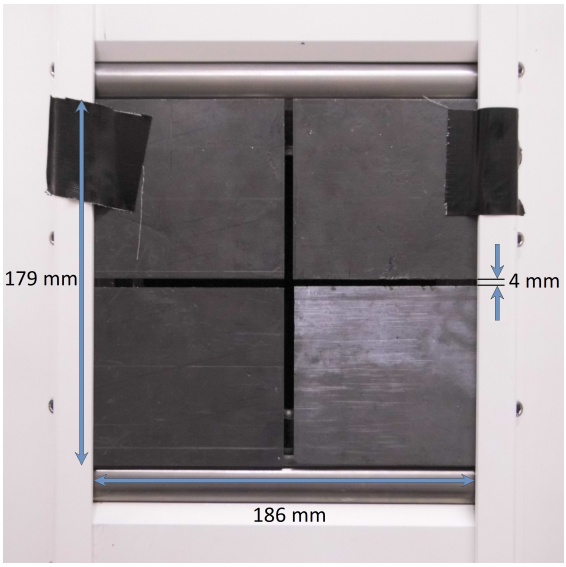

Figure 3.4: The collimator that is used in the experiments. Consisting of a cross slit, created with four plates of 2 mm lead.

The collimator that is used in the experiments is a cross slit. This will result in a cross in the image on the detector. The position of the cross image, says something about the position of the source. Combining the information from the three detectors gives a reconstructed position. More on this is explained in the next chapter. The cross slit consists of four lead plates with 4 mm spacing between them. Each plate is 2 mm thick. The cross has a vertical length of 179 mm and a horizontal length of 211 mm. But due to the clamping on the sides, the effective horizontal length is 186 mm. The lead plates are supported by a piece of Perspex, from which also a cross is cut out. Only 0.047% of the 122 keV photons will get through the lead of the collimator, resulting in a very clear cross in the image on the detector. However 61% of the 412 keV photons will get through. The image will now be more like a square with in the middle a higher number of detections, resulting in a cross. This will be more challenging to process. In all experiments the collimator is centered in front of the detector plate.

3.1.3. Traversing device

For one of the experiments we used a traversing device. This device is computer controlled using LabVIEW and moves very accurately along a predefined sequence of positions in 3D space. For each position we determine how long it should stand still there, before going to the next. The same LabVIEW interface is used to control the detectors. So with the source mounted onto the traversing device, we can easily measure the source at multiple specific positions in air.

3.1.4. Stirred tank

All the other experiments are done with the source inside a stirred tank (see Figure 3.5 on the left). As tank a beaker is used with a diameter, T, of 147 mm which is filled until a water height, H, of 147 mm. This results in 2.5 L of water. Further we used a Rushton turbine (see Figure 3.6) with a diameter, D, of 49 mm with a clearance, C, of 50 mm above the bottom of the tank. The stirrer is powered by a motor positioned above the tank. The motor operates in a range of 30-600 rpm. The four baffles that are used, have a width of 13.9 mm and are connected to each other via two circular connection pieces (see Figure 3.5 on the right), such that they can be positioned easily in the tank. These and more dimensions are summarized in Table 3.1.

3.1.5. Aerator

For some of the experiments we wanted to have air bubbles being injected at the bottom of the tank. Therefore we used an aerator (see Figure 3.7). This is a metal pipe bent in a circle, with 12 holes of 1 mm in the upper side of the ring. The ring has an outer diameter $D_{aer,out}$, an inner diameter $D_{aer,in}$ and the holes are positioned on a circle of diameter $D_{aer,h}$. The clearance of the aerator above the bottom of the tank is C_{aer}. The values of these dimensions are summarized in Table 3.2. The pipe of the aerator goes up, along one of the baffles, outside the tank and is connected to a mass flow controller with the range of at least 2-10 L/min.

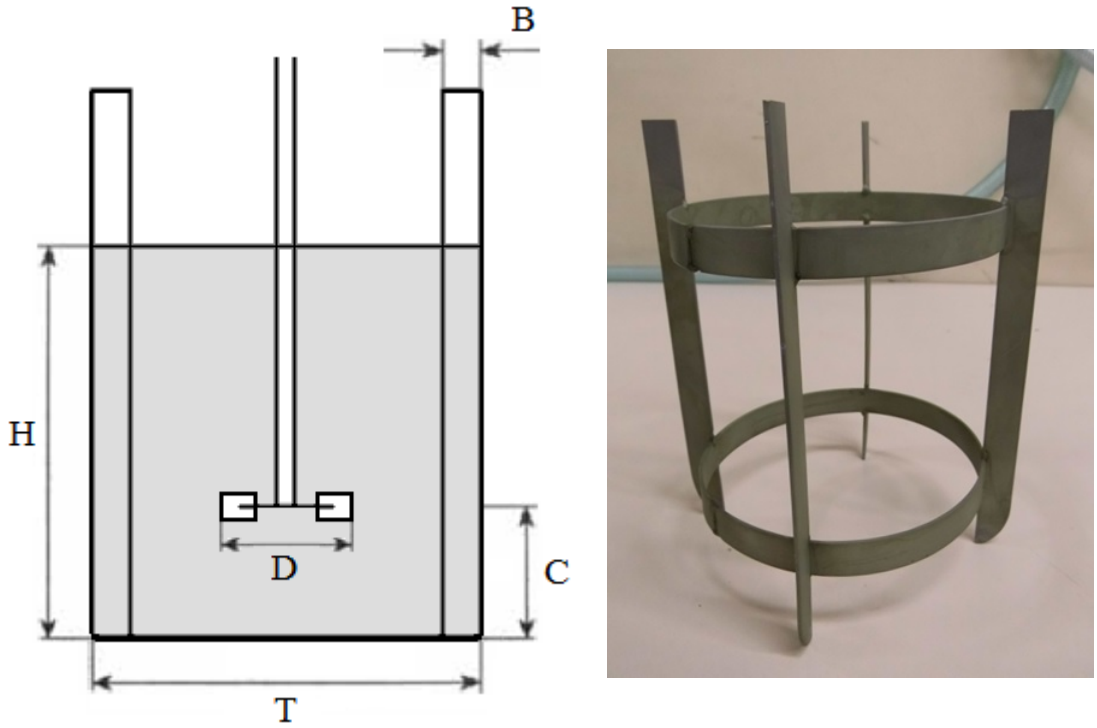

Figure 3.5: With on de left a sketch of the baffled tank agitated by a Rushton turbine with the corresponding dimensions and with on the right a picture of the baffles.

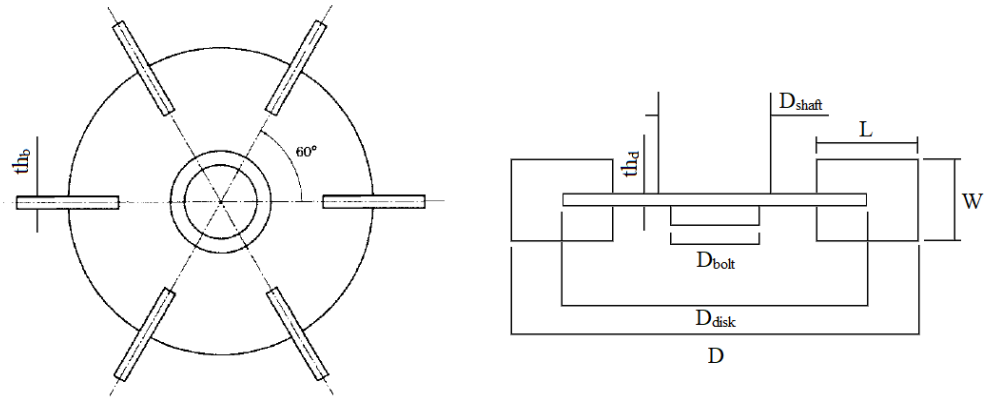

Figure 3.6: A Rushton turbine and its dimensions. Adapted from [18].

Table 3.1: Dimensions of the tank, stirrer and baffles

Quantity	in mm	in T, D or C
T	147	-
H	147	T
D	49	T/3
B	13.9	0.095T
C	50	0.34T
D_{disk}	32.6	0.67D
D_{shaft}	9	0.18D
D_{bolt}	6.5	0.13D
L	12.5	0.26D
W	10	0.20D
th_b	1.5	0.01T
th_d	1.5	0.01T

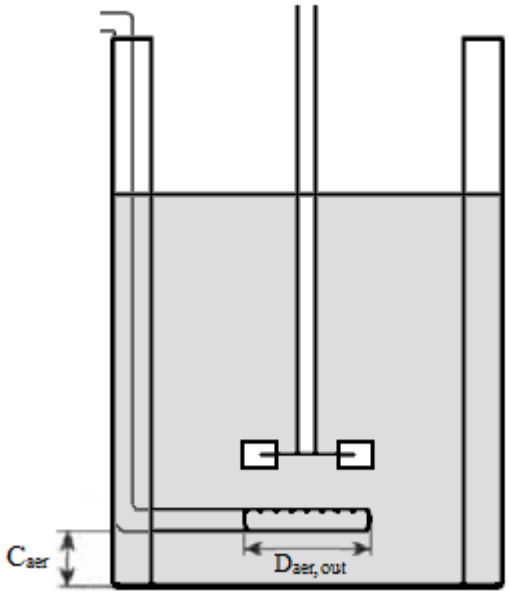

Figure 3.7: A baffled tank agitated by a Rushton turbine with aerator and the corresponding dimensions.

Table 3.2: Dimensions of the aerator

Quantity	in mm
C_{aer}	5
$D_{aer,out}$	36
$D_{aer,h}$	30
$D_{aer,in}$	24
th_{aer}	6

3.1.6. Rotator

For one of the experiments we wanted the source to move along a circular trajectory. Therefore a special object is made, which will be referred to as the rotator (see Figure 3.8 on the left). This is a piece of Perspex mounted onto a aluminum shaft. It is made such that a cup (see Figure 3.8 on the right) can be placed in one of the ends. The source is put inside the cup, where the lid is designed such that it will keep the source in place at the bottom of the cup. A bolt is used to fasten the cup in the rotator. The radius of the circular motion can be varied in two ways. One is by changing which side of the cup is put first into the rotator. With bottom first, the source is closer to the shaft and thus the radius is smaller. With the lid first, the source is farther away from the shaft and thus the radius is larger. The second way is by adjusting the depth at which the cup is put into the rotator.

3.1.7. Tongs and tweezers

At some point we have to place the source in the setup. To decrease the amount of radiation we will receive, we want to maximize the distance from the source to our body. Therefore it is useful to use tongs and tweezers to handle the source with.

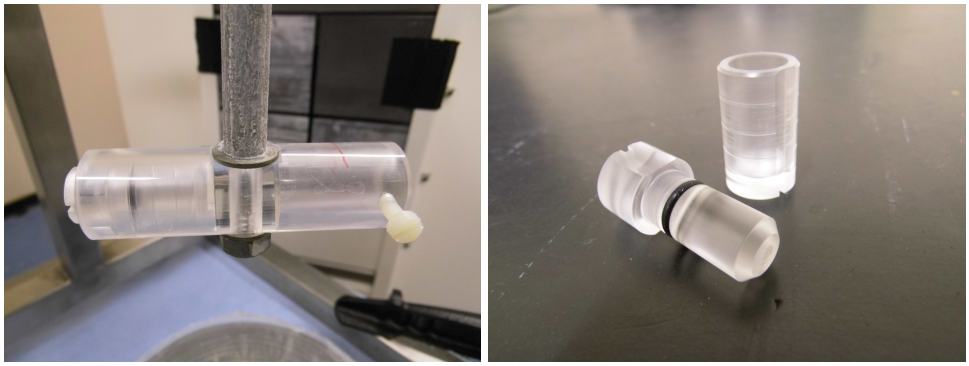

Figure 3.8: With on the left the rotator and on the right the cup which goes into the rotator.

3.2. Experiments

The final goal of this research is to track a tracer particle while it is moving freely with the flow in a stirred tank. But since you will not know where it will be going, you will neither know how accurate the reconstruction of its path is. Therefore we have to do some other experiments as well. We will, for instance, also measure with the source at several fixed positions in air, to see what accuracy can be achieved with the particle not moving and how this depends on the time frame rate that is used and the position of the source. Furthermore, we will measure with the source moving along a known, circular trajectory in a tank with water, to see how the accuracy depends on the velocity of the source. This is done for different radii of the trajectory. After this we will try to track a tracer particle when it is moving freely with the flow in a stirred tank. At last we will repeat the experiments with a moving source, but now with air bubbles being injected at the bottom of the tank, to investigate the effect of bubbles on the accuracy of the reconstruction. Each experiment is explained in more detail in the following sections.

3.2.1. Fixed positions

The first experiment is done by measuring the source at several fixed positions in air. For this we mounted the source to the traversing device and placed the three gamma detectors around it (see Figure 3.9). Approximately at 260 mm from the source, with 120° between the detectors and the center of the collimators at the same height as the source. This position of the source is chosen as origin. From this position all other positions are determined. The orientation of the chosen coordinate system is shown in the figure at the bottom right. Above that the coordinate system of the traversing device is shown.

This experiments is done twice. Once with a ^{57}Co source with an activity of 3.2 MBq and once with a ^{198}Au source of 69 MBq. The ^{57}Co source is used to test the setup, before doing the measurements with the higher activity ^{198}Au source. The ^{57}Co source is also used by Bechan [1] and due to its relatively long half-life, its activity was still high enough to use it right away. The gold inside the tracer particle had to be activated in the reactor of the Reactor Institute Delft (RID) of the TU Delft to obtain a ^{198}Au source.

The ^{57}Co source has a little piece of female screw thread attached to the cylinder containing the source. So it can directly be mounted to the traversing device. For the ^{198}Au source a holder is made which can hold an Eppendorf tube containing the source. Once the source is placed in the setup, the sequence is started. The ^{57}Co source is measured for 3 s at each of the 98 positions. The ^{198}Au source is measured for 1 s at each of the 240 positions. The range of positions for which is measured, corresponds with the size of the tank that will be used in the following experiments. However, the ^{57}Co source is measured in a slightly smaller range. For the complete sequences see Appendix B.

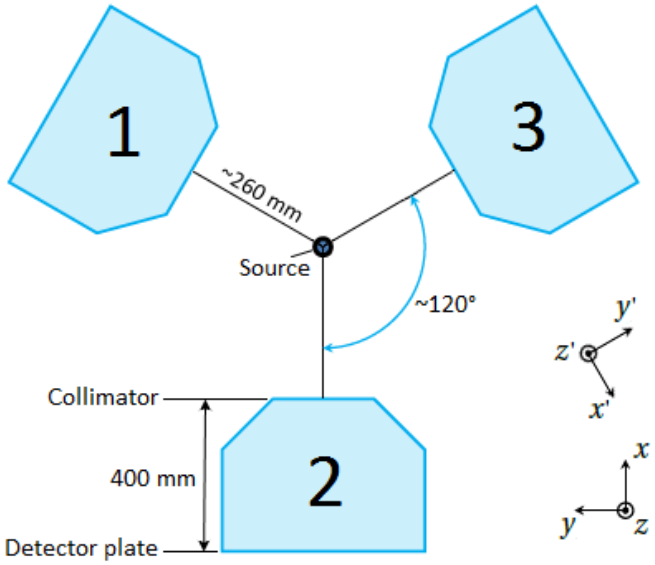

Figure 3.9: Top view of the setup for the experiment with the source at fixed positions. With the source mounted to the traversing device and the three detectors placed around it.

3.2.2. Moving freely in a stirred tank

For this experiment the traversing device is replaced by a table with the stirred tank on it. It is positioned with the center of the tank approximately at the origin. The Rushton turbine is placed in the motor and set at a clearance of 50 mm. The same ^{198}Au source, with an activity of 69 MBq, is put in the water of the tank, after which the motor of the stirrer is turned on. We have measured 60 s for each rotational speed, from 180 up to 540 rpm with steps of 60 and thus with Reynolds numbers ranging from $7.2 \cdot 10^3$ up to $2.2 \cdot 10^4$. See Appendix D for all rotational speeds of the stirrer and the corresponding Re. The Stokes number of the tracer particle ranges from 27 up to 140 for the different stirrer speeds. This is quite large, but there was no time to design a new tracer particle. To determine the accuracy of the technique, the particle had to move, but not necessarily exactly with the flow. Using the Zwietering criterion we find N_{js} = 293 rpm. Hopefully we will be able to see in our results whether this is confirmed by our experiments.

3.2.3. Moving along a known circular trajectory

For this experiment the Rushton turbine is replaced by the rotator. Due to the time necessary to prepare this experiment, another ^{198}Au source had to be activated. This one has an activity of 45 MBq and is put in a cup. When the cup is put as far as possible into the rotator, with the lid first, the radius of the circular trajectory is 38.8 mm. With bottom first the radius is 10.3 mm. As third radius 19.4 mm is chosen, which is achieved by putting the bottom of the cup first, but not all the way into the rotator. We tried to find several combinations of rotational speeds for the three radii such that the tangential velocity is almost the same for each radius. The tangential velocities range from 35 to 450 mm/s. See Appendix C for all rotational speeds. The time during which is measured, varied with the rotational speed. We desired to measure at least for 5 s, but also for at least 10 rotations. The experiments are done with the rotator at 50 mm above the bottom of the tank. Corresponding to z = -23.5 mm.

3.2.4. The effect of bubbles

Both the freely moving as the moving along a known circular trajectory experiment are done as well with different air flow rates. Using the aerator, we measured for air flow rates ranging from 2 up to 10 L/min with steps of 2. Using the Zwietering criterion for aerated tanks we see N_{jsg} increasing up to 520 rpm. Hopefully we will be able to see in our results whether this is confirmed by our experiments.

4

Post-processing

To obtain a reconstructed position of the source, we have to process the measured data, combine the information from the three detectors and use the geometry of the setup. We will now look at what is measured by the detectors and how we process this data to obtain something useful.

When a photon is measured by one of the detectors, the following properties are written down: the number of the detector, the energy of the photon, the time of detection and the x and y-coordinate of the pixel where it is detected. This is saved in a LM-file. In MATLAB this is converted to a MATLAB Data file, for further processing.

4.1. ^{198}Au source

We will first consider the ^{198}Au source of 69 MBq fixed at the origin. Measuring for 1 s resulted in $1.04 \cdot 10^6$ detections, of which $3.5 \cdot 10^5$ where measured by Detector 1. These are shown in Figure 4.1 on the left. All the 512x512 pixels are shown, but only the ones that are blue, have detected one or more photons. There are areas where the number of detections is more dense than in other areas. Four areas can be distinguished, shown in the figure on the right.

The first area is where no photons are detected (the white space at the left and right edges). This could mean several things. The photons directed towards these pixels are blocked, by lead for instance, or these pixels do not work properly or they do not exist at all. However, when we increase the time frame length we see more and more detections occurring in this area. So the first explanation is most plausible. The second area is where some photons are detected (in red). These photons passed through the shielding. The third area is where the detections are more concentrated (in blue). These photons passed through the lead plates of the collimator. The fourth area is where the detections are most concentrated (in black). These photons passed through the cross slit of the collimator.

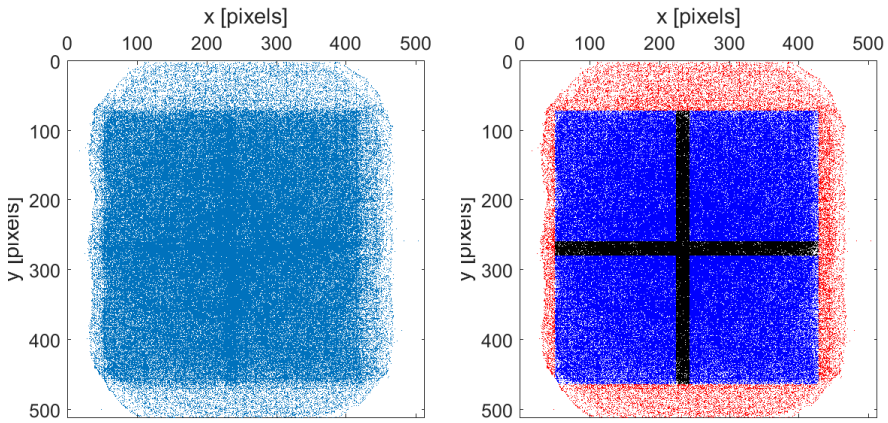

Figure 4.1: Detections in a [0 600] keV energy window during 1 s on the 512x512 pixels of one of the detectors with the ^{198}Au source of 69 MBq positioned at the origin, with on the left all detections in the same color and on the right each area with its own color.

Let us have a look at the energy distribution of the detected photons. This is shown if Figure 4.2. There are three peaks clearly visible. One at 85, 185 and 445 keV. Respectively corresponding to the fluorescent X-rays of Pb, the backscatter peak and the photopeak of ^{198}Au. The Compton edge at 260 keV is not that clear due to the backscattering peak, but there is a small hump visible after which there is a sudden drop.

Something that should be noticed, is that these energies are a bit higher then expected. We would expect for instance the photopeak to be around 412 keV. It might be that the detectors are not that good calibrated. This should be investigated further to find the real cause. But for the scope of this research it is not important.

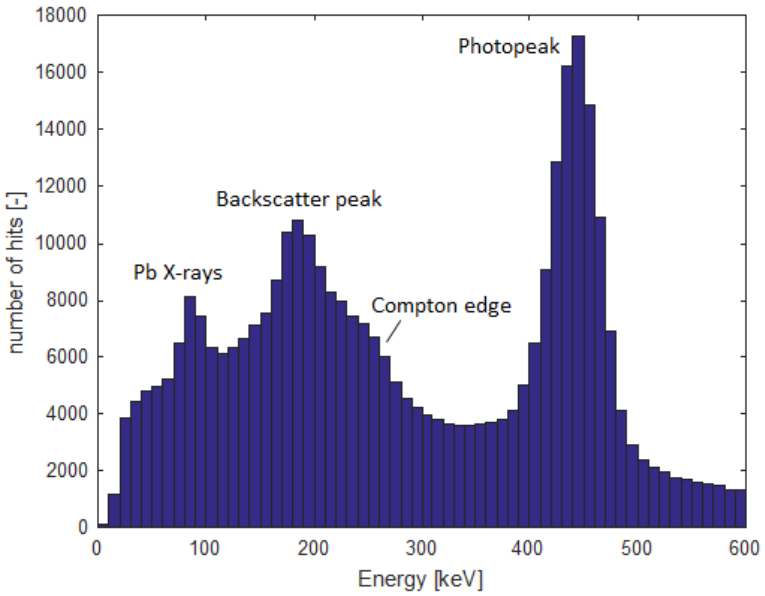

Figure 4.2: The energy distribution of the detections during 1 s on one of the detectors with the ^{198}Au source of 69 MBq positioned at the origin.

To improve the image of the cross we want to use energy discrimination. We divided the energy distribution into ten energy windows, each with approximately 35000 hits, and plotted for each the hits on the detector (see Figure 4.5). We would expect that the detections forming the cross to have an energy within the photopeak, since these did not lose some of their energy to the shielding or the collimator. And indeed, there is a cross visible in the energy windows [418.1; 442.2] and [442.2; 465.6] keV, which cover together most of the photopeak. But in almost all lower energy windows there is also a cross visible. This originates from the fact that the detector does not always absorb all the energy of an incident photon, which results in the Compton continuum. Since all those lower energies also contain information about the position of the cross, we decided to take an energy window of [5 480] keV, which seemed to give the best results. So in all that follows, this energy window will be used, unless stated differently.

To determine the position of the center of the cross we use the following procedure. First we project all the detections of both the x and y-axis, of which the result is shown in the two top plots of Figure 4.6. So we are looking now at the number of detections in each column (for the x-axis) and each row (for the y-axis) of pixels. We see in each plot a clear peak appearing in the middle, corresponding to the position of the cross. This way we can determine the x and y-coordinate separately. Since the source is not moving we could take a time frame of 1 s. When the source starts moving, the image is spread out. This effect is called motion blur and happens as well when one takes a picture of a moving object. Therefore one wants to use then a shorter time frame, such that the source has moved a shorter distance during a time frame. Unfortunately, shorter time frames mean less detections and due to the stochastic behavior of the detections, the plots become more chaotic with larger fluctuations. In Figure 4.6 there are also plots shown with shorter time frames, and thus higher frame rates. At 50 fps (frames per second) some fluctuations cause equally high peaks as the peak of the cross, making it less clear which peak corresponds to the cross. Therefore we will do some filtering next. As example we will use the detections with a frame rate of 50 fps.

The peak corresponding to the cross, which we will refer to as the cross peak from now on, is the or one of the highest peaks in such a plot. Using a threshold we will get rid of a lot of useless data (see second row Figure 4.7). Now we have the cross peak and some additional peaks. The difference between these peaks is that these additional peaks are very narrow, only a few pixels wide. Therefore we delete all values of which both nearest neighbors are zero or both second nearest neighbors are zero. This results in the third row of Figure 4.7. Now we are left with the cross peak and very few additional peaks. These additional peaks are almost always lower than the cross peak.

The cross peak, however, consists itself out of multiple local peaks and the highest peak is not necessarily in the middle. This would have made things easier. Making the time frame length longer will reduce the number of local peaks and the highest peak will tend to move to the middle. In both cases, the best thing to do is to take a weighted average of the pixels covering the cross peak, with as weights the number of hits for that pixel, and define this as the center of the peak. This is done by taking an interval around the highest peak. When multiple peaks are the highest, the one with the most hits within the chosen interval is used. Since the recorded image of the cross is slightly wider than the actual image, due to the spatial resolution of the detector, the width of the interval is taken to be twice the width of the actual image with the source at the origin. The peak position resulting from this weighted average and the interval that is used are shown in the fourth row of Figure 4.7.

4.2. ^{57}Co source

Now we will consider the ^{57}Co source of 3.2 MBq fixed at the origin. Measuring for 3 s resulted in $3.9 \cdot 10^4$ detections, of which $1.2 \cdot 10^4$ where measured by Detector 1. These are shown in Figure 4.3. As was expected, the collimator works much better for these lower energetic photons. It lets only a very small fraction of the photons go through. This results in much clearer peaks when we project the detections to the axes (see Figure 4.4). Even though they are almost thrice as low. This makes the determination of the peak position more accurate end less sensitive to fluctuations when increasing the frame rate.

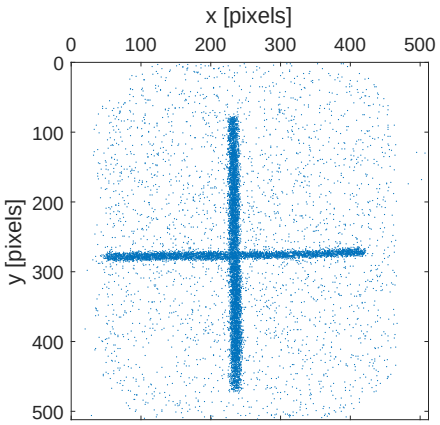

Figure 4.3: Detections in a [0 600] keV energy window during 3 s on the 512x512 pixels of one of the detectors with the ^{57}Co source of 3.2 MBq positioned at the origin.

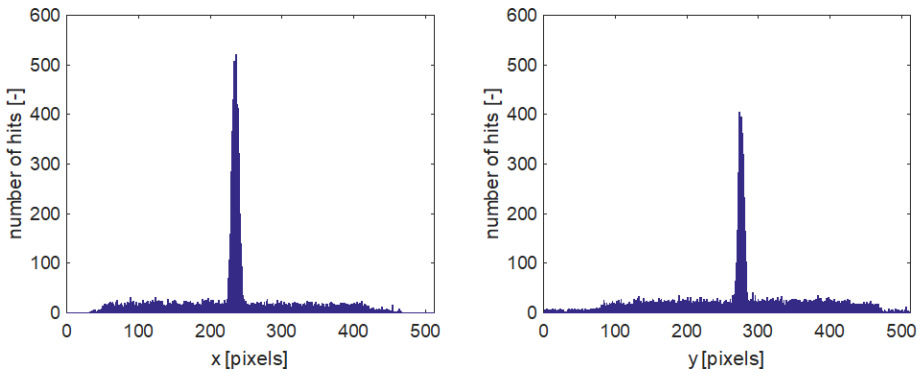

Figure 4.4: Detections during 3 s one of the detectors with the ^{57}Co source of 3.2 MBq positioned at the origin, projected to each of the axes. With on the left a projection to the x-axis and on the right a projection to the y-axis.

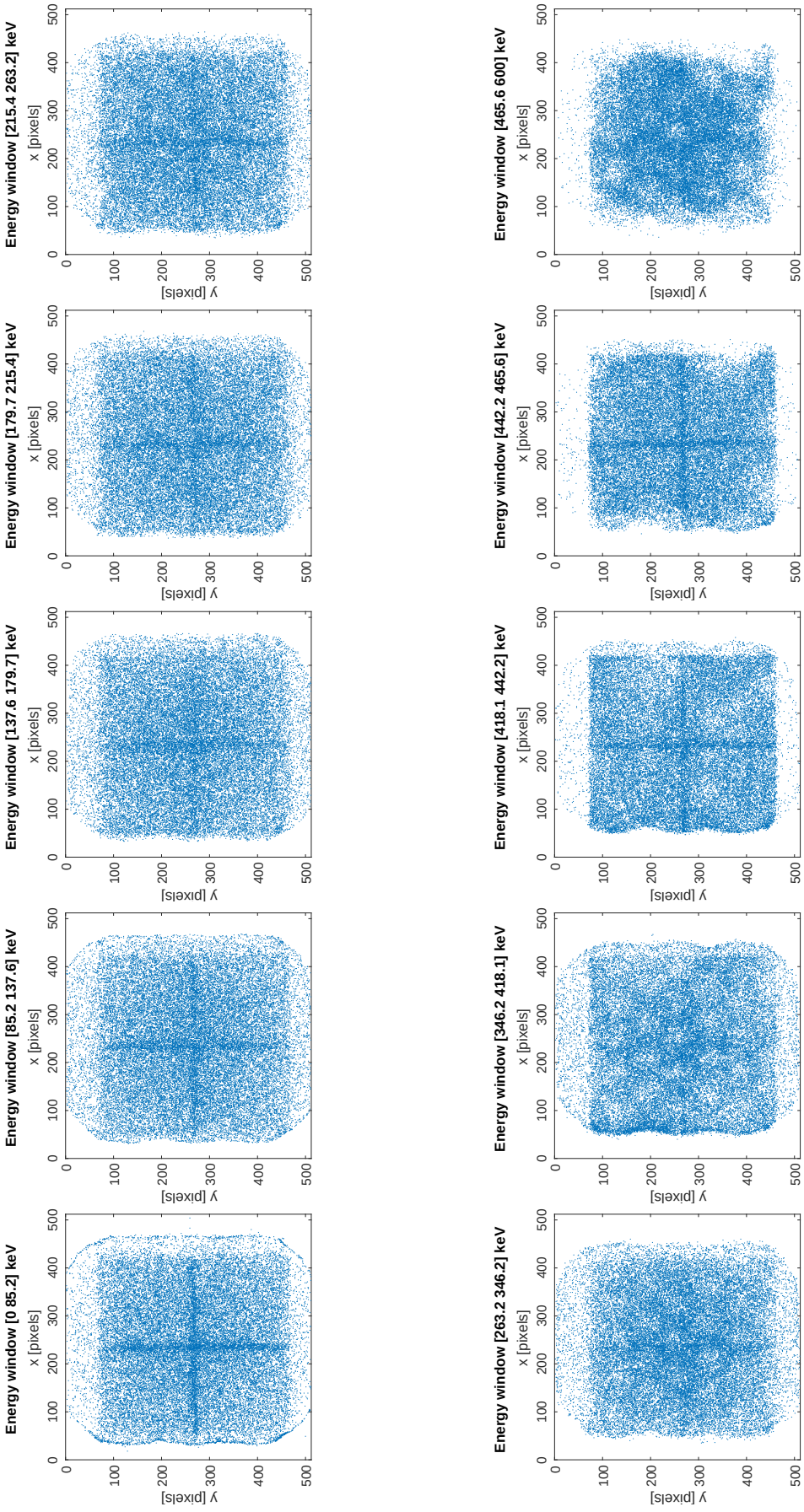

Figure 4.5: Detections during 1 s on the 512x512 pixels of one of the detectors with the ^{198}Au source of 69 MBq positioned at the origin for different energy windows.

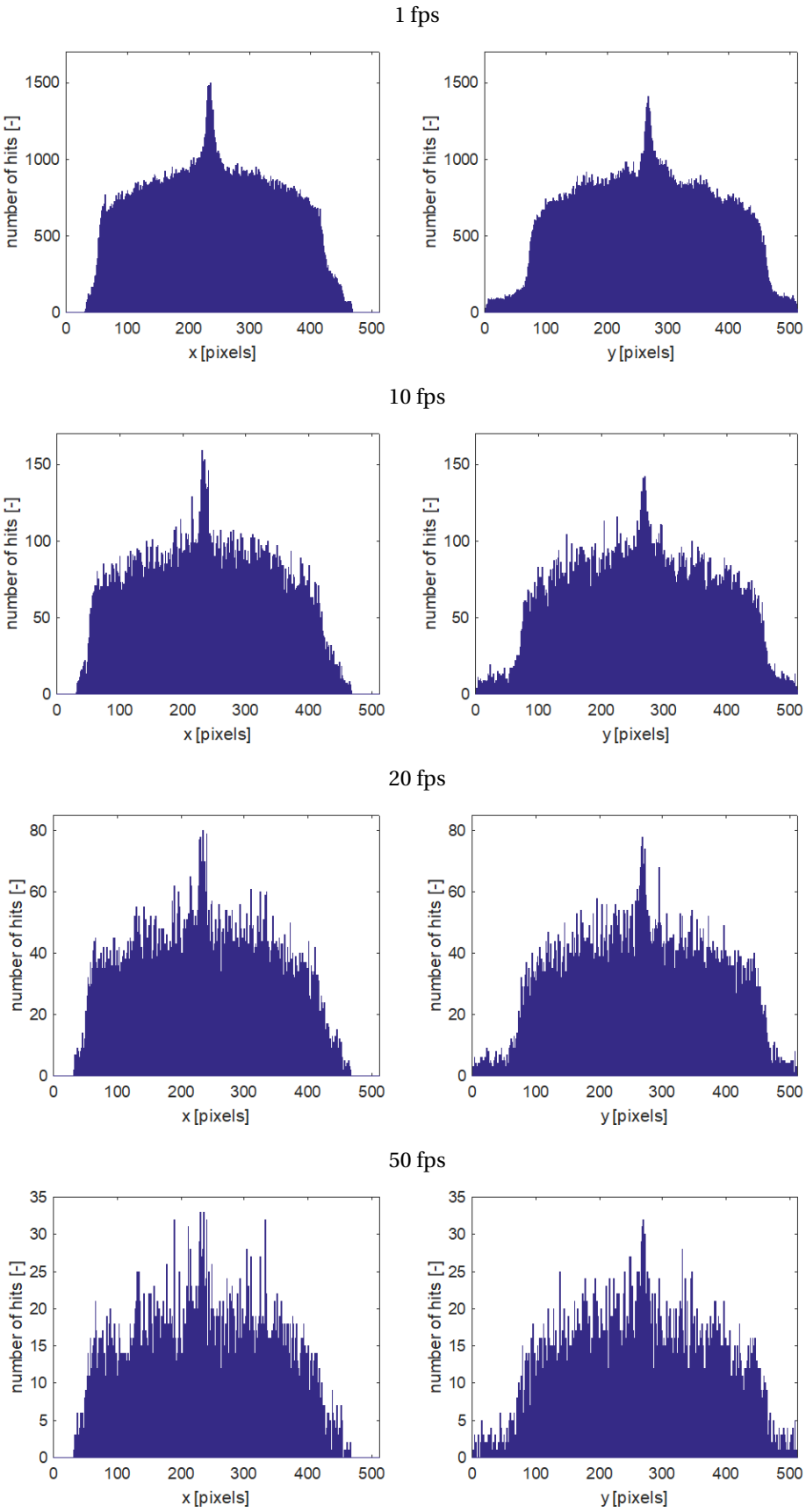

Figure 4.6: Detections for different frame rates on one of the detectors with the ^{198}Au source of 69 MBq positioned at the origin, projected to each of the axes. With on the left a projection to the x-axis and on the right a projection to the y-axis.

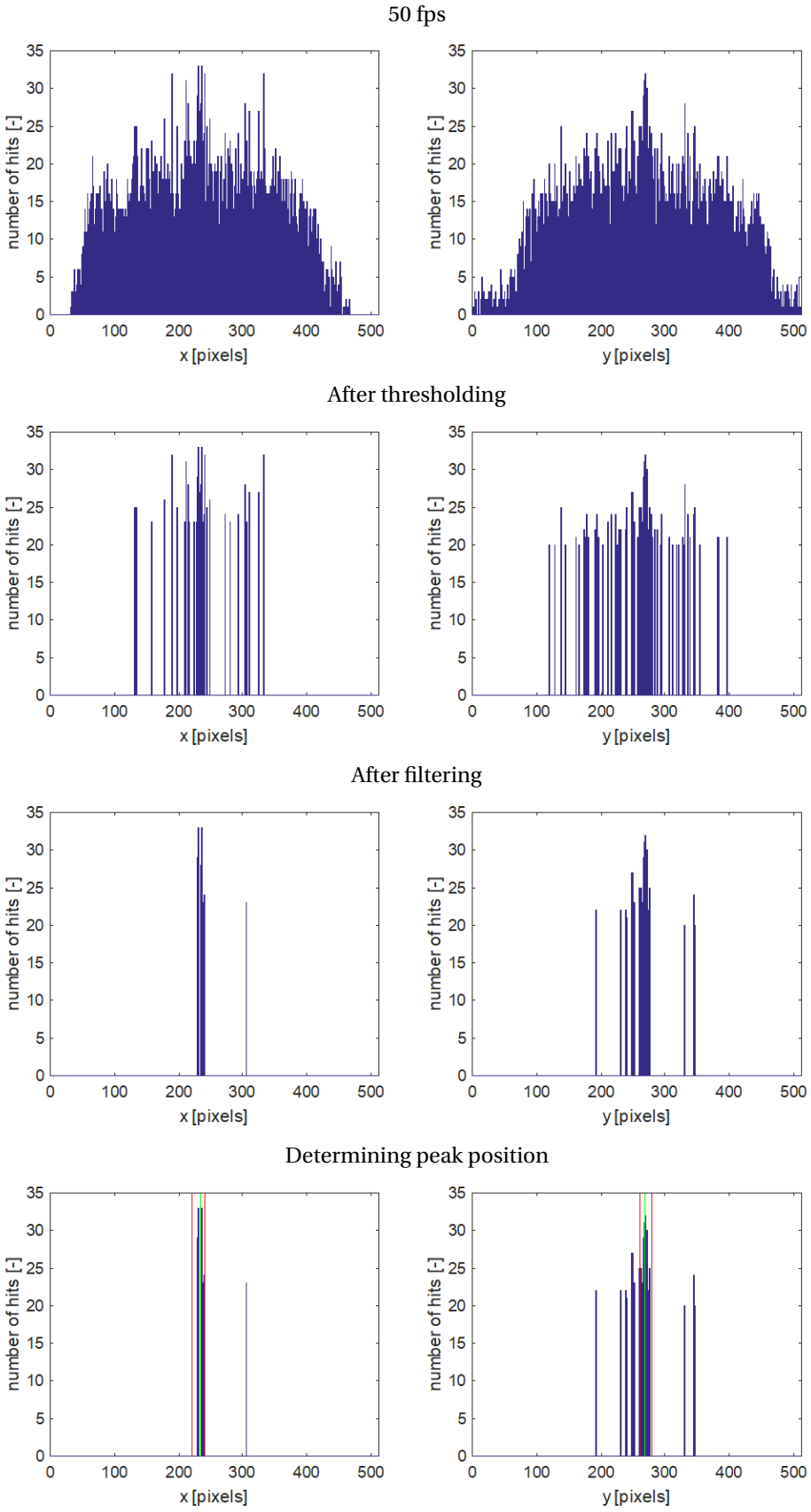

Figure 4.7: Detections for one frame using 50 fps, projected to each of the axes. With on the left a projection to the x-axis and on the right a projection to the y-axis. Using thresholding, filtering and a weighted average to determine the position of the peak. The red and green lines in the lowest two plots are respectively the interval of the weighted average and the determined peak position.

5

Reconstruction

Now we know the center positions of the three cross images. Each contains information about the location of the source. Since the photons creating the image passed through the cross slit, we know something about the direction the photons came from and thus in which direction the source should be. We used the following procedure to reconstruct the position of the source. We separated the information given by the horizontal and vertical part of the cross slits. Therefore we need the following definitions (see Figure 5.1): the position of the center of the cross image on the detector, $\mathbf{p}$, the left and right extreme of the cross slit (vertically centered), $\mathbf{L}_s$ and $\mathbf{R}_s$ and the upper and lower extreme of the cross slit (horizontally centered), $\mathbf{U}_s$ and $\mathbf{D}_s$.

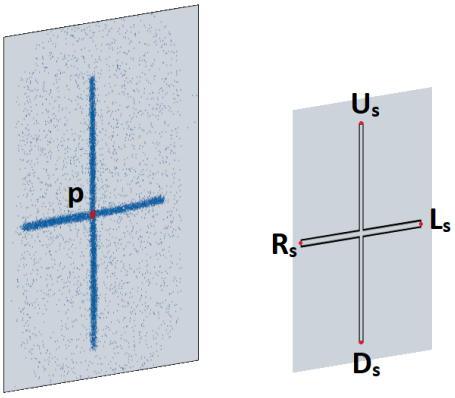

Figure 5.1: Definition of the positions used in the reconstruction of the location of the source.

5.1. Horizontal part of slit

For each detector a plane can be drawn through the center of the cross image and the middle of the horizontal part of the slits (see Figure 5.2 on the left). To create the obtained image, the source should lie in this plane. The plane can be described as follows:

$$\mathbf{c}_{h,i} \cdot \mathbf{x} = c_{h1,i}\,x + c_{h2,i}\,y + c_{h3,i}\,z = d_{h,i} \tag{5.1}$$

where $\mathbf{c}_{h,i}$ is the normal vector of the plane and where h denotes the use of the horizontal part of the slit and i denotes the number of the detector. The normal vector can be obtained using two vectors parallel to the plane. Therefore we use the vectors $\mathbf{a}_{h,i}$ and $\mathbf{b}_{h,i}$ which lie inside the plane:

$$\mathbf{a}_{h,i} = \mathbf{L}_{s,i} - \mathbf{p}_i \tag{5.2}$$

$$\mathbf{b}_{h,i} = \mathbf{R}_{s,i} - \mathbf{L}_{s,i} \tag{5.3}$$

The cross product of $\mathbf{a}_{h,i}$ and $\mathbf{b}_{h,i}$ creates a vector perpendicular to the plane, which is equal to the normal vector $\mathbf{c}_{h,i}$:

$$\mathbf{c}_{h,i} = \mathbf{a}_{h,i} \times \mathbf{b}_{h,i} \tag{5.4}$$

Since $d_{h,i}$ is a value which has to hold for all positions inside the plane, we can use any position that lies inside the plane to obtain this value. So let us use for instance $\mathbf{R}_{s,i}$:

$$d_{h,i} = \mathbf{c}_{h,i} \cdot \mathbf{R}_{s,i} \tag{5.5}$$

Since the source has to lie in each of these planes, we can combine the result of the three detectors to create a system of three equations with three unknowns:

$$\mathbf{A}_h \hat{\mathbf{x}}_h = \mathbf{d}_h \tag{5.6}$$

where $\hat{\mathbf{x}}_h$ is the reconstructed position of the source using the horizontal part of the slits and where

$$\mathbf{A}_h = \begin{bmatrix} \mathbf{c}_{h,1}{}^T \\ \mathbf{c}_{h,2}{}^T \\ \mathbf{c}_{h,3}{}^T \end{bmatrix} \tag{5.7}$$

$$\mathbf{d}_h = \begin{bmatrix} d_{h,1} \\ d_{h,2} \\ d_{h,3} \end{bmatrix} \tag{5.8}$$

The system can be solved as follows:

$$\hat{\mathbf{x}}_h = \mathbf{A}_h{}^{-1} \mathbf{d}_h \tag{5.9}$$

where $\mathbf{A}_h{}^{-1}$ is the inverse matrix of $\mathbf{A}_h$. Note that not every matrix is invertible.

This all can be visualized as follows (see Figure 5.2 on the right). We have a plane for each of the detectors. Two of these planes (for instance the ones of Detector 1 and 3, respectively in green and red) intersect in a line (in black), if they are not parallel. This line and the third plane (in yellow) intersect in a point, if they are not parallel. This is the reconstructed position of the source using the horizontal part of the slits. The case where two planes or the intersection line and a third plane are parallel corresponds to a not invertible matrix. The chances to end up with such parallelism is very small however, since there are so much less possibilities for the planes to be parallel, than for them to be not parallel. So usually this will not cause any problems.

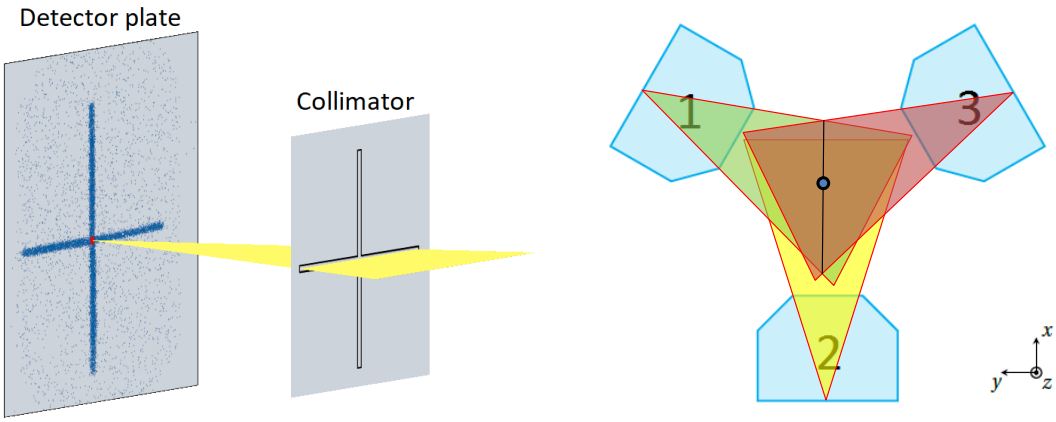

Figure 5.2: Reconstruction of the source position using the center of the cross images on the three detectors and the horizontal part of the cross slits. With on the left a 3D-sketch for one of the detectors and on the right a top view for the three detectors together.

5.2. Vertical part of slit

Something similar can be done using the vertical part of the slits. For each detector a plane can be drawn through the center of the cross image and the middle of the vertical part of the slits (see Figure 5.3 on the left). To create obtained image, the source should lie in this plane as well. To get the normal vector $\mathbf{c}_{v,i}$ we use the vectors $\mathbf{a}_{v,i}$ and $\mathbf{b}_{v,i}$:

$$\mathbf{a}_{v,i} = \mathbf{U}_{s,i} - \mathbf{p}_i \tag{5.10}$$

$$\mathbf{b}_{v,i} = \mathbf{D}_{s,i} - \mathbf{U}_{s,i} \tag{5.11}$$

$$\mathbf{c}_{v,i} = \mathbf{a}_{v,i} \times \mathbf{b}_{v,i} \tag{5.12}$$

with v denoting the use of the vertical part of the slit. $d_{v,i}$ is obtained using $\mathbf{D}_{s,i}$:

$$d_{v,i} = \mathbf{c}_{v,i} \cdot \mathbf{D}_{s,i} \tag{5.13}$$

To end up with the following system of equations:

$$\mathbf{A}_v \hat{\mathbf{x}}_v = \mathbf{d}_v \tag{5.14}$$

where $\hat{\mathbf{x}}_h$ is the reconstructed position of the source using the vertical part of the slits and where

$$\mathbf{A}_v = \begin{bmatrix} \mathbf{c}_{v,1}{}^T \\ \mathbf{c}_{v,2}{}^T \\ \mathbf{c}_{v,3}{}^T \end{bmatrix} \tag{5.15}$$

$$\mathbf{d}_{v,i} = \begin{bmatrix} d_{v,1} \\ d_{v,2} \\ d_{v,3} \end{bmatrix} \tag{5.16}$$

Which can be solved by:

$$\hat{\mathbf{x}}_v = \mathbf{A}_v{}^{-1} \mathbf{d}_v \tag{5.17}$$

This all can be visualized as follows (see Figure 5.3 on the right). We have a plane for each of the detectors. Since they are almost vertical they look like lines in the top view. Two of these planes (for instance the ones of Detector 1 and 3, respectively in green and red) intersect in a line, if they are not parallel. This line and the third plane (in yellow) intersect in a point, if they are not parallel. This is the reconstructed position of the source using the vertical part of the slits. Note that if the vertical part of the slits are perfectly vertically aligned, the line and the third plane are both vertical. This means that either the line lies inside the plane and the intersection is just the same line or the line lies outside the plane and they do not ever intersect. But since the chance that all slits are perfectly aligned is very small, the three planes usually intersect in a point.

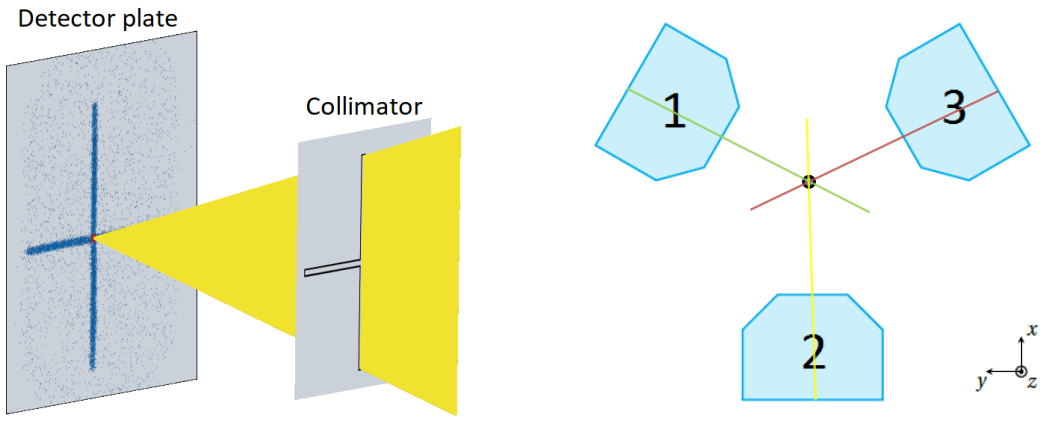

Figure 5.3: Reconstruction of the source position using the center of the cross images on the three detectors and the vertical part of the cross slits. With on the left a 3D-sketch for one of the detectors and on the right a top view for the three detectors together.

5.3. Combining the results

Now we have two reconstructed positions, one using the horizontal part of the slits and one using the vertical part. Each has its own strong points. The planes through the horizontal part of the slits have typically an angle smaller than 22° with the horizontal in our case. This means that an error in the center of the cross image will result in a bigger error in the horizontal direction than in the vertical direction. So the z-coordinate of this reconstructed position will be most accurate. The planes through the vertical parts of the slits are almost vertical. This means that an error in the center of the cross image will result in a bigger error in the vertical direction than in the horizontal direction. So the x and y-coordinates of this reconstructed position will be most accurate. As final reconstructed position, $\hat{\mathbf{x}}$, we combine the results by using the strong properties from each method:

$$\hat{\mathbf{x}} = \begin{bmatrix} \hat{x}_v \\ \hat{y}_v \\ \hat{z}_h \end{bmatrix} \tag{5.18}$$

5.4. Geometry of the setup

In order to solve for where the planes from the three detectors will intersect, one will have to know how the detectors are positioned with respect to each other. Therefore we measured the distances shown in Figure 5.4. These distances are measured with a tape measure at the height of the horizontal part of the slits. We used the distances shown on the left in the figure to reconstruct the positioning of the detectors. However, when measuring these distances, errors will be made, which leads to inconsistencies. This can be repaired by adjusting one of the distances, but that is not the most accurate way to solve this. Therefore we gave each distance a certain deviation of a few millimeter and tried multiple variations. To check the outcome we also used the distances shown in the figure on the right. Ultimately we chose the variation where the biggest deviation was smallest. For all the measured and reconstructed distances, see Appendix E.

Besides these distances we also measured the tilt of the detectors compared to the horizontal and used this when defining the planes for the reconstruction of the source position.

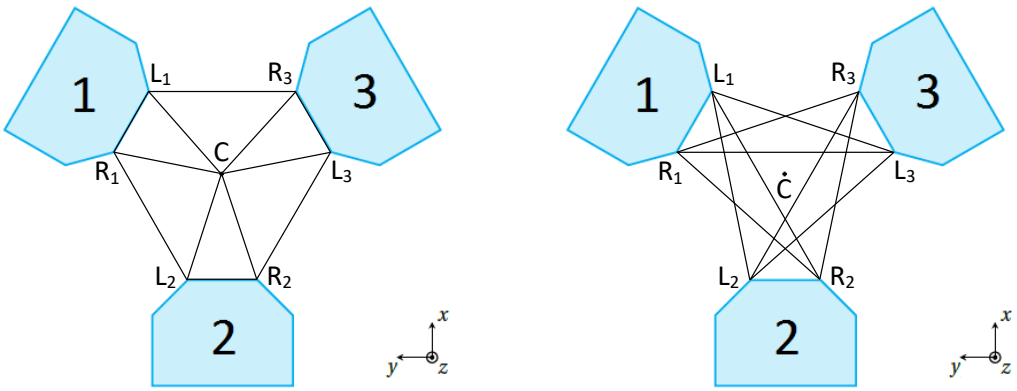

Figure 5.4: Measured distances to obtain the geometry of the setup. The ones on the left are used to reconstruct the geometry and the ones on the right are used as an additional check.

6

Results and discussion

6.1. Fixed positions

6.1.1. Maximum time frame length

^{57}Co source

We will first have a look at the results of reconstructing the position of the ^{57}Co source of 3.2 MBq for 98 fixed positions in air. We will first use the whole measurement time of 3 s as time frame length. We will compare the reconstructed positions with the positions determined by measuring the origin of the traversing device, from which it operates, and the orientation of its coordinate system compared to the chosen coordinate system with a tape measure. The latter will be referred to as the actual positions from now on. However, this does not mean that these positions are exact. Also in these positions there might be an error. Both the reconstructed and the actual positions are shown in Figure 6.2 on the left. As can be seen in the top view there is an almost constant horizontal offset, while in the side view one can see that for most cases the z-position is very accurate. The horizontal offset is most likely caused by an error made in measuring the geometry of the setup. The error might, however, be in the reconstructed positions or the actual positions. To correct for this, we determined the difference between the reconstructed origin, from the detections while measuring with the source at that position, and the actual origin, from measuring that same position with a tape measure. Since we know that these positions should coincide, we subtracted the difference from all reconstructed positions. Since we measured twice with the source at the origin, we used as reconstructed origin, the mean of the two reconstructions. The results of these corrected positions are shown in the figure on the right.

Let us now have a look at some quantitative results of the corrected, reconstructed positions. For each position we determined the absolute error of the reconstructed positions compared to the actual positions. This is done by determining for each position the difference in the x, y and z-direction between the reconstructed and actual position. Using the Pythagorean theorem, the total absolute error is found. This results in the charts shown in Figure 6.1 showing the probability to find an error within each interval and the probability to find an error smaller or equal to the upper limit of each interval, called the cumulative probability. Of all positions 75% are reconstructed within an error of 1 mm and 86% within 1.5 mm. The maximum error is 4.5 mm. For a more elaborate overview of the values, see Appendix F Section F.1.1. We also determined the horizontal and vertical component of the error, which are also present in the appendix.

Subsequently, we want to determine whether there is a dependency of the error on the x', y' and z'-position (see Figure 6.3). We have measured at seven positions along the x'-axis and seven positions along the y'-axis. Each is repeated at seven different z'-positions, leading to 98 positions. However, every $x' = y' = 0$ position is measured twice. To determine the dependency on the x'-position we take the 49 positions along the x'-axis and take for each x'-position the mean over the different z'-positions (shown in the first chart). For the dependency on the y'-position, the same is done for the 49 position along the y'-axis (shown in the second chart). To determine the dependency on the z'-position, the mean is taken over all x' and y'-positions at the same z'-position (shown in the third chart). The same is done for the horizontal and vertical component of the error.

In the first chart it can be seen that the farther away from $x' = 0$, the larger the error. The same can be said of the horizontal error, which most times has the largest contribution. Especially at the two outermost positions. For the vertical error there is no clear trend. At x' = -20 mm and x' = -10 mm the vertical error is

larger than the horizontal error. The second chart shows a similar behavior, with an increasing error farther away from y' = 0. However, for the negative y'-positions, the vertical error increases faster and becomes larger than the horizontal error. For the positive y'-positions it increases less and stays smaller than the horizontal error. The third chart shows for the horizontal error also a slight increase farther away from z' = 0. However, the vertical error decreases farther away from z' = 0 and peaks sharply at z' = 0.

If we now look more closely at the vertical errors at x' = -20 mm and x' = -10 mm, which can be found in Table F.5 in Appendix F, we see that there is for each a large error happening at z' = 0 causing the higher mean values. The high value is probably more a characteristic of the z'-dependency than that of the x'-dependency. While for the negative y'-positions we see high values through out all z'-positions, indicating that it is a characteristic of the y'-dependency.

So for both the x' and y'-dependency of both the horizontal and vertical error we saw an increase for positions farther away from the zero position. One explanation might be that when farther away from the origin, the distance to one of the detectors will increase, leading to less detections on that detector, which in order might lead to a larger inaccuracy in determining the center of the cross image, which will result in a larger error in the reconstruction of the source position. Another explanation might be that farther away from the origin, the errors in the measured geometry of the setup result in a larger error. Something else to notice is the asymmetry of the vertical error around y' = 0. This might be caused by the fact that the y'-axis is almost aligned with Detector 3, where the positive direction is towards the detector, while the negative direction is away from it. Since moving the source in the negative direction increases the distance to Detector 3 in a greater amount, than moving an equal distance in the positive direction will for the distance to Detector 1 and 2. Apparently this does not affect the horizontal error or to a lesser extent. Maybe the vertical error is more sensitive for one detector with significant less detections, the weakest link, than the horizontal error. When this experiment would have been performed not in air, but in the tank filled with water, the errors would have been higher, since the water would have absorbed a larger fraction of the photons, than the air does now. The water will also enhance the increase in the error when moving away from the zero position, since a longer path to one of the detectors, will in general also lead to a longer path through water and thus even less detections.

A possible explanation for the peak at z' = 0 in the vertical error is the following. At z' = 0 the source is approximately at the same height as the horizontal part of the three slits. Let us say, that the source is positioned slightly above the slits. Meaning that the three planes used to determine the z-position are almost horizontal, but slightly inclining towards the source. However, a small error in the position of the center of the cross image might result in one of the planes declining towards the source. The planes will now intersect somewhere completely different. Position 45 at (x', y', z') = (-10, 0, 0) mm which should be reconstructed at (x, y, z) = (8.69; 4.94; 0.03) mm was for instance reconstructed at (x, y, z) = (3656.8; -1468.7; 4.46) mm, somewhere way beyond Detector 3. But since the planes are almost horizontal, the vertical error is still in the order of millimeters, while the horizontal error is of the order of meters. But as soon as the source is several millimeters above or below the horizontal part of the slits, the chance of this happening is negligible, resulting in lower vertical errors at the other z'-positions. What the reason is for the further decrease in the vertical error when moving farther away from z' = 0, is not clear. One would expect with the source moving farther away the error would increase, due to a decrease in the number of detections. This behavior is shown by the horizontal error, although it does not increase very much.

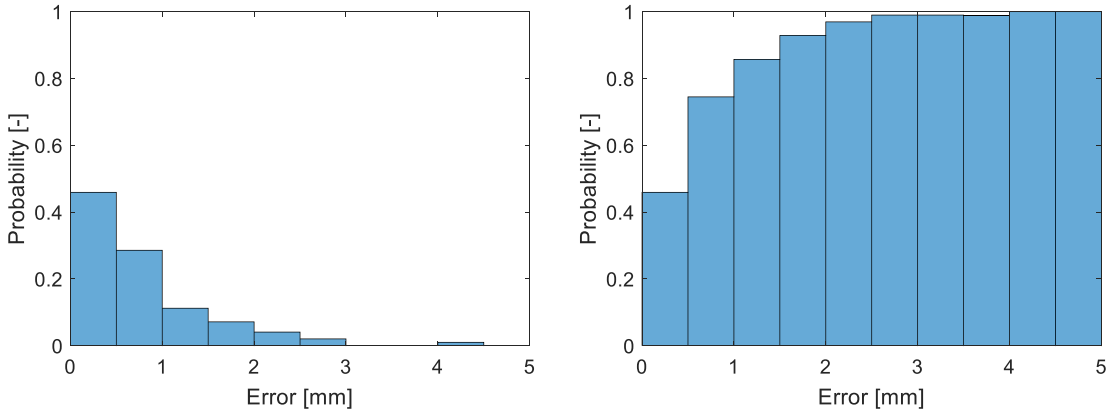

Figure 6.1: Probability distribution of the error made in the reconstruction of the 98 positions of the ^{57}Co source of 3.2 MBq with a time frame length of 3 s shown on the left and the cumulative probability distribution shown on the right.

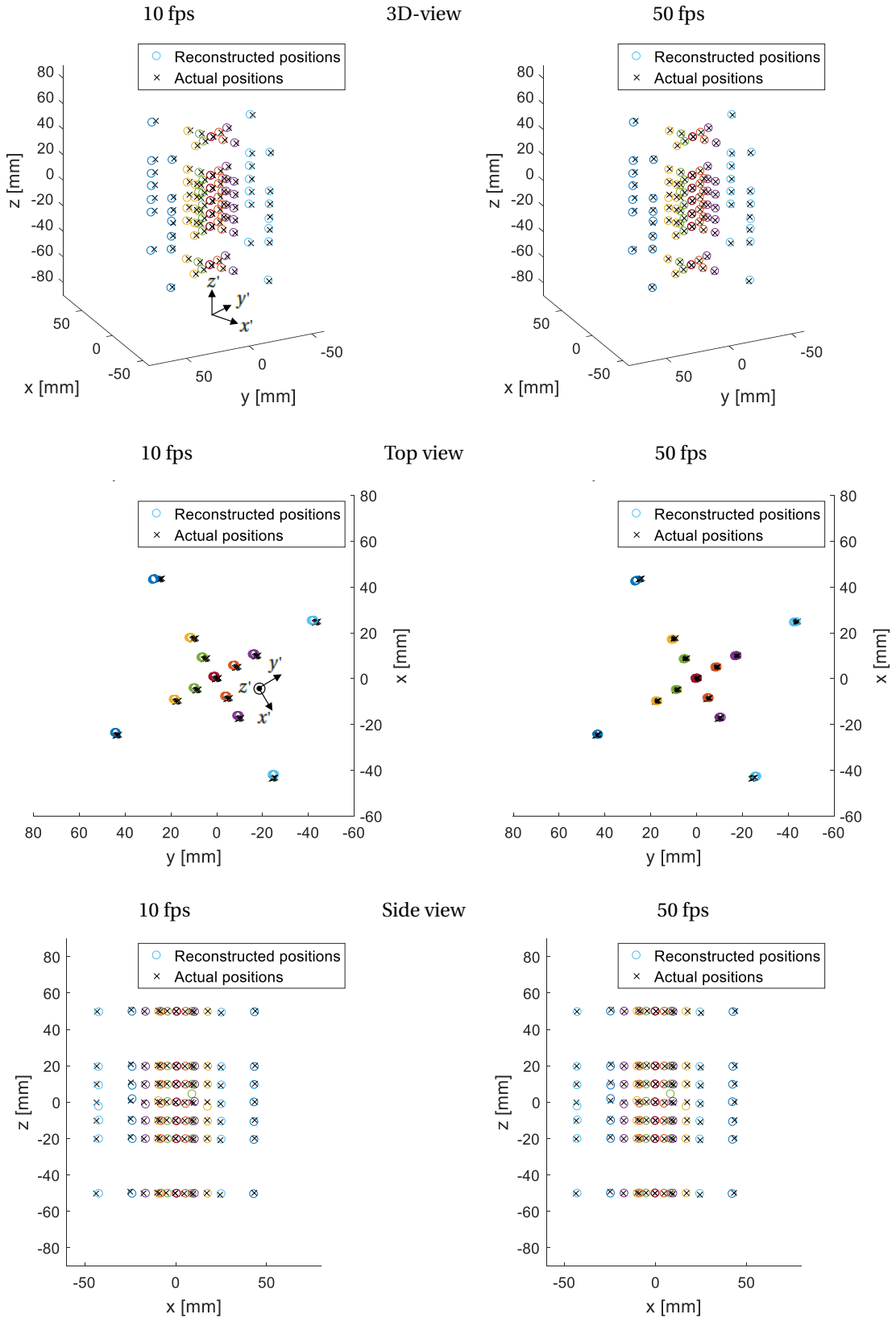

Figure 6.2: With on the left the reconstructed positions of a ^{57}Co source of 3.2 MBq at 98 fixed positions using a time frame length of 3 s, represented by circles. These are plotted together with the actual positions, represented by crosses. With at the top a 3D-view including the orientation of the coordinate system of the traversing machine, in the middle a top view also including the coordinate system of the traversing machine and at the bottom a side view. On the right there is corrected for the offset of the reconstructed origin.

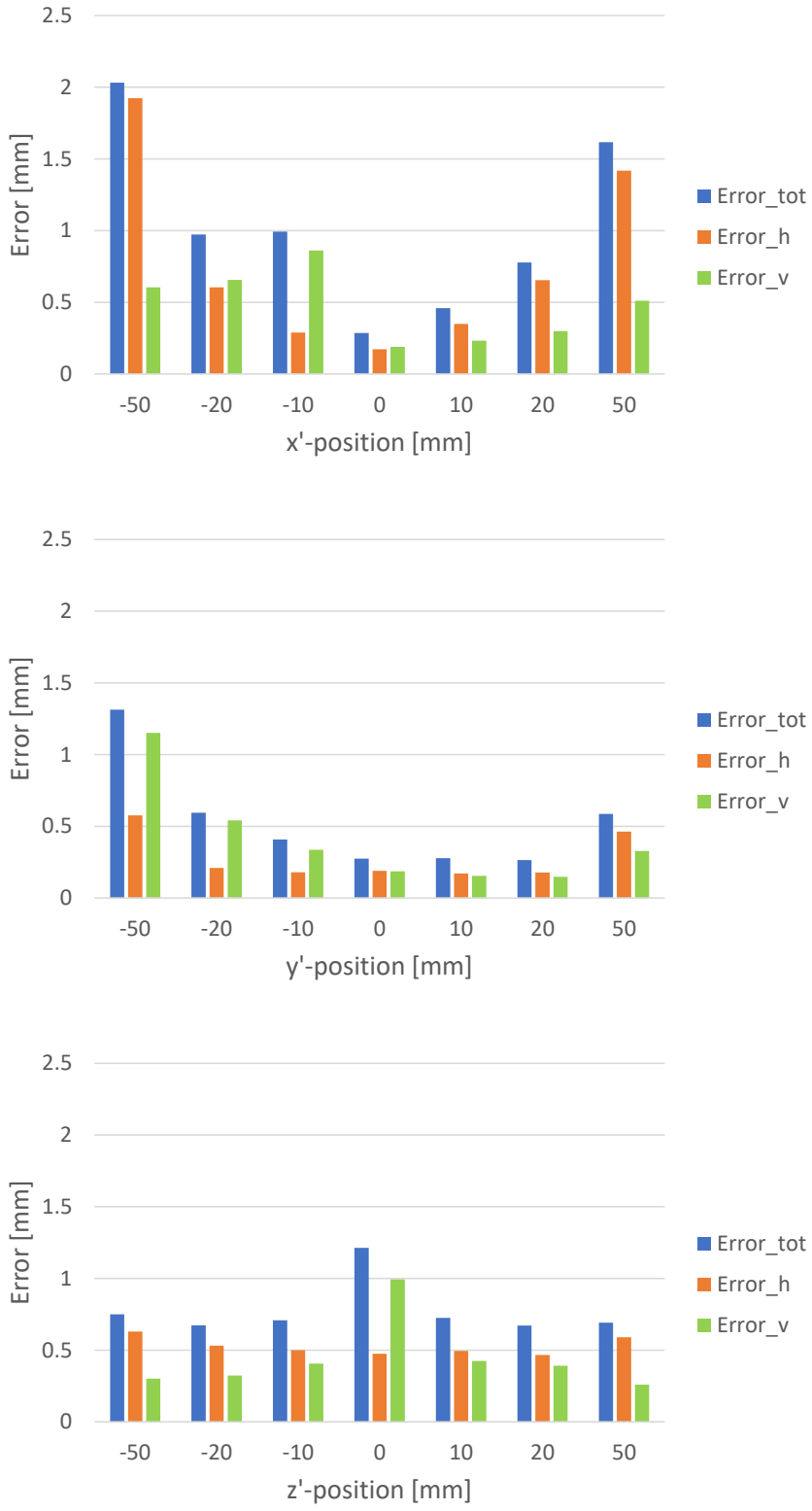

Figure 6.3: The absolute error, $Error\_tot$, of the corrected, reconstructed positions compared to the actual positions of the ^{57}Co source using a time frame length of 3 s. Also divided into the horizontal and vertical component, $Error\_h$ and $Error\_v$. With at the top the mean taken over the different z'-positions for the position along the x'-axis. With in the middle the mean taken over the different z'-positions for the position along the y'-axis. And at the bottom the mean taken over all the positions for the different z'-positions.

^{198}Au source

We will now have a look at the results of reconstructing the position of the ^{198}Au source of 69 MBq for 240 fixed positions in air. The range is slightly bigger than the one used for the ^{57}Co source. Also at some intermediate positions the source is measured. For example, at z' = -25 mm which corresponds approximately to the height where the stirrer or the rotator will be during the next experiments. We will first use the whole measurement time of 1 s as time frame length. We will again compare the reconstructed position with the actual positions. The results are shown in Figure 6.5 on the left. As can be seen in the top view there is an almost constant horizontal offset, but this time we see in the side view an even bigger offset in the z-positions. The offset, or at least part of it, is most likely caused by an error made in measuring the geometry of the setup, resulting in the reconstructed or actual position. However, there might be two additional causes. Firstly, between this and the previous experiment, we have adjusted the distance between the slit and the detector plate, after which we have set it back. We checked some distances to verify that the geometry of the setup had not changed. Most distances where measured identically. For the ones that seemed to have changed, the difference was within the inaccuracy of measuring with a tape measure. So we assumed nothing had substantially changed. Secondly, we switched to another source. Because the ^{198}Au source was put in a special holder, resulting in some additional height, the transversing device had to be adjusted to keep the origin at the same height. Maybe an error was made in doing so. To correct for the offset, the difference between the reconstructed origin and the actual origin is subtracted. These results are shown in the figure on the right.

Again, we determined for each position the absolute error of the reconstructed positions compared to the actual positions. This results in the charts shown in Figure 6.4 showing the probability and the cumulative probability distributions. Of all positions now only 45% are reconstructed within an error of 1 mm, but 68% within an error of 1.5 mm and the maximum error is 4.5 mm as well. For a more elaborate overview of the values, see Appendix F. We also determined the horizontal and vertical component of the error, which are also present in the appendix.

The three charts in Figure 6.6 show the dependency of the error and its horizontal and vertical component on respectively the x', y' and z'-position. The first shows a similar dependency on the x'-position as we saw before for the ^{57}Co source, increasing errors for positions farther away from x' = 0 and with the horizontal component increasingly dominant. The second chart shows for the negative y'-positions a similar trend, but then with both components of the same order. The errors for the positive y'-positions are almost constant. It looks similar to the behavior of the y'-dependency of the vertical error for the ^{57}Co source, but now it also holds for the horizontal error. The third chart does not show a clear trend for the z'-dependency. Both components vary somewhat, as does the total error.

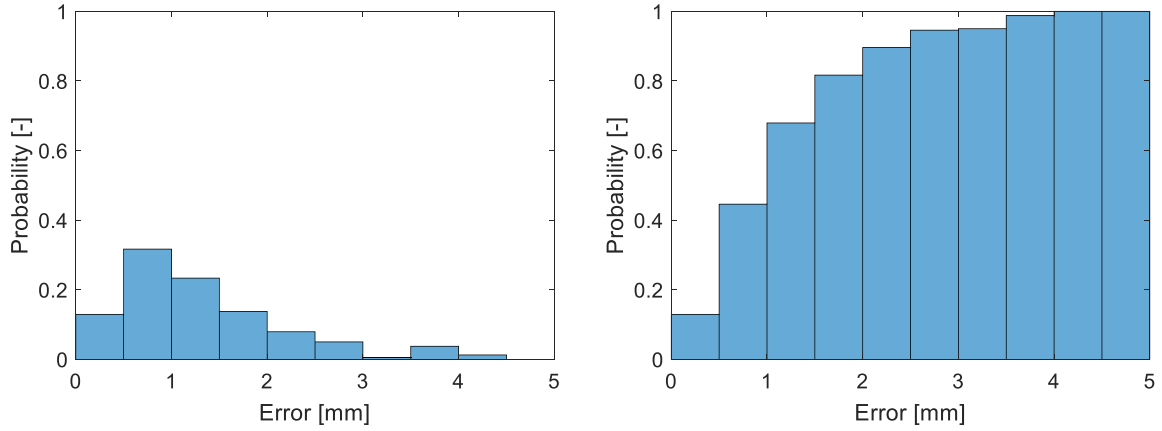

Figure 6.4: Probability distribution of the error made in the reconstruction of the 240 positions of the ^{198}Au source of 69 MBq with a time frame length of 1 s shown on the left and the cumulative probability distribution shown on the right.

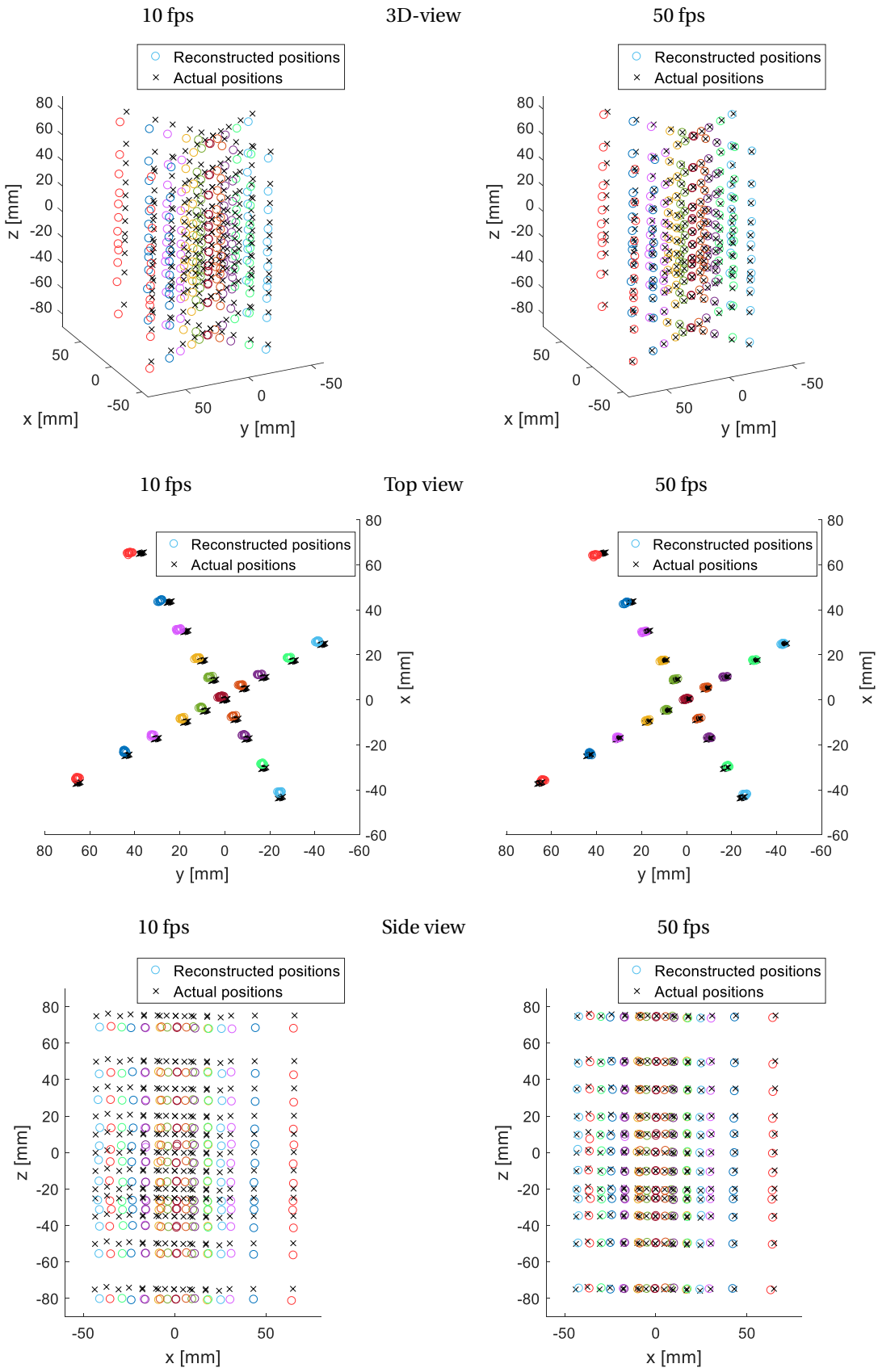

Figure 6.5: With on the left the reconstructed positions of a ^{198}Au source of 69 MBq at 240 fixed positions using a time frame length of 1 s, represented by circles. These are plotted together with the actual positions, represented by crosses. With at the top a 3D-view, in the middle a top view and at the bottom a side view. On the right there is corrected for the offset of the reconstructed origin.

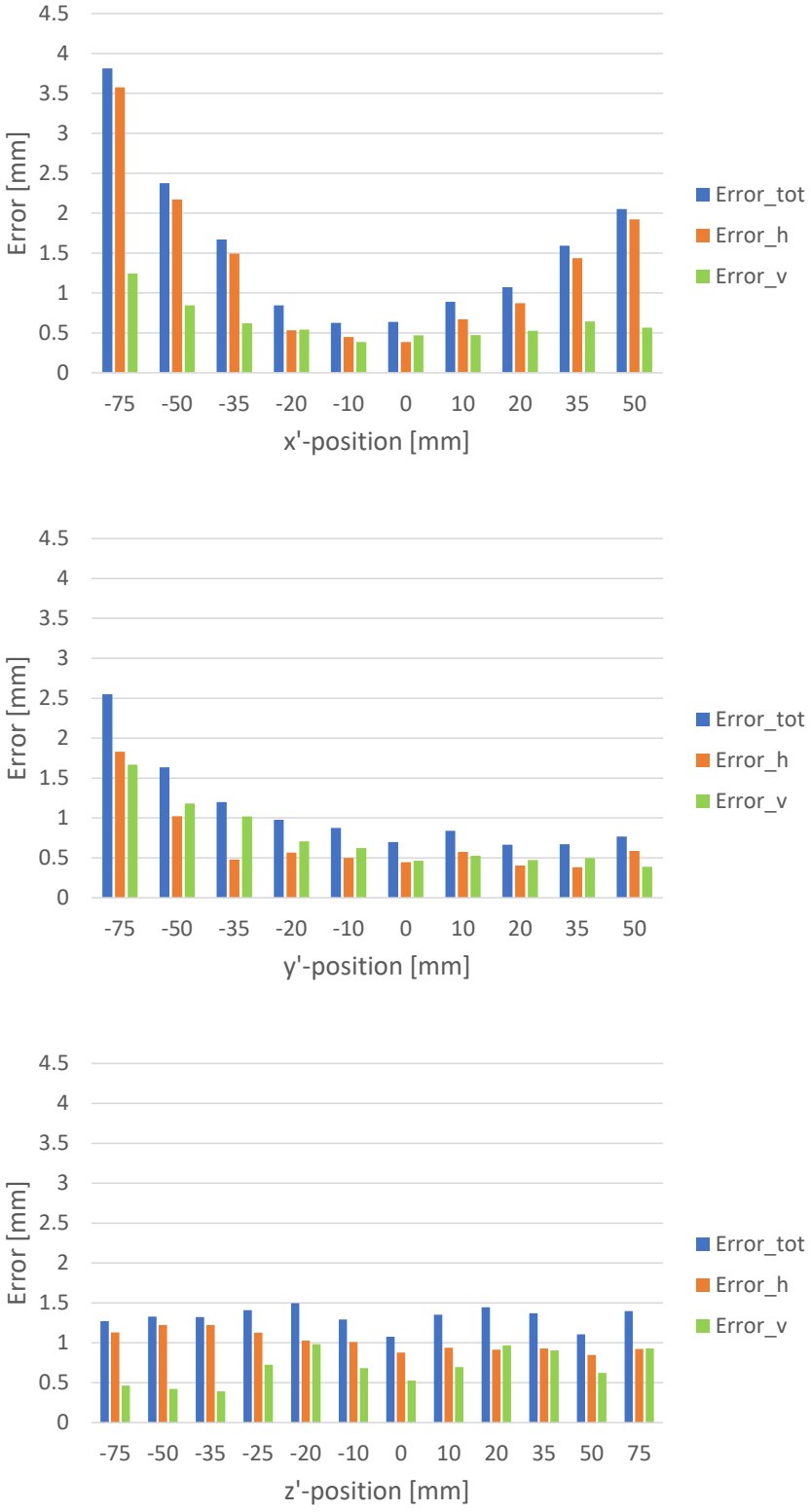

Figure 6.6: The absolute error, $Error\_tot$, of the corrected, reconstructed positions compared to the actual positions of the ^{198}Au source using a time frame length of 1 s. Also divided into the horizontal and vertical component, $Error\_h$ and $Error\_v$. With at the top the mean taken over the different z'-positions for the position along the x'-axis. With in the middle the mean taken over the different z'-positions for the position along the y'-axis. And at the bottom the mean taken over all the positions at the different z'-positions.

6.1.2. Increasing frame rates

Next thing we want to do is to see how the error changes when we decrease the time frame length we use, or in other words increase the frame rate. Although the source now was fixed at a position, in the next experiments the source will be moving. To reduce the effect of motion blur, higher frame rates are required. So we will divide the measurements into multiple frames and for each reconstruct the position of the source. When possible at least. Sometimes the center of the cross image can not be determined, resulting in a reconstructed position that is not a number (NaN). For some of the reconstructions the error is so big, that it is labeled as an outlier and deleted. Otherwise it would influence the following results too much. The outliers are, however, only deleted for all the quantitative results. In the plots showing the reconstructions, they are still included. The labeling is done using the modified Z-score. The normal Z-score is defined as:

$$Z_i = \frac{x_i - \overline{x}}{\sigma} \tag{6.1}$$

where Z_i is the Z-score of the i^{th} element, x_i, of the data set, $\overline{x}$ is the mean value and σ is the standard deviation of the data set. The Z-score expresses the difference between an element and the mean of the data set in the number of standard deviations. However, when the outliers are too big, they influence the mean and the standard deviation so much that they will not be recognized as outliers. That is why we will use the modified Z-score, which is defined as:

$$M_i = \frac{x_i - \tilde{x}}{MAD} \tag{6.2}$$

where M_i is the modified Z-score of the i^{th} element, x_i, of the data set, $\tilde{x}$ is the median of the data set and MAD is the so called median absolute deviation, which is defined as:

$$MAD = median\left(|x_i - \tilde{x}|\right) \tag{6.3}$$

Both the median and the MAD are much less influenced by large outliers. We will use this modified Z-score for the absolute error of the reconstructions. Errors with modified Z-scores with an absolute value greater than 3.5 are labeled as outliers.

^{57}Co source

In Figure 6.7 the results are shown for the ^{57}Co for a frame rate of 10 and 50 fps. Since the total measurement time is 3 s, the number of reconstruction per positions is three times the frame rate. We see the blob of reconstructions of each position become bigger when the frame rate increases, meaning that the errors made become bigger, as is expected. In the top view we see that the horizontal error is in each horizontal direction more or less the same. While in the side view we see that the vertical error is smaller than the horizontal error. We see also some reconstructions outside these blobs, corresponding to a bigger vertical error. The positions are plotted together with the reconstructed positions using the maximum time frame length of 3 s. For the dependency of the error on frame rate, we will calculate the error of the reconstructed positions with higher frame rates compared to these positions instead of the actual positions. This to exclude errors caused by faulty measured geometry of the setup, so that it will only show the additional spreading of the reconstructions due to increasing frame rates.

In Figure 6.9 at the top the mean of this error is shown for different frame rates. The mean is taken without the frames that gave NaN or were assigned as outlier. This results, however, in positions with less frames giving a reconstruction which contributes in the mean. Therefore we first took the mean error per positions and then the mean over all positions, such that the error at each position, instead of each frame, contributes equally. The same is done for the horizontal and vertical component. Both components increase almost linearly with increasing frame rates. However, after 30 fps it seems to flatten. For all frame rates the horizontal error is bigger than the vertical error. Another interesting feature to look at is how the biggest error changes for increasing frame rates. One might just look then at the maximum error, but this value tends to fluctuate a lot. Therefore we choose to look at the error below which 95% of the errors made will be. We will refer to this as the 95% error. This error is also determined for the horizontal and vertical component. This is shown in the figure in the middle. The values are higher, but show the same behavior as the mean. A difference is that for frame rates up to 20 fps, the vertical error is larger than the horizontal error. Notice that the different errors do not necessarily happen for the same reconstruction. In the figure at the bottom the percentage of frames that give NaN or are labeled as an outlier and the sum of these two are shown for different frame rates. For 5 up to 20 fps there are (almost) no NaNs and about 4% of the frames are assigned as outliers. When the frame rate

is increased further, the percentage of NaNs rapidly increases. With at 50 fps, 49% of the frames give NaN. Because of the low activity of the ^{57}Co source, relatively little detections are done per second. However, due to the good blocking by the collimator little are needed to find the center of the cross image accurately. But when the frame rate is increased too much, no detections are left by the filters that are used, which will result in NaN. This probably also causes the decrease in outliers, since there are less frames giving a position which can be assigned as an outlier. When we look at the number of detections per time frame when using a frame rate of 25 fps, we see that NaNs start occurring when one of the detectors has less than 150 detections during one time frame. This is, however, for a stationary source. When the source starts moving, motion blur will cause NaNs occurring even with more than 150 detections per time frame. But whether it is beneficial to decrease the frame rate to obtain more detections per time frame or to increase the frame rate to decrease the effect of motion blur, will probably depend on the velocity of the source, because the effect of motion blur increases for higher velocities.

^{198}Au source

In Figure 6.8 the results are shown for the ^{198}Au source for a frame rate of 10 and 50 fps. Since the total measurement time is 1 s, the number of reconstruction per positions is now equal to the frame rate. The results are similar as for the ^{57}Co source, except that now for the 50 fps we see outside the blobs also a lot of reconstructions with much bigger errors. While for the ^{57}Co source we only saw a few with a bigger vertical error, we now also see a lot with bigger horizontal errors.

In Figure 6.10 at the top the mean of the error over all frames of all 240 positions is shown for different frame rates and again together with the horizontal and vertical component. Both components increase again almost linearly with increasing frame rates. But this time, it seems not to flatten after 30 fps. And again for all frame rates the horizontal error is bigger than the vertical error. Both errors are slightly bigger though, compared to those of the ^{57}Co source. The behavior of the 95% error, shown in the figure in the middle, is similar as for the mean error. The horizontal error bigger than the vertical error for all frame rates and both increase linearly. The horizontal errors are bigger than those of the ^{57}Co source for all frame rates. The vertical errors are bigger as well, but only for the low and high frame rates. In the range from 15 up to 35 fps those of the ^{57}Co source are bigger. In the figure at the bottom the percentage of frames that give NaN or are labeled as an outlier and the sum of these two are shown for different frame rates. For 5 up to 15 fps the percentage of outliers is a bit larger, but decreasing and there are again no NaNs. At 20 fps the results are almost the same, 4% outliers and no NaNs. For higher frame rates the percentage of outliers increases again. Which is a good thing in a bad situation, since we saw all those reconstructions with very large errors. The percentage of NaNs stays almost at zero now. This is caused by the higher activity of the ^{198}Au source. A lot of detections are done and also necessary to accurately determine the center of the cross image, due to the many additional detections of photons passing right through the collimator. Increasing the frame rate will decrease the accuracy, but the frame rate has to increase much more to decrease the number of detections per time frame such that no detections will be left by the filter and result in NaN. The minimum number of detections will, however, be higher than the 150 detections we found for ^{57}Co, due to the additional photons passing through the collimator.

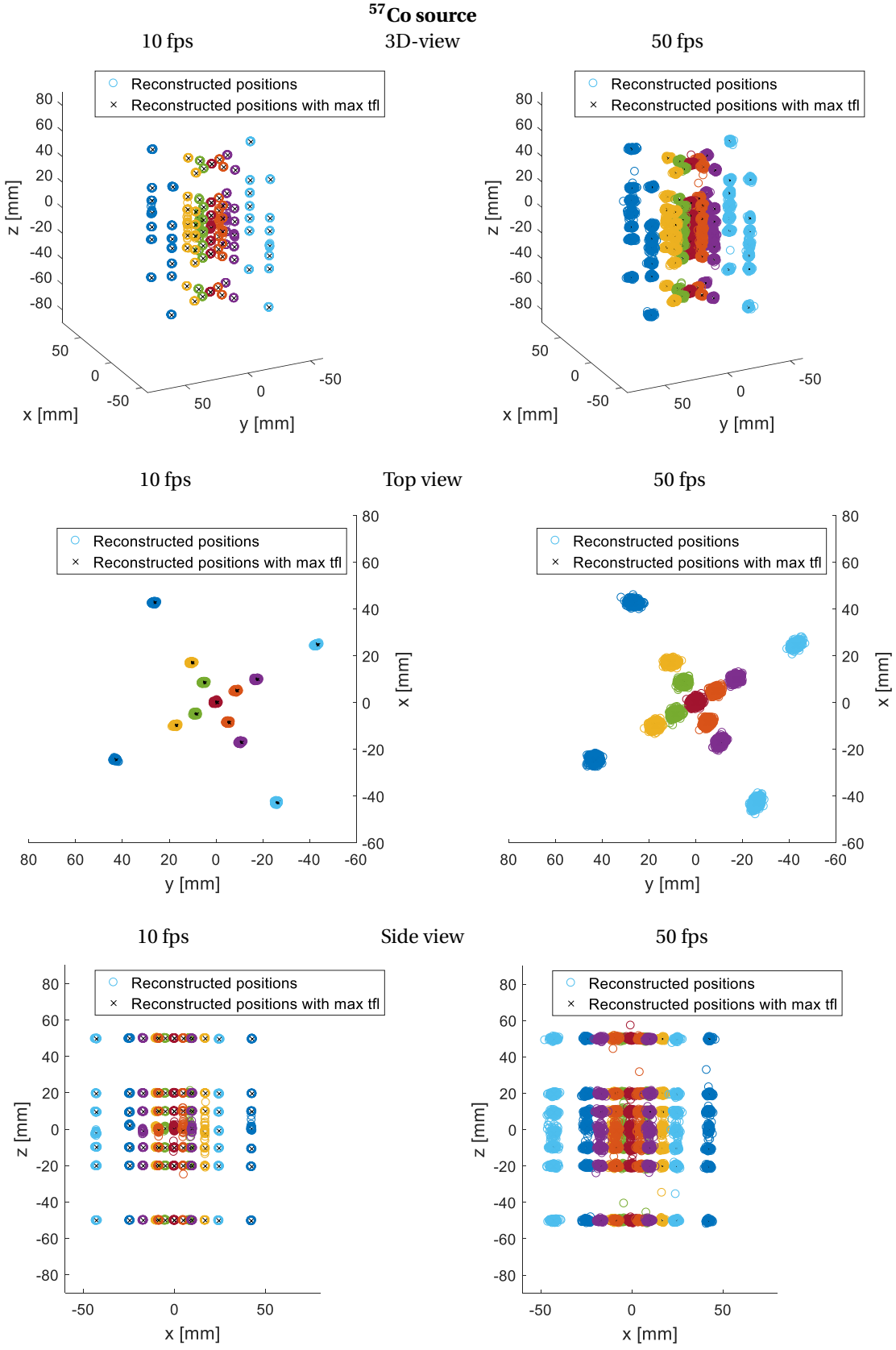

Figure 6.7: With on the left the reconstructed positions of a ^{57}Co source of 3.2 MBq at 98 fixed positions for a frame rate of 10 fps and on the right for 50 fps, represented by circles. These are plotted together with the reconstructed positions using the maximum time frame length of 3 s, represented by crosses. With at the top a 3D-view, in the middle a top view and at the bottom a side view.

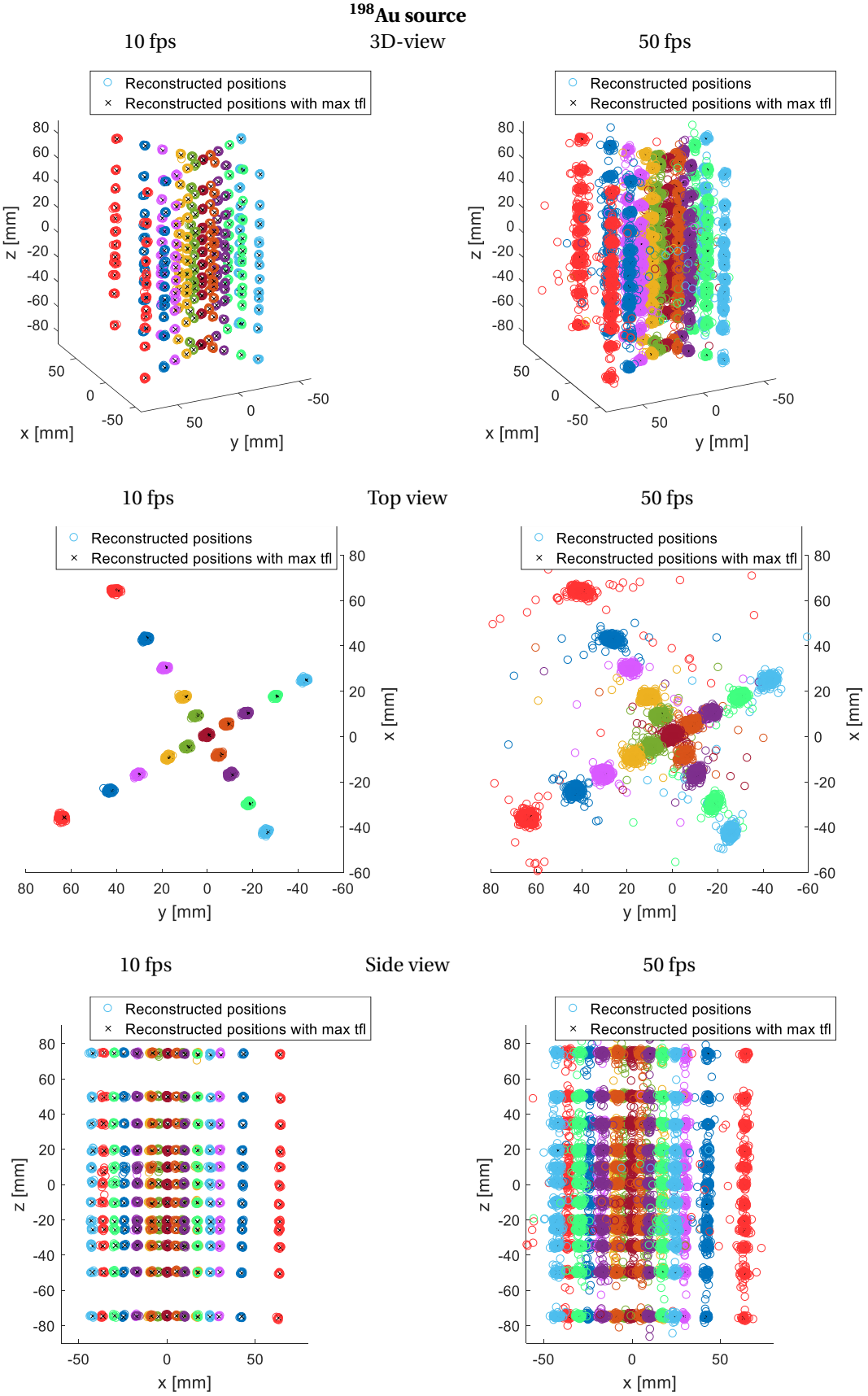

Figure 6.8: With on the left the reconstructed positions of a ^{57}Co source of 3.2 MBq at 98 fixed positions for a frame rate of 10 fps and on the right for 50 fps, represented by circles. These are plotted together with the reconstructed positions using the maximum time frame length of 3 s, represented by crosses. With at the top a 3D-view, in the middle a top view and at the bottom a side view.

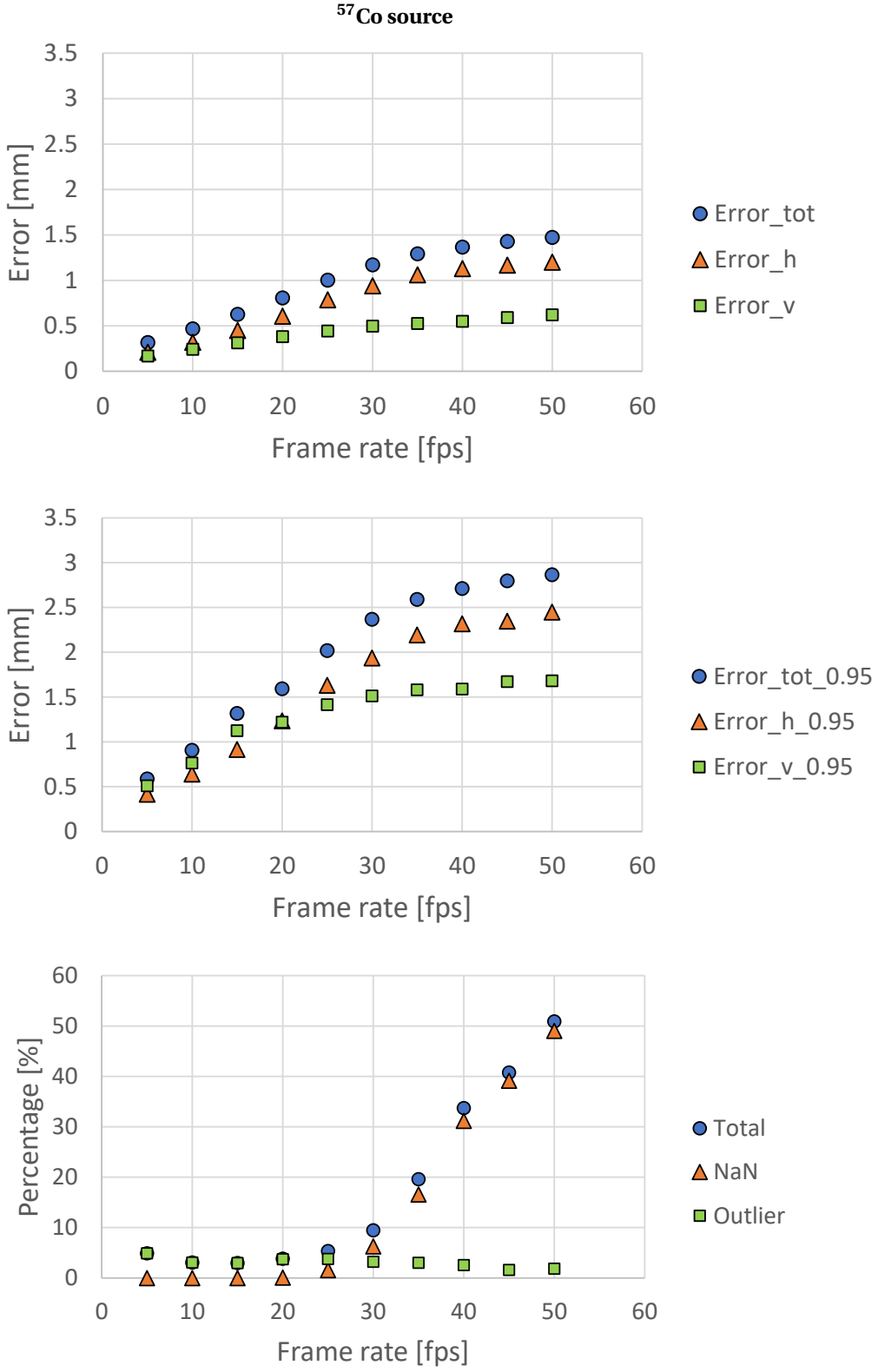

Figure 6.9: At the top the mean error in the reconstructed position of the 98 positions of the ^{57}Co source, also showing the same for the horizontal and vertical errors. In the middle the error below which 95% of the errors are, also shown for the horizontal and vertical errors. And at the bottom the percentage of all frames of all positions which give NaN or are labeled an outlier and the total of those two, each for different frame rates.

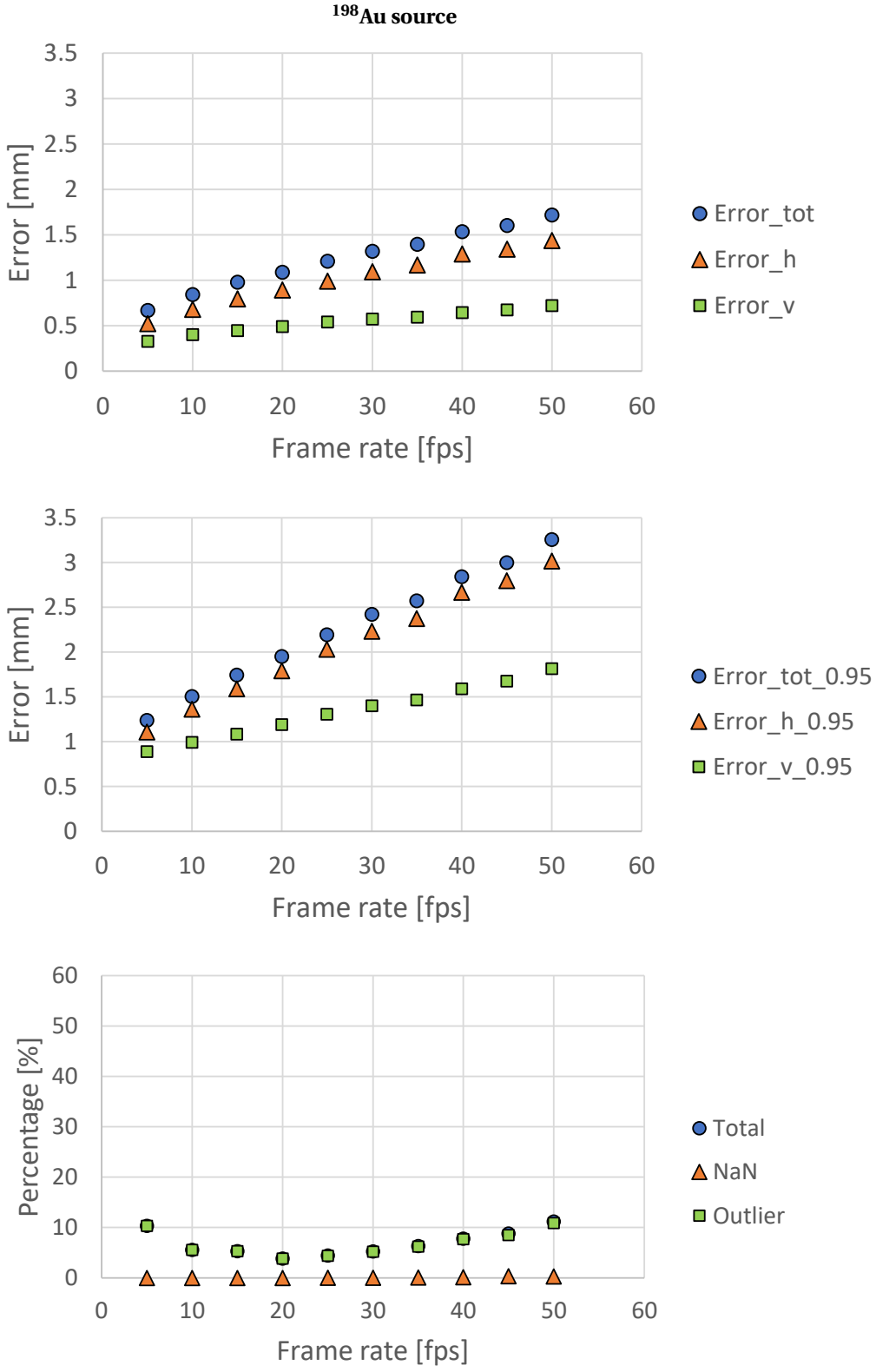

Figure 6.10: At the top the mean error in the reconstructed position of the 240 positions of the ^{198}Au source, also showing the same for the horizontal and vertical errors. In the middle the error below which 95% of the errors are, also shown for the horizontal and vertical errors. And at the bottom the percentage of all frames of all positions which give NaN or are labeled an outlier and the total of those two, each for different frame rates.

6.2. Moving along a known circular trajectory

Now we will have a look at the results of reconstructing the position of the ^{198}Au source of 45 MBq moving along a known circular trajectory in water. We repeated the experiment for various radii and rotational speeds. We do not know where along the trajectory the source is during the measurement. Therefore we cannot calculate the exact error of the reconstructions and use this to filter out the most extreme outliers. We know with which velocity it is moving, what the radius is of the circular trajectory, at which height it is moving and in which direction. We can use this to filter out reconstructions that conflict with this information and would otherwise influence the results too much. The filters are not set too strict such that we will also get a view on the errors that are made.

When reconstructing the positions, we have to decide which frame rate to use. For each radius and rotational speed, we tried several frame rates, in order to find for each the optimal frame rate. In the next section the results using these optimal frame rates are discussed.

6.2.1. Using the optimal frame rate

Let us first have a look at the reconstructions for the circular motion with the largest radius (38.8 mm) and a rotational speed of 30 rpm, resulting in a tangential velocity of 122 mm/s, while using a frame rate of 20 fps. Several top views are shown in Figure 6.11a through c. In each plot the reconstructions of all time frames, except the ones that resulted in NaN or an outlier, are represented by blue dots. In each plot a different set of five successive time frames is highlighted, by making them larger. The larger the size, the more recent the time frame. Also the circle fitted through all positions and the actual circle are shown. Since we already found out in the previous experiment if there were any offsets in the reconstructed positions, we now placed the actual circle concentric with the fitted circle.

In Figure 6.11a one can see five successive time frames being highlighted, each lying approximately on the actual circle and almost equally spaced. However, not every reconstruction lies on the circle as can be seen by the highlighted time frames in Figure 6.11b. Even though there is some radial spreading, the fitted circle almost coincides with the actual circle. In Figure 6.11c only two time frames are highlighted, because the other three time frames gave NaN or were assigned as an outlier.

In Figure 6.11d through f the results are shown for the motion with the smallest radius (10.3 mm) and a rotational speed of 113 rpm, resulting in a tangential velocity of 122 mm/s as well, while using a frame rate of 25 fps. Notice that due to different measuring times and frame rates, the number of time frames is not the same for both cases. The same holds for the number of reconstructions, which is besides that also affected by the number of NaNs and outliers. The radial spreading of the reconstructions is very similar, however, the fitted circle now is slightly too big. In Figure 6.11d five time frames are shown which lie approximately at the actual circle. However, not every reconstruction goes that well. In Figure 6.11e it seems as if the source suddenly jumps to the other side of the circle. Normally this reconstruction would be filtered out. But now the time frame before this one gave NaN or was deleted because it was labeled as an outlier. Because of this some of the filters are not able to recognize this one as an outlier anymore, since they need to compare the current time frame with the previous one. Due to this it is also possible to find reconstructions that seem to show that the source is moving counterclockwise for a short time, as is shown in Figure 6.11f. Another consequence of these unrecognized outliers, is that they might cause a successive, accurate reconstruction to be labeled as outlier, because compared to the unrecognized outlier it looks like an outlier.

Now we are going to look how the tangential velocity of the source influences the reconstructions. In Figure 6.12a through c we see the three different radii, but each with tangential velocity of 122 mm/s. While in Figure 6.12d through f it is 451 mm/s. For each radius we see a larger radial spreading for a higher velocity. However, keeping the fitted circle equally accurate, except for the smallest radius. Due to some quite big outliers the circles is fitted too big. These reconstructions were not recognized as outliers though. Probably because the time frames preceding these resulted in NaN or an outlier.

In Figure 6.13 the side views are shown. We see the same behavior for the vertical spreading, which increases for higher velocities. Especially for the smallest radius again. However, it makes the error in the z-position smaller, since the fit and the actual circle are now overlapping, while the error for the larger radii stays the same.

Besides plotting the reconstructions in 3D, we can also look at each coordinate separately as a function of time. Such plots are shown in Figure 6.14 for the case with the largest radius (38.8 mm) and a rotational speed of 30 rpm, while using a frame rate of 20 fps. In both the plots of the x and y-coordinate we can clearly recognize the sinusoid one would expect for a circular motion, despite the small deviations and the gaps. In

the plot of z-coordinate we see random fluctuations around a constant value. If we now look at the case with the smallest radius (10.3 mm) and a rotational speed of 418 rpm, while using a frame rate of 35 fps, shown in Figure 6.15, we are not able to recognize a sinusoid for the x and y-coordinates. Besides that the deviations are much bigger, there are only five time frames per revolution. Which would make it hard to recognize even without any deviations. For the z-coordinate we see a larger spreading.

In Figure 6.16 some quantitative results are shown. Since we do not know where on the trajectory the source is during the measurements, we also do not know the exact error in the reconstructions. But with what we do know, we calculated for each radius at each velocity, the error of the radius of the fitted circle, the mean of the absolute radial error of the reconstructions compared to the actual circle, the error of the z-position of the fitted circle and the mean of the absolute error of the z-position of the reconstructions compared to the z-position of the actual circle. Both errors of the fit can be positive and negative. Where positive means a too large fitted radius or a too high fitted z-position, and negative means a too small fitted radius and a too low z-position. These errors say something about the overall tendency of the reconstructions. The mean absolute errors are a measure of the spreading in the errors, although they do not distinguish the direction of the error. Therefore they are always positive. The mean radial error is an underestimation for the mean horizontal error though. But this one we can not calculate.

For each radius we see that for all velocities the radius of the fitted circle increases for higher velocities, except for the highest velocities of the medium circle. For the smallest two radii this means that the error becomes larger, since the radii were already too big. The largest circle was fitted too small and thus it is leading to a smaller error. But if we would increase the velocity even further, the radius will probably become too big and the error starts increasing as well. The mean radial error increases for increasing velocities as well, which agrees with what we have seen in the plots in Figure 6.12. The highest velocity of the medium circle is, however, an exception again. Besides this one, the mean radial errors for the different radii are very similar. The error in the z-position of the circle does not change that much. For all radii and for all velocities the error is negative, meaning the circle is fitted below the actual circle. Except for the highest velocity of the smallest radius. There the error is almost zero, but positive. Since the z-position of the rotator was hard to set accurately, it might as well be caused by an error in the actual position. This might explain why the errors do not differ that much between the two smallest radii, but it does not explain why the error for the largest radii is bigger. The mean error of the z-position increases as well for each radius for increasing velocities, which agrees with what we have seen in the plots in Figure 6.13.

In Figure 6.17 the percentage of NaNs and outliers and the total of these two are shown for each radius at each velocity. For the smallest two radii, the percentage of NaNs first decreases for increasing velocities, but starts increasing for the highest velocities. Even though, in general a higher frame rate was used for higher velocities, as is shown in Figure 6.18 (more on that later), the traveled distance in one time frame still increased. So one would expect that due to motion blur, the percentage of NaNs would only increase with increasing velocities. What causes the decrease is not clear. The percentages for the smallest radius are in most cases almost twice as big as for the medium radius. The percentage of NaNs for the largest radius shows just the opposite, first a small increase and after that a decrease. We have neither for this an explanation. The percentage of outliers fluctuates quite a lot per velocity, but there is no clear trend visible. The same holds for the total of the two, since the percentage of outliers is for almost all cases larger than the percentage of NaNs.

To choose which frame rate is optimal for each radius at each velocity, we tried different frame rates for each. Then we tried to find the frame rate with the best results for both the errors and the percentage of NaNs and outliers. When different frame rates gave similar results, we chose the highest frame rate and thus the one with the most reconstructions. As can be seen in Figure 6.18, the optimal frame rate tends to increase for higher velocities. So for higher velocities, the effect of motion blur becomes more important than the effect of less detections due to higher frame rates. It also seems that for smaller radii a higher frame rate is optimal. This might have something to do with the higher curvature of the trajectory, increasing the effect of motion blur.

So for higher velocities one wants to use a higher frame rate. But during the next experiment with the source moving freely, we do not know how fast the source will be moving and its velocity will probably change in time. So which frame rate to choose then? One might use the velocity of the previous time frame(s) to predict the velocity of the next and choose accordingly the frame rate and thus making it variable. We did not get this far. We wanted first to try using one fixed frame rate. We decided to use 20 fps. For this frame rate, both the highest and lowest velocities seem to give reasonable results, although for these it is not the optimal frame rate. The results are discussed in the next section.

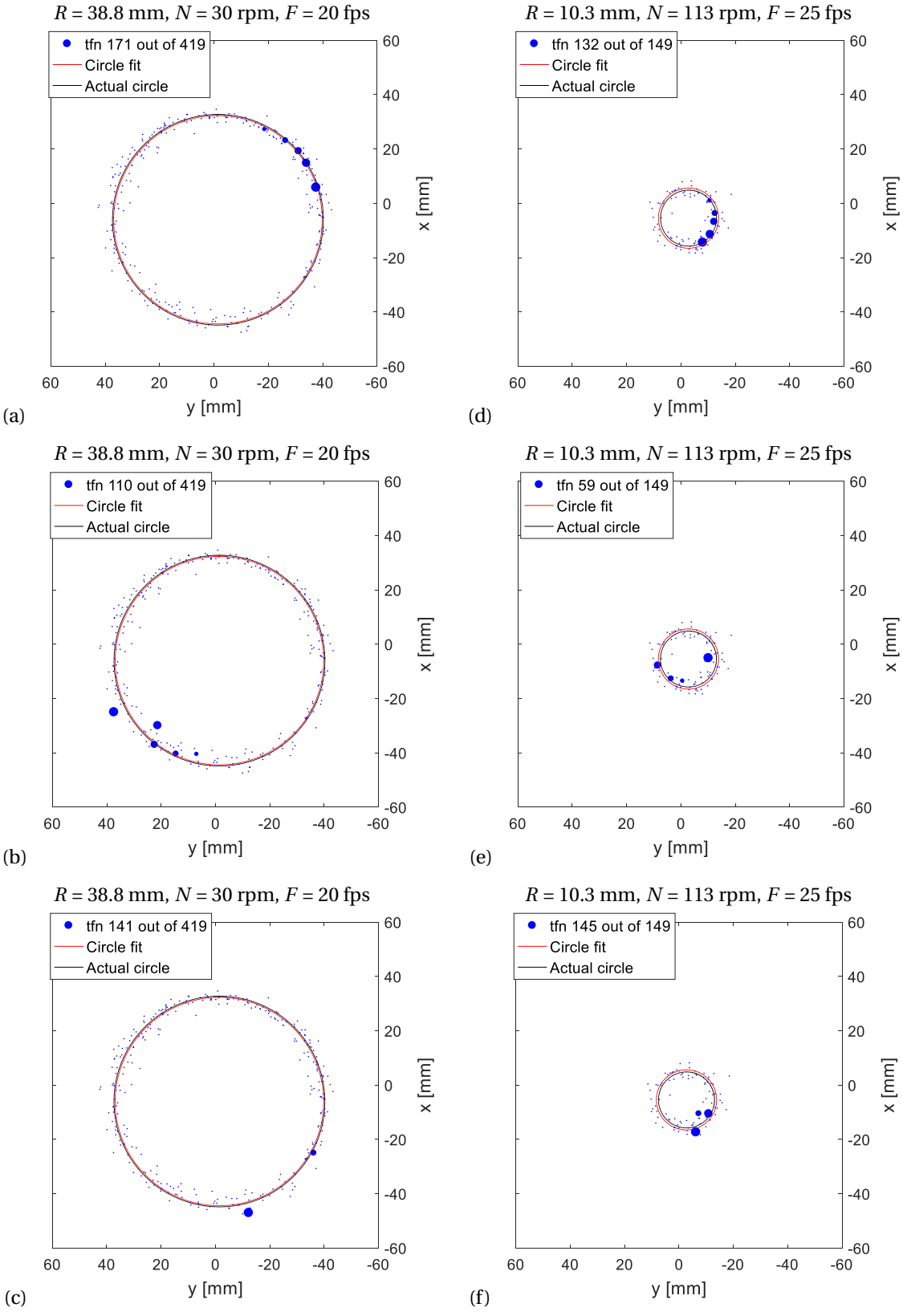

Figure 6.11: The reconstructions of the time frames for a ^{198}Au source of 45 MBq making a circular motion represented by the small blue dots. With in (a) through (c) a radius of 38.8 mm and rotational speed of 30 rpm, using a frame rate of 20 fps and in (d) through (f) respectively 10.3 mm, 113 rpm and 25 fps. Both resulting in a tangential velocity of 122 mm/s. In each plot the reconstructions of the current and the previous four time frames are highlighted. The bigger the dot, the more recent the time frame. In each plot also the fitted and the actual circle are shown, respectively in red and black.

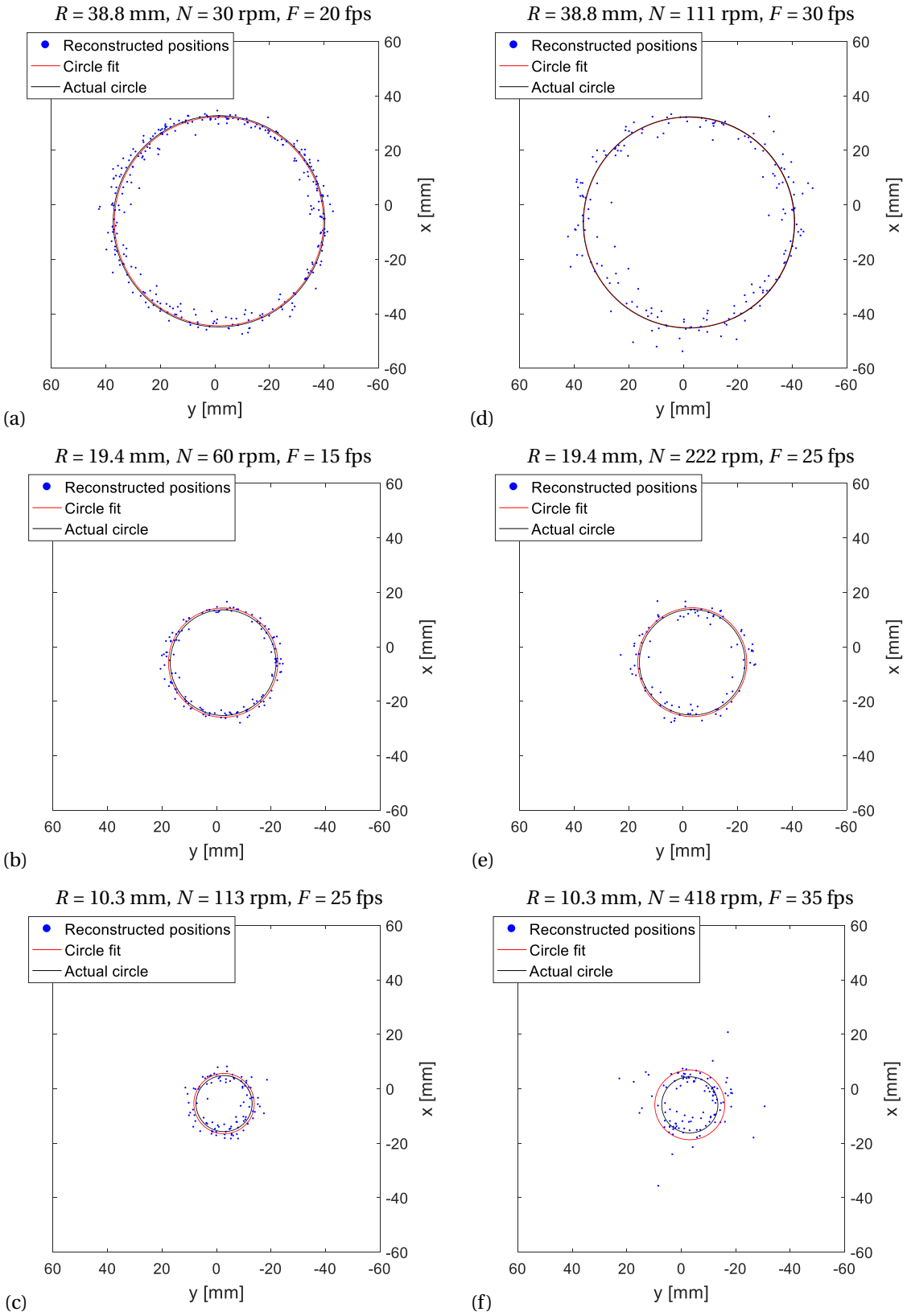

Figure 6.12: Top view of the reconstructions of the time frames for a ^{198}Au source of 45 MBq making a circular motion represented by the small blue dots. In (a) through (c) the tangential velocity is 122 mm/s and in (d) through (f) it is 451 mm/s. In each plot also the fitted and the actual circle are shown, respectively in red and black.

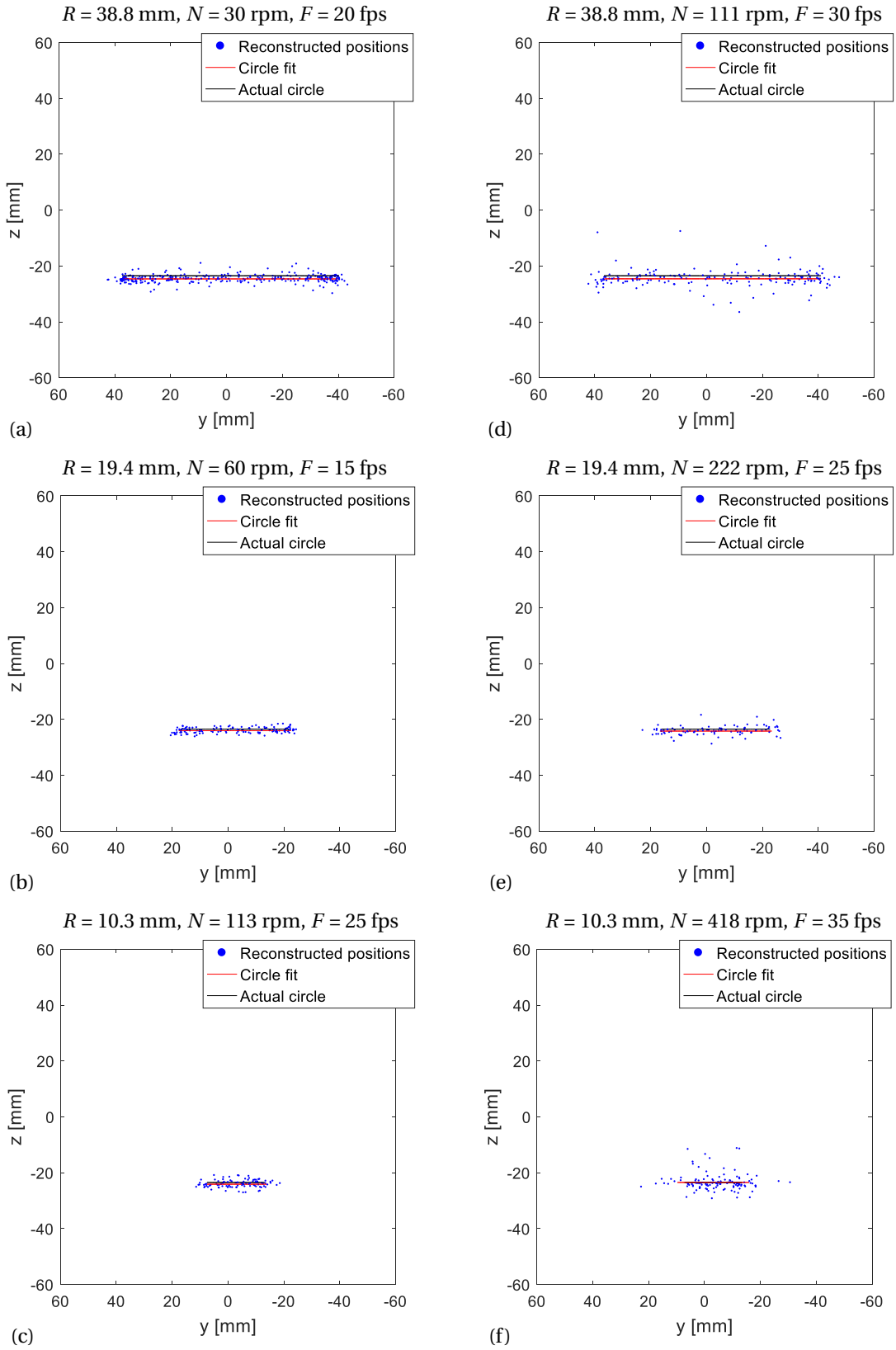

Figure 6.13: Side view of the reconstructions of the time frames for a ^{198}Au source of 45 MBq making a circular motion represented by the small blue dots. In the plots on the left the tangential velocity is 122 mm/s and on the right 451 mm/s. In each plot also the fitted and the actual circle are shown, respectively in red and black.

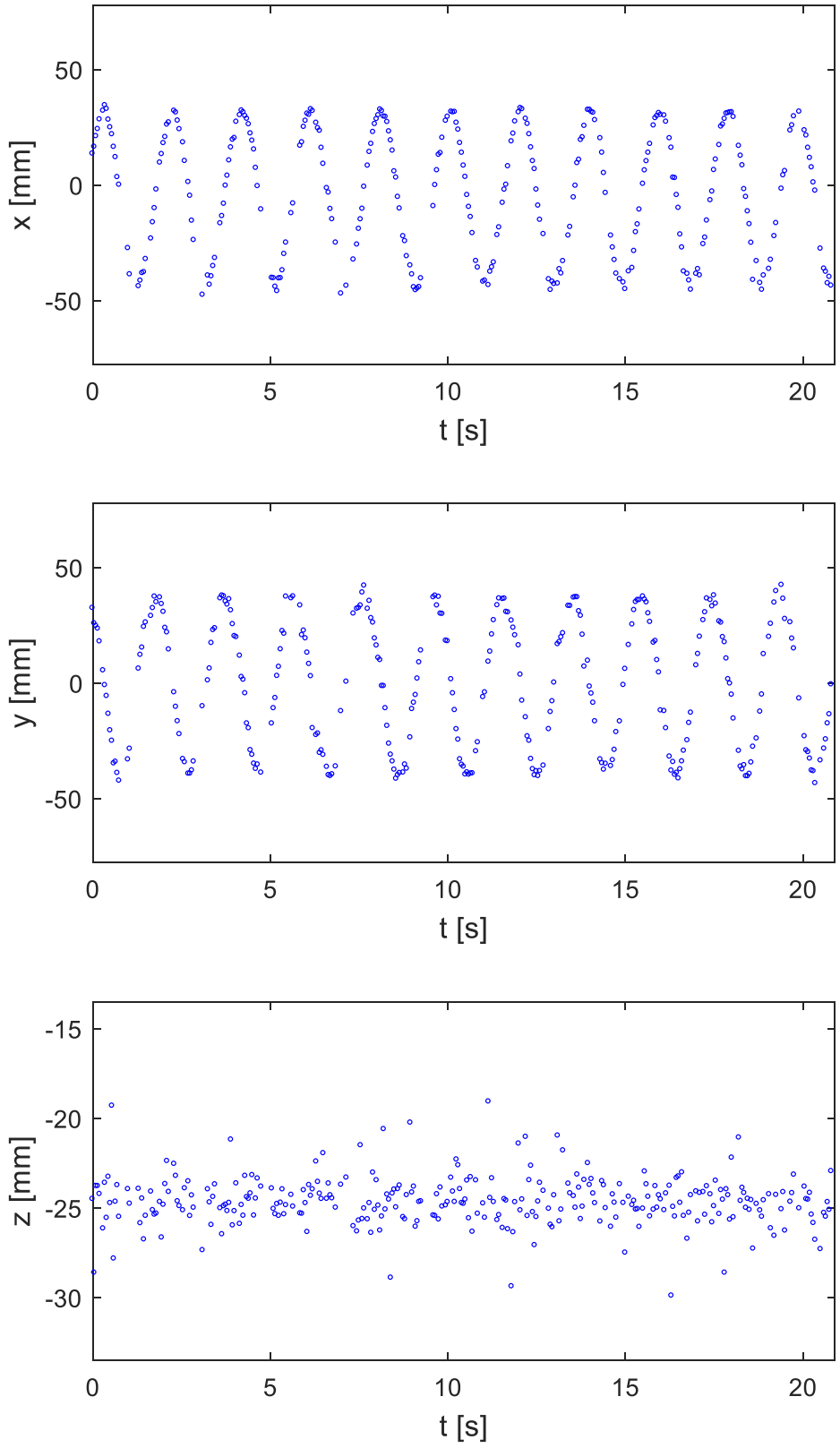

Figure 6.14: Respectively the x, y, and z-coordinates as function of time for the reconstructions of a ^{198}Au source of 45 MBq making a circular motion with a radius of 38.8 mm and rotational speed of 30 rpm, using a frame rate of 20 fps.

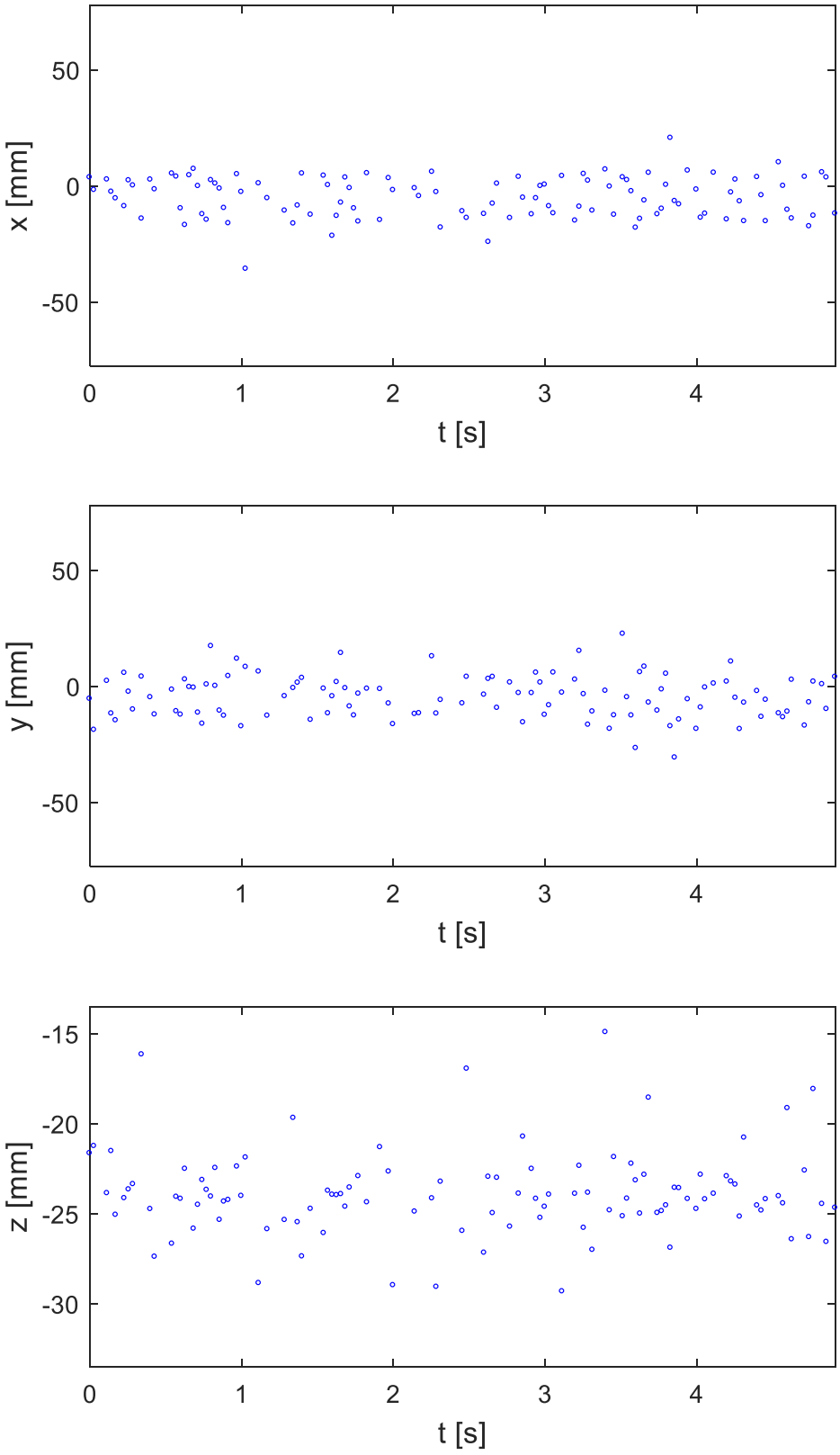

Figure 6.15: Respectively in x, y, and z-coordinates as function of time for the reconstructions of a ^{198}Au source of 45 MBq making a circular motion with a radius of 10.3 mm and rotational speed of 418 rpm, using a frame rate of 35 fps.

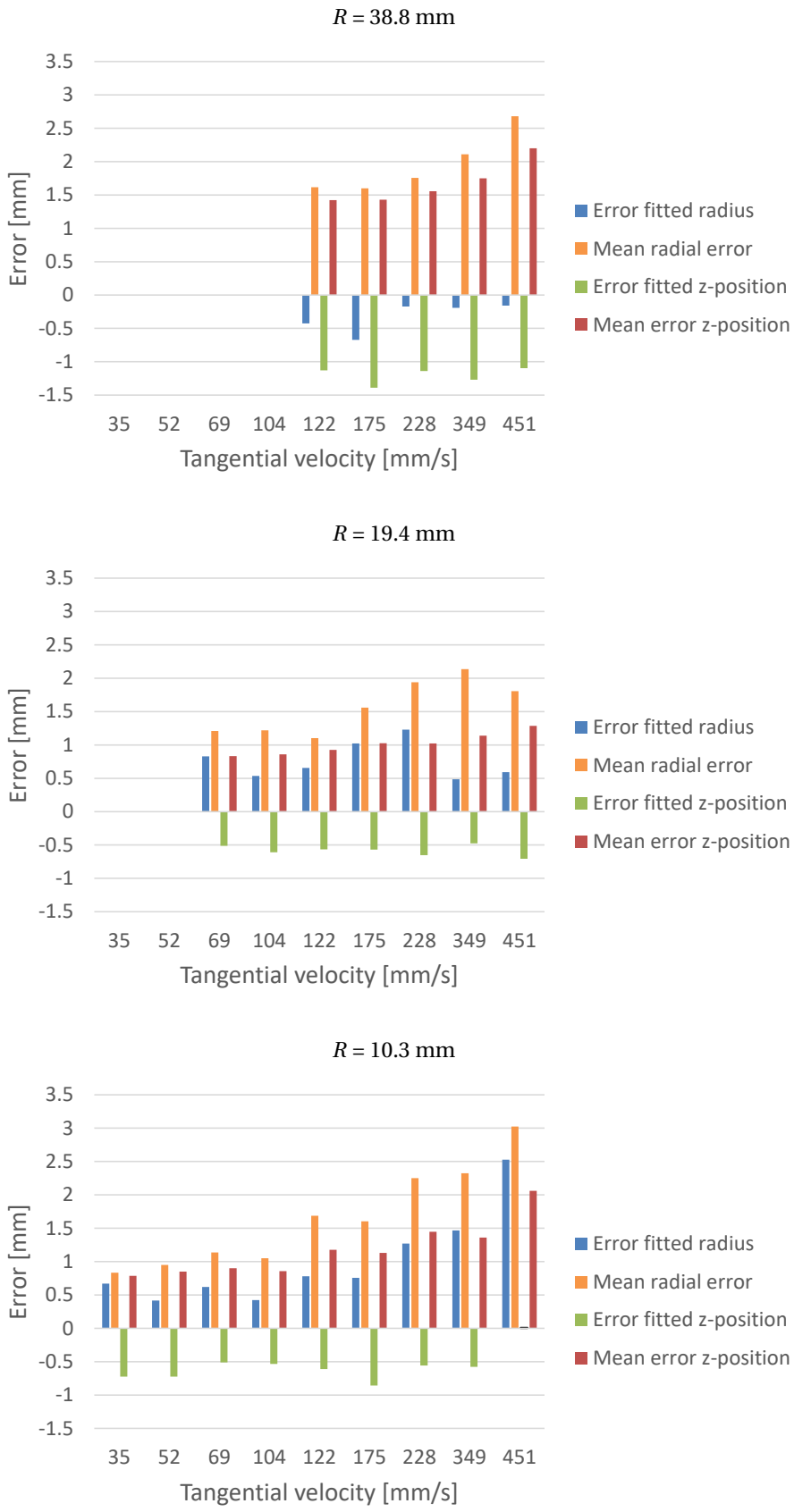

Figure 6.16: The error in the radius of the fitted circle, the mean radial error of the reconstructions, the error in the fitted z-position and the mean error in the z-position of the reconstructions for the different tangential velocities in a chart for each radius. For each radius at each velocity its optimal frame rate is used.

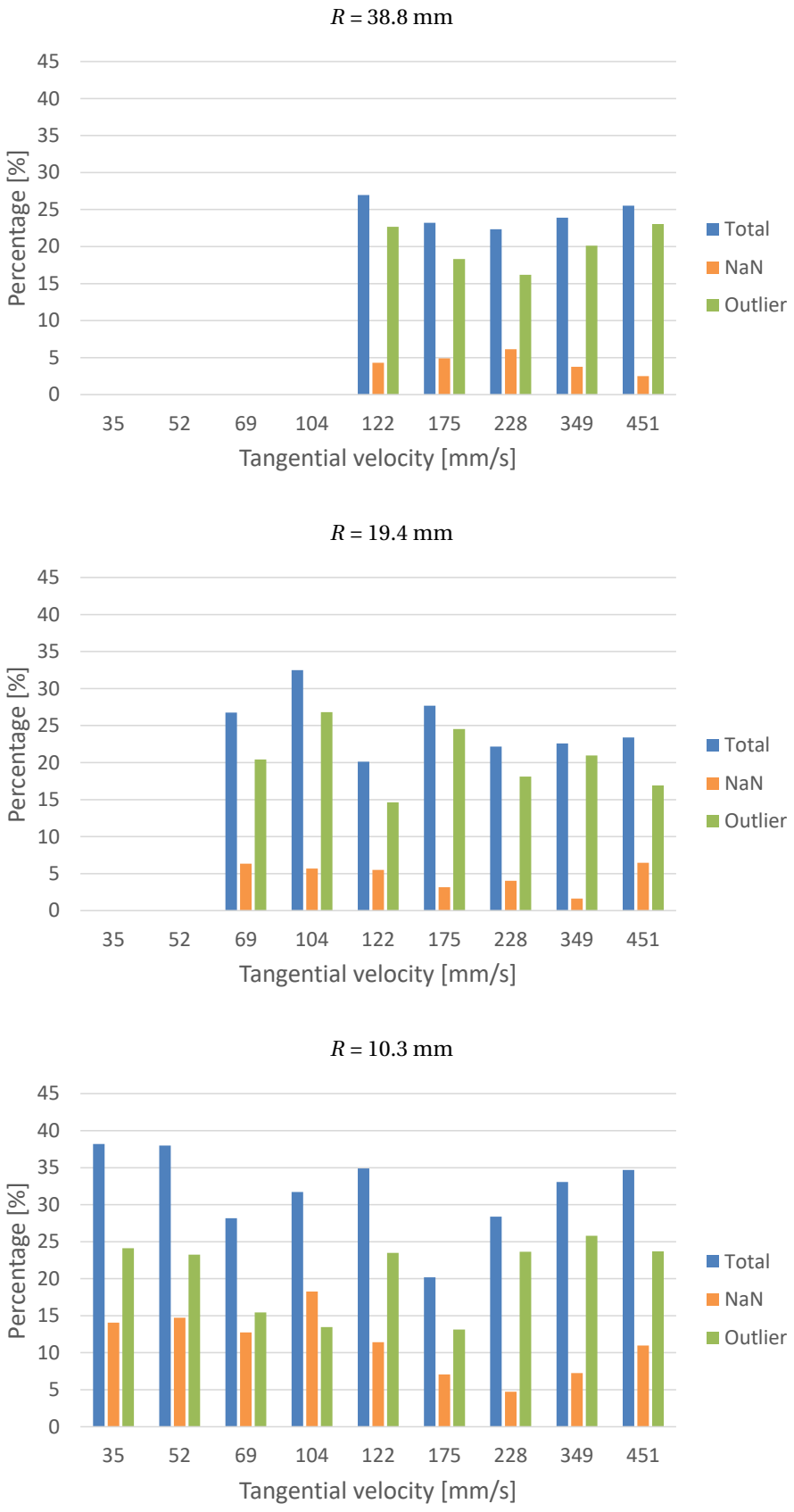

Figure 6.17: The percentage of NaNs, outliers and the total of these two for the different tangential velocities in a chart for each radius. For each radius at each velocity its optimal frame rate is used.

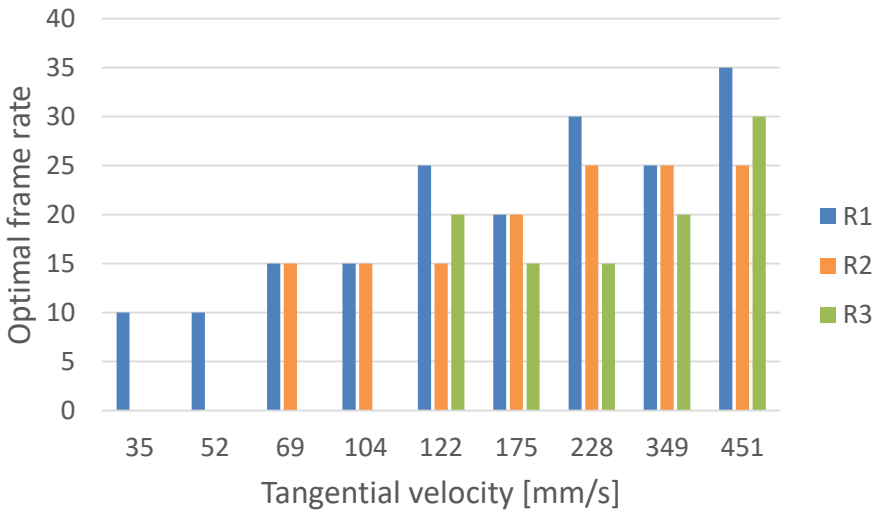

Figure 6.18: The optimal frame rates for the different tangential velocities and for each radius.

6.2.2. Using a fixed frame rate

So now we will be using a frame rate of 20 fps, for all radii at each velocity. In Figure 6.19 the errors of the fit and the mean errors are shown. The error of the fitted radius differs per velocity, but there is no real tendency. While for the two largest radii, the mean radial error again tends to increase for higher velocities. Which we would expect, since when keeping the time frame constant, the motion blur will increase even more for increasing velocities. For the smallest radius, however, it first decreases slightly, then it increases and for the highest three velocities it stays almost constant. The error of the fitted z-position does not change that much per velocity, but it differs per radius. For the medium radius it is smallest and for the largest radius it is biggest. For the largest radius the mean error in the z-position still increases, but for the other two radii it only fluctuates a little.

In Figure 6.20 the percentage of NaNs, outliers and the total of the two are shown. For the medium radius we still see the same behavior. First a small decrease and then an increase in the percentage of NaNs. While for the largest radius it seems to increase and for the smallest one it seems to decrease. The percentage of outliers fluctuates quite a lot again. The same holds for the total of the two, since the percentage of outliers is in all cases larger than the percentage of NaNs. One might notice that the percentage of NaNs for the smallest radius is now smaller for all velocities then before, while the total of NaNs and outliers is almost the same. Except for 175 mm/s, since for this velocity we already used 20 fps. It is strange that both for velocities using now a higher frame rate and for velocities using a lower frame rate, the percentage of NaNs is lower. In the first case, the number of detections decreases, but the effect of motion blur decreases as well. For the second case they both increase. We would think, that one of the effects would be bigger than the other, which would lead to opposite effects, for the velocities lower and higher than 175 mm/s. The decrease in NaNs seems to go together with an almost equal but opposite change in the percentage of outliers, keeping the total of the two the same.

One might notice as well that the errors for the two highest velocities of the smallest radius are smaller than for the optimal time frames and the percentage of NaNs and outliers are similar. We did not select the time frame rate of 20 fps as optimal, because this would mean that the number of reconstructions per revolution became less than five. Since we are trying to reconstruct a circular motion, we decided five reconstructions per revolution is the minimum to be able to recognize a circular motion.

We also tried to reconstruct the velocity of the source. The result is shown in Figure 6.21, where it is shown as function of time. The actual velocity of the source is 122 mm/s. The reconstruction is not very accurate, as one can see. More than 30% is found within an error of 20 mm/s, but most times a higher velocity is found. With as maximum a velocity of nearly four times as high. This can be seen in Figure 6.22 where the probability distribution and the cumulative probability distribution of the reconstructed velocity are shown. Since the reconstructed velocity is not very accurate, there is little use in trying to use it to make a variable frame rate, as was mentioned before. Therefore also in the experiment with the source moving freely we will use a fixed frame rate.

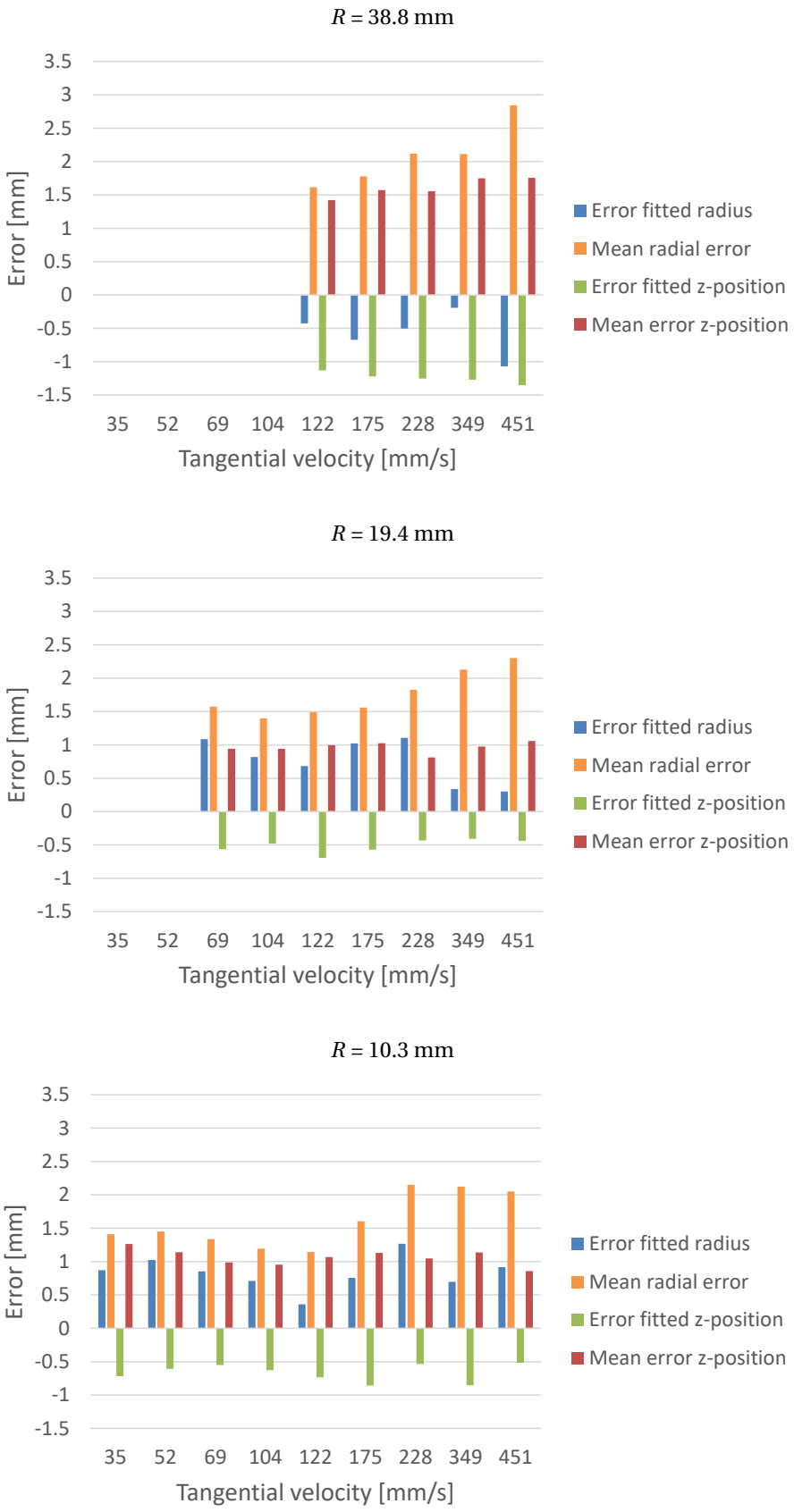

Figure 6.19: The error in the radius of the fitted circle, the mean radial error of the reconstructions, the error in the fitted z-position and the mean error in the z-position of the reconstructions for the different tangential velocities in a chart for each radius. For each velocity a frame rate of 20 fps is used.

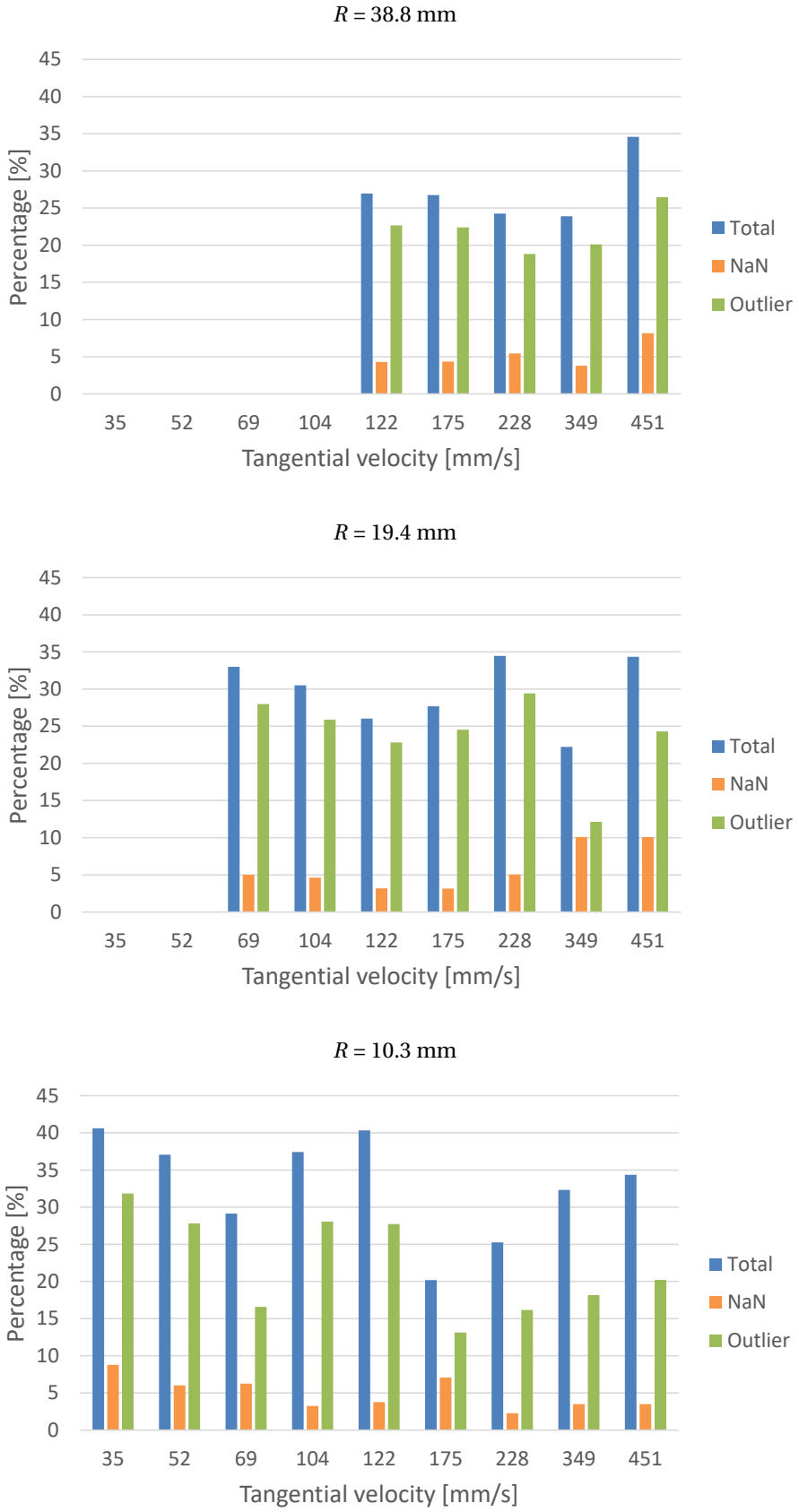

Figure 6.20: The percentage of NaNs, outliers and the total of these two for the different tangential velocities in a chart for each radius. For each velocity a frame rate of 20 fps is used.

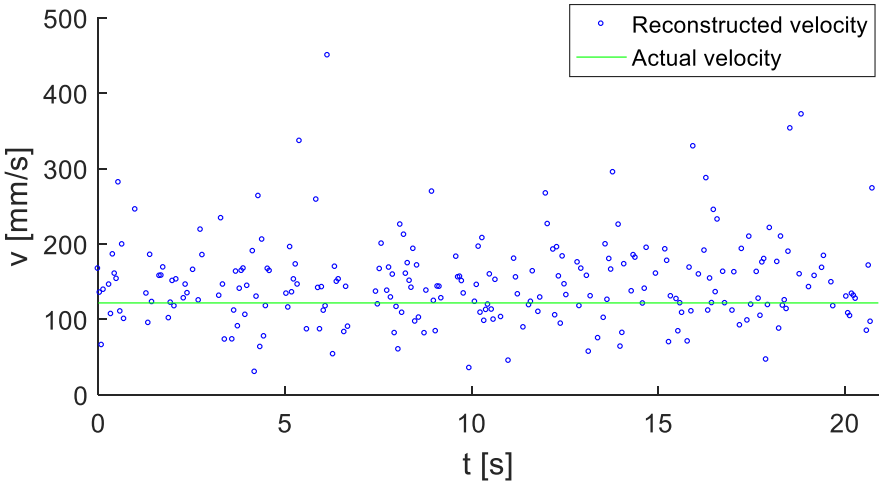

Figure 6.21: The reconstructed velocity as function of time for a ^{198}Au source of 45 MBq making a circular motion with a radius of 38.8 mm and rotational speed of 30 rpm, using a frame rate of 20 fps, plotted together with the actual velocity of 122 mm/s.

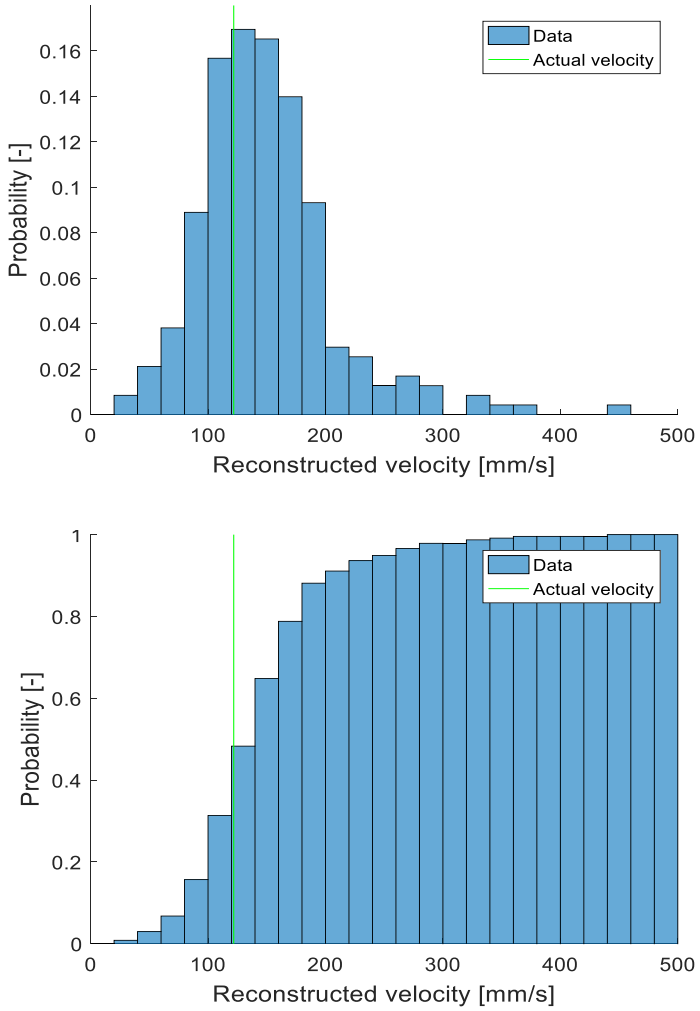

Figure 6.22: Probability distribution of the reconstructed velocity shown in the upper plot and the cumulative probability distribution shown in the lower plot.

6.3. Moving freely in a stirred tank

Now we will consider the ^{198}Au of 69 MBq moving freely in a stirred tank for 60 s for different values of Re. Although the activity of this source is higher than for the experiment with the source moving along a known circular trajectory, we will use the same fixed frame rate of 20 fps as was used there. Since we know less about the motion of the source, we have less information to use to filter out outliers. We used only the maximum displacement between two reconstructions, using the velocity of the tip of the blades of the stirrer and the time frame length. In Figure 6.23 the reconstructions are shown for N = 420 rpm, with in each plot five different time frames highlighted. In Figure 6.23a through c some frames are highlighted which seems to give good reconstructions. A large part of the time, the source circles around at the bottom of the tank (shown in Figure 6.23a). Just like the stirrer, in the clockwise direction. Occasionally the source is lifted up from the bottom (shown in Figure 6.23b), after which it soon will move down to the bottom again. A few times the source gets lifted up and moves to the top of the tank, after which it gradually moves back to the bottom. However, not all reconstructions are as good as these. For instance, often there seems to be a jump back and forth for one time frame, as is shown in Figure 6.23d. These are probably outliers that need additional filters to be deleted. Like filters using the acceleration of the source. But sometimes outliers are deleted or the reconstruction gave NaN, which leads to gaps in the reconstructions, as is shown in Figure 6.23e. But since we do not know how the source is actually moving, we never know for sure whether we are looking at the real motion of the source or some errors of the reconstructions. Especially when the source is moving very slowly. Something else that these reconstructions show is that during the measurement the source got stuck in the zip tie connecting the pipe of the aerator to one of the baffles. After a few seconds it got free by itself. This happened a few times as well for other rotational speeds of the stirrer.

In Figure 6.24 the top and side views are shown for the results of three different rotational speeds and thus different Re, together with the boundaries of the tank. To reconstruct the position of these boundaries we placed the center of the tank at the same (x, y)-position as the center of one of the fitted circles for the source moving along a known circular trajectory. We took the one with the largest radius at its minimal rotational speed using its optimal frame rate, since this fit was one of the most accurate. However, we did not measure whether the rotator was exactly in the middle of the tank. So there might be a slight offset.

For the lowest Re of $7.2 \cdot 10^3$ shown in Figure 6.24a and d, we see that the source stays almost all the time at the bottom and close to the axis of the tank. In the top view we see a small group of reconstructions, slightly away from the bigger group near the axis. This is the position where the source had sunk to after putting it inside the tank before starting the measurement. After some time it starts to move closer to the axis, where it will move around. The larger group seems to be not exactly centered at the axis of the tank. Besides the possible offset of the boundaries, this might as well be caused by the fact that when replacing the rotator by the stirrer, the stirrer was positioned slightly differently. In the side view we see some reconstructions slightly above the bottom. However, most of them seem to be sudden jumps and thus outliers. What one might see as well, is that some of the reconstructions fall outside the boundaries of the tank. We did not filter these out, such that we could see whether it is necessary or not and because the reconstructed boundaries are not that accurate.

For the Re of $1.2 \cdot 10^4$ shown in Figure 6.24b and e, we see slightly more radial and vertical spreading. Meaning that the source starts to move more. This is in line with the N_{js} we found earlier using the Zwietering criterion, since the stirrer speed of 300 rpm is slightly above it. This time most of the higher reconstructions are not just outliers, but actual movements where the source is lifted up from the bottom, subsequently moving radially outward and back to the bottom.

For the Re of $1.7 \cdot 10^4$ shown in Figure 6.24c and f, we see much more radial and vertical spreading. Meaning that the source starts to move even more. One can see in the side view that most of the reconstructions stay below a certain height. This is where the stirrer is. The center of the stirrer is at z = -23.5 mm. Using half the width of the blades we reach z = -28.5 mm, which is the vertical position of the underside of the stirrer. The reconstructions seem to stay slightly lower, probably because they are pushed out radially even before reaching the stirrer. A few times the source reaches the upper region of the tank above the stirrer. Increasing Re further to $1.9 \cdot 10^4$ and $2.2 \cdot 10^4$ does not seem to change much.

So for the lowest Re the tracer particle does not show much of the motion of the water. For Re above $1.4 \cdot 10^4$ the tracer particle is able to show the motions in the lower region of the tank and occasionally of the upper region. So depending on the Re and the region you want to investigate, a better tracer particle is necessary.

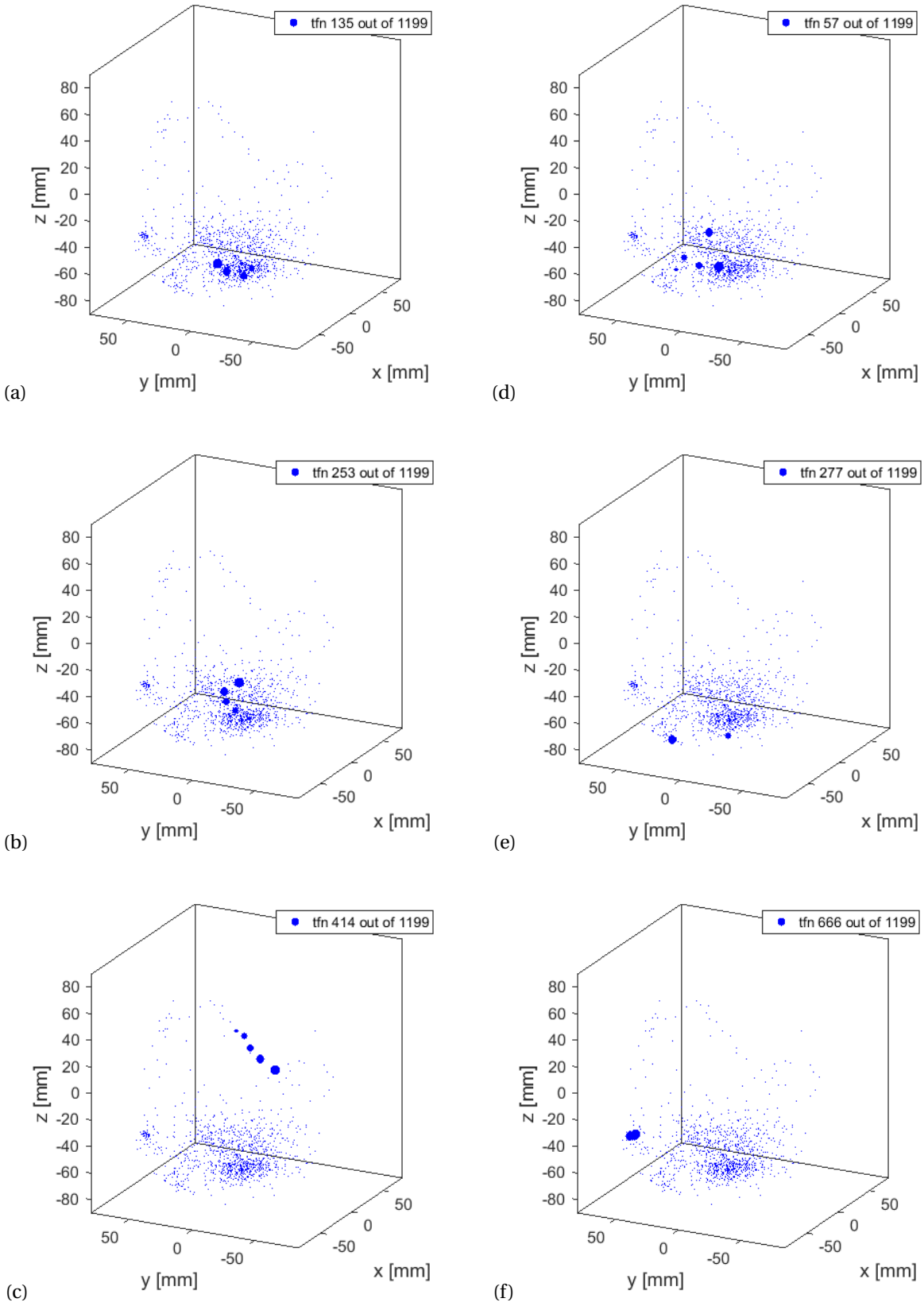

Figure 6.23: The reconstructions of the time frames for a ^{198}Au source of 69 MBq moving freely in a stirred tank for 60 s with N = 420 rpm, corresponding to $Re = 1.7 \cdot 10^4$, and a frame rate of 20 fps, represented by the small blue dots. In each plot the reconstructions of the current and the previous four time frames are highlighted. The bigger the dot, the more recent the time frame.

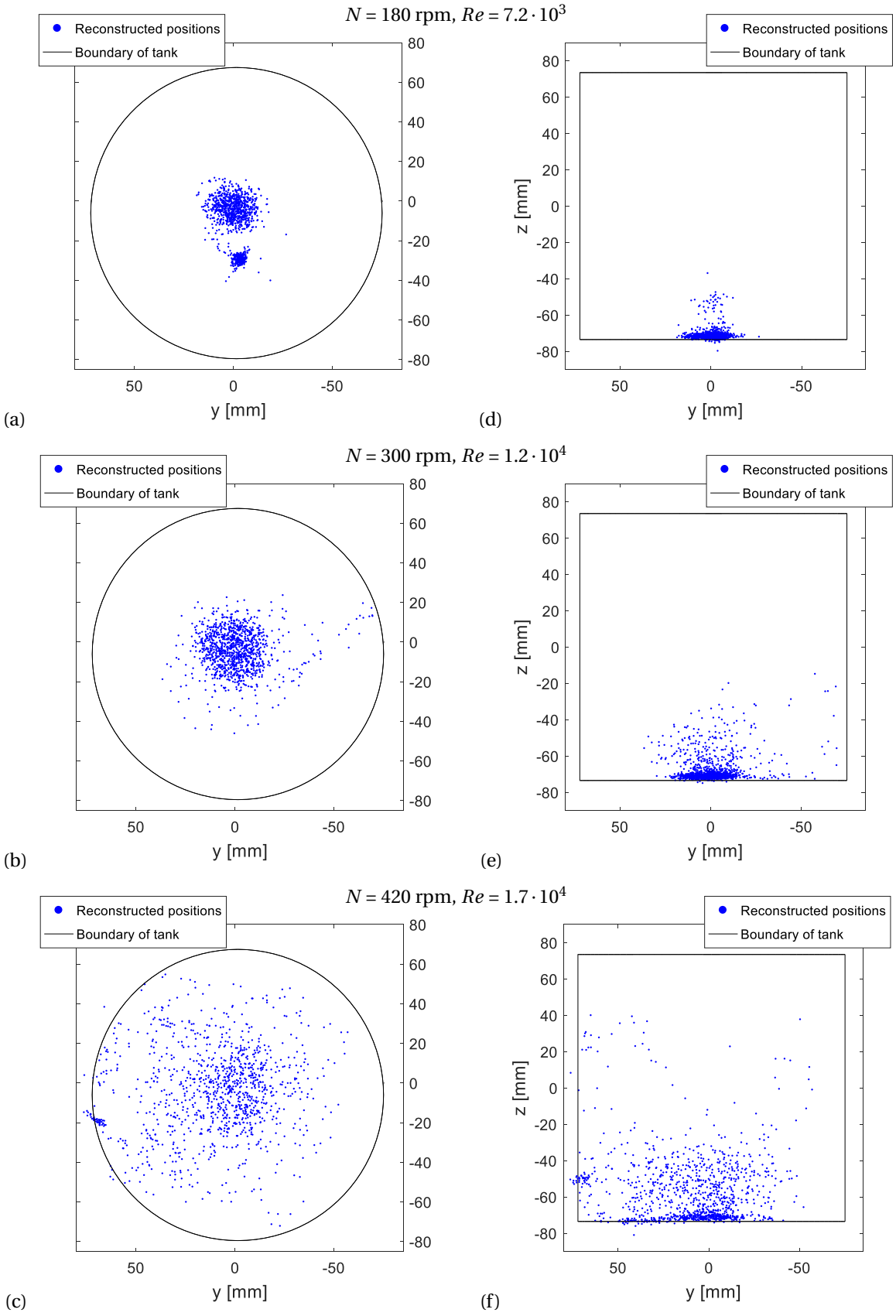

Figure 6.24: The reconstructions of the time frames for a ^{198}Au source of 69 MBq moving freely in a stirred tank for 60 s using a frame rate of 20 fps, represented by the small blue dots. There are plots for three different rotational speeds with in (a) through (c) the top views and in (d) through (f) the side view. Also the boundary of the tanks are plotted in black.

6.4. The effect of bubbles

In this section the results are shown for the experiments where we injected bubbles at the bottom of the tank. First we will discuss the results for moving along a known circular trajectory with bubbles.

6.4.1. Moving along a known circular trajectory with bubbles

In Figure 6.25 we have again the errors of the fit and the mean errors, but now for different air flow rates. There is a chart for each radius at the tangential velocity of 122 mm/s using its optimal frame rate. For all radii almost everything stays more or less constant. There are a few exceptions. Such as the maximum air flow rate for the largest radius, there the fitted z-position suddenly increases, which decreases the error. However, the mean error of the z-position suddenly increases. This is probably caused by some outliers which were not deleted by the filters. For the smallest radius the error in the fitted radius increases for increasing air flow rates, as does the mean radial error.

For more information about the cause of this we also looked at the detection rate of each detector, the number of hits per second, and how this changed with the air flow rate. For the largest radius most changes are below 0.5%. Most of them showing an increase. Only three are bigger but still only around 1%. For the medium radius, four of the changes are above 0.5% but none of them above 1%. For the smallest radius almost all changes show an increase. But there are no real trends visible for the different flow rates. That for the smallest radius more often an increase in the detection rate is found, might be caused by the following. The bubbles are released in a circle with a radius of 15 mm. The bubbles rise in a column to the rotator, with the radius not changing that much. So probably with the source at the smallest radius, is the only case where the source is surrounded by bubbles. In the other two cases the source is outside the bubble column, so there is always a detector for which there are no bubbles in between. When making multiple rotations, the average number of bubbles between the source and each detector, will be lower than with the source inside the bubble column.

One might think that the gamma radiation might get refracted by the bubbles, just as visible light does, when it travels from one medium to another. But the refractive index of gamma rays in both air and water is almost equal to one. So the bubbles will not lead to the deflection of photons from their path to the detectors, resulting in less detections. There is another phenomena that could affect the accuracy of the reconstructions when introducing bubbles to the system. Namely the fact that air has a higher transmittance for gamma rays than water. So when there are bubbles on the path from the source to the detectors, more photons will reach the detectors. And thus, the accuracy would even increase by adding bubbles to the system. However, we see in the results that the differences are so small, there does not seem to be a real effect. For these air flow rate though. For higher air flow rates, the effect might become larger.

6.4.2. Moving freely in an aerated, stirred tank

In Figure 6.27 the reconstructions are shown for the ^{198}Au of 69 MBq moving freely in a stirred tank for 60 s for $Re = 1.7 \cdot 10^4$ and for different air flow rates. In Figure 6.27a and g the results from before without air are shown. But already at the lowest air flow rate of 2 L/min we see a huge difference in the radial and vertical spreading of the reconstructions. Meaning that the movement of the source has become much less, as if the Re is decreased. This is caused by the presence of the bubbles, which show a loading pattern. The bubble column, rising to the stirrer, decreases the average density in that region. Leading to a decreased buoyancy force and resulting in the tracer particle being to heavy to be dragged along by the water. When increasing the air flow rate, the spreading of the reconstructions and thus the movement becomes less and less. For 4 L/min the source does reach the upper region one time, but this is probably just a matter of chance. For 6 L/min and higher, most of the reconstructions slightly above the bottom, are again outliers, meaning that the source is almost all the time at the bottom of the tank. This is in line with the N_{jsg} we found earlier using the Zwietering criterion, since a stirrer speed of 420 rpm is approximately the N_{jsg} for 6 L/min. However, for 10 L/min the source does again reach the upper region once. But besides that the source almost does not move. Increasing the flow rate causes also the flow pattern to make a transition to flooding. This seems to have little effect on the motion of the source, however.

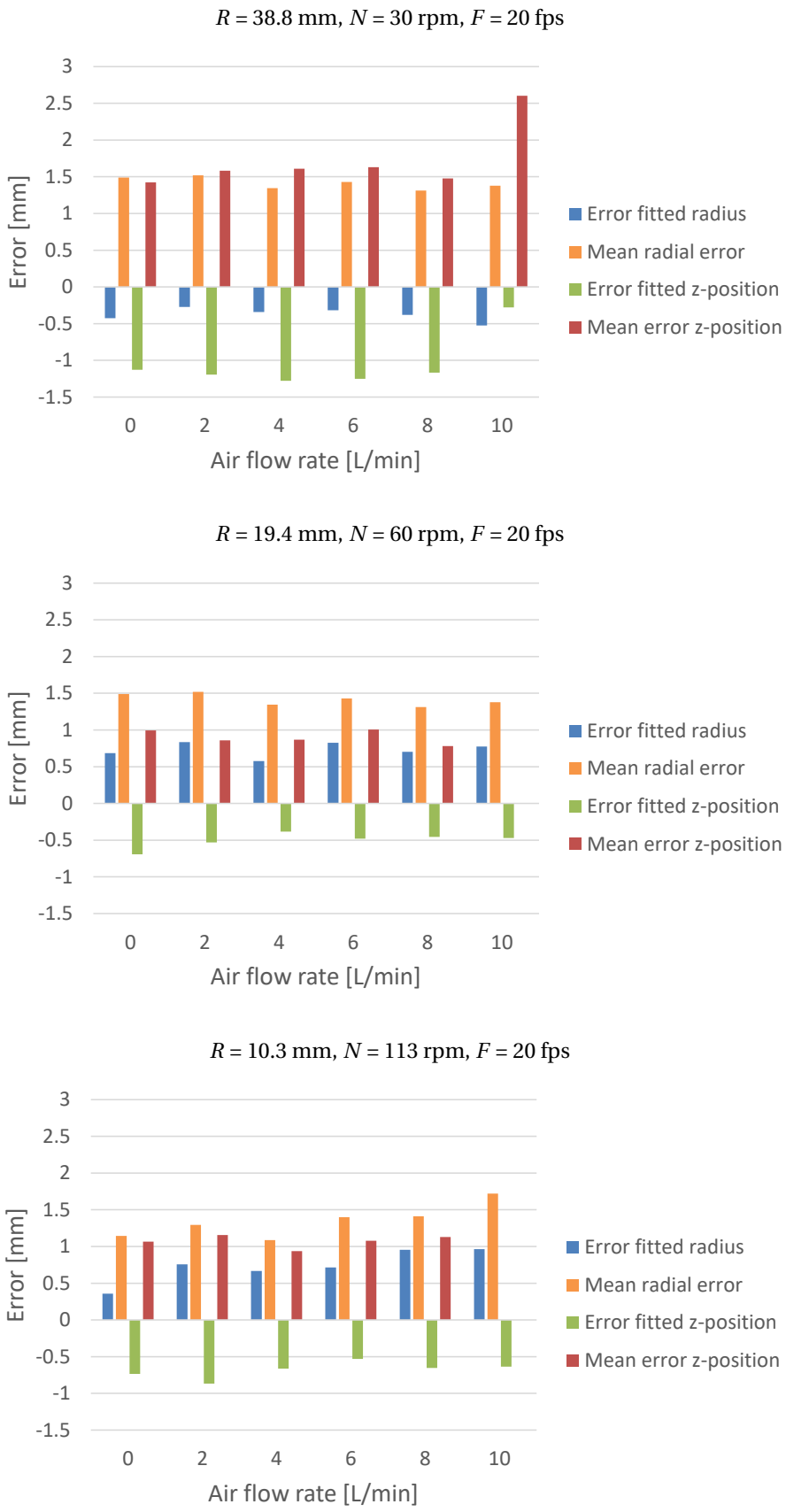

Figure 6.25: The error in the radius of the fitted circle, the mean radial error of the reconstructions, the error in the fitted z-position and the mean error in the z-position of the reconstructions for different air flow rates. With a chart for each radius, but all at a tangential velocity of 122 mm/s and using a frame rate of 20 fps.

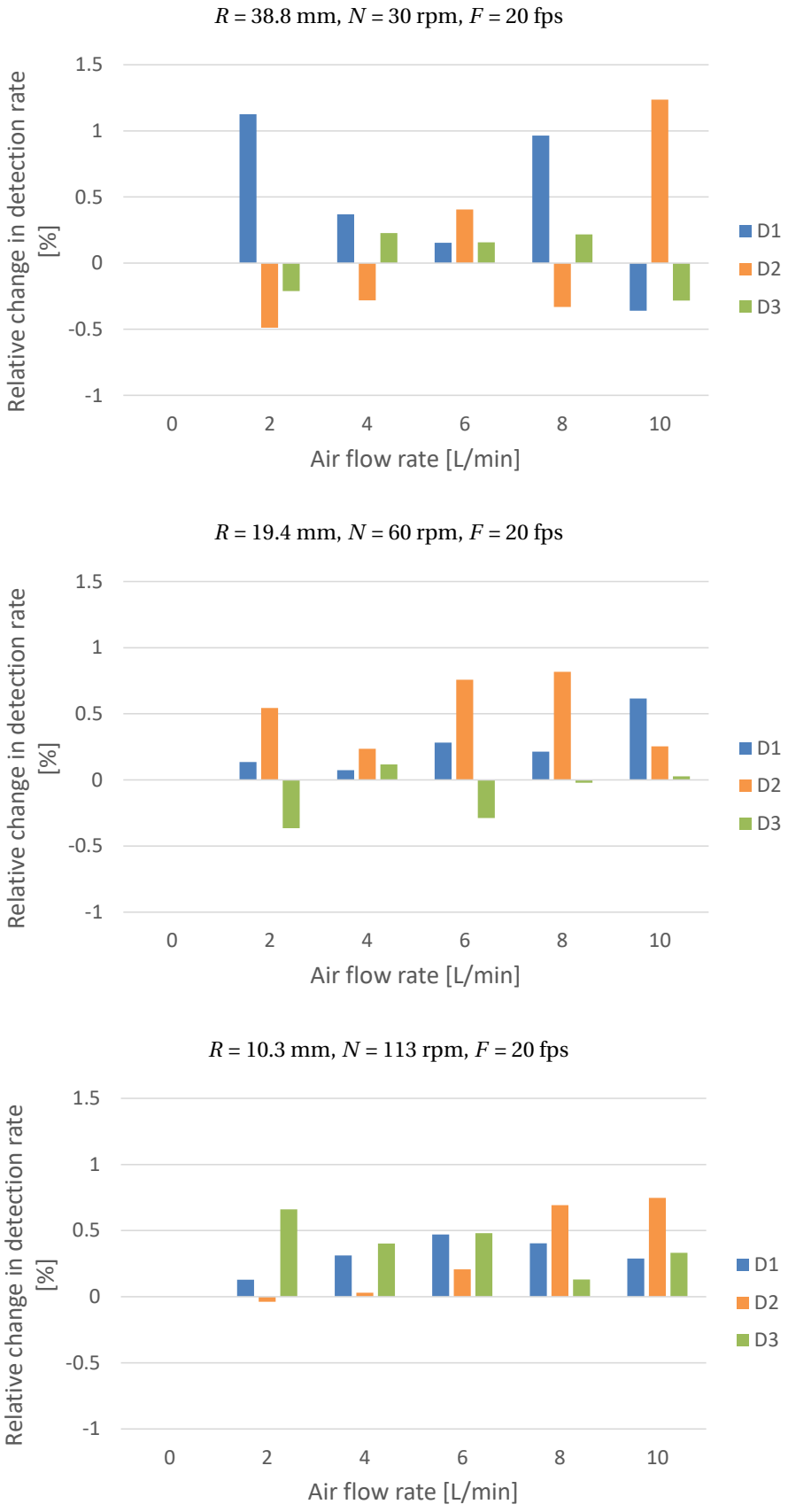

Figure 6.26: The relative change in the detection rate for different air flow rates compared to the case without bubbles. With a chart for each radius, but all at a tangential velocity of 122 mm/s and using a frame rate of 20 fps.

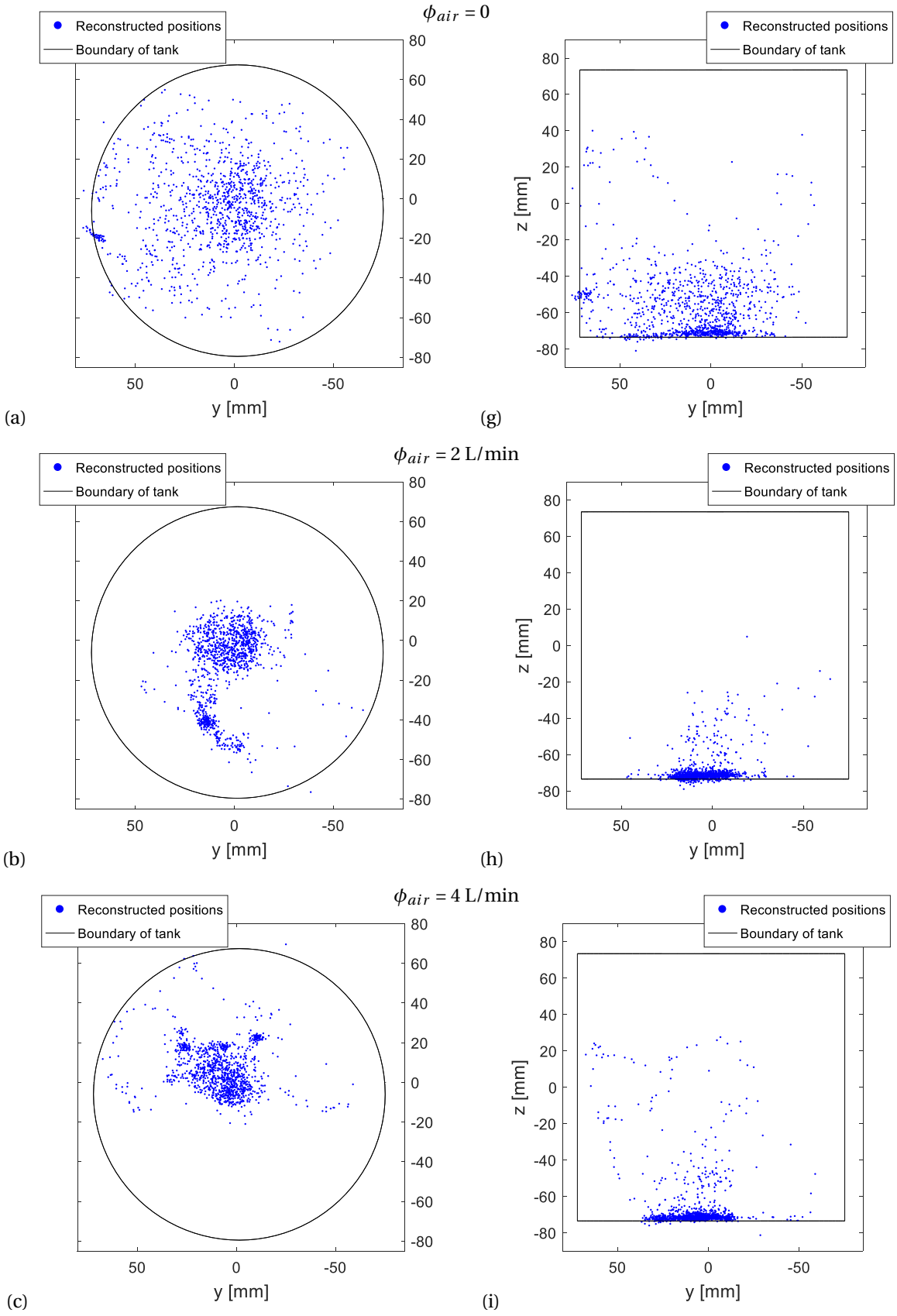

Continues on next page

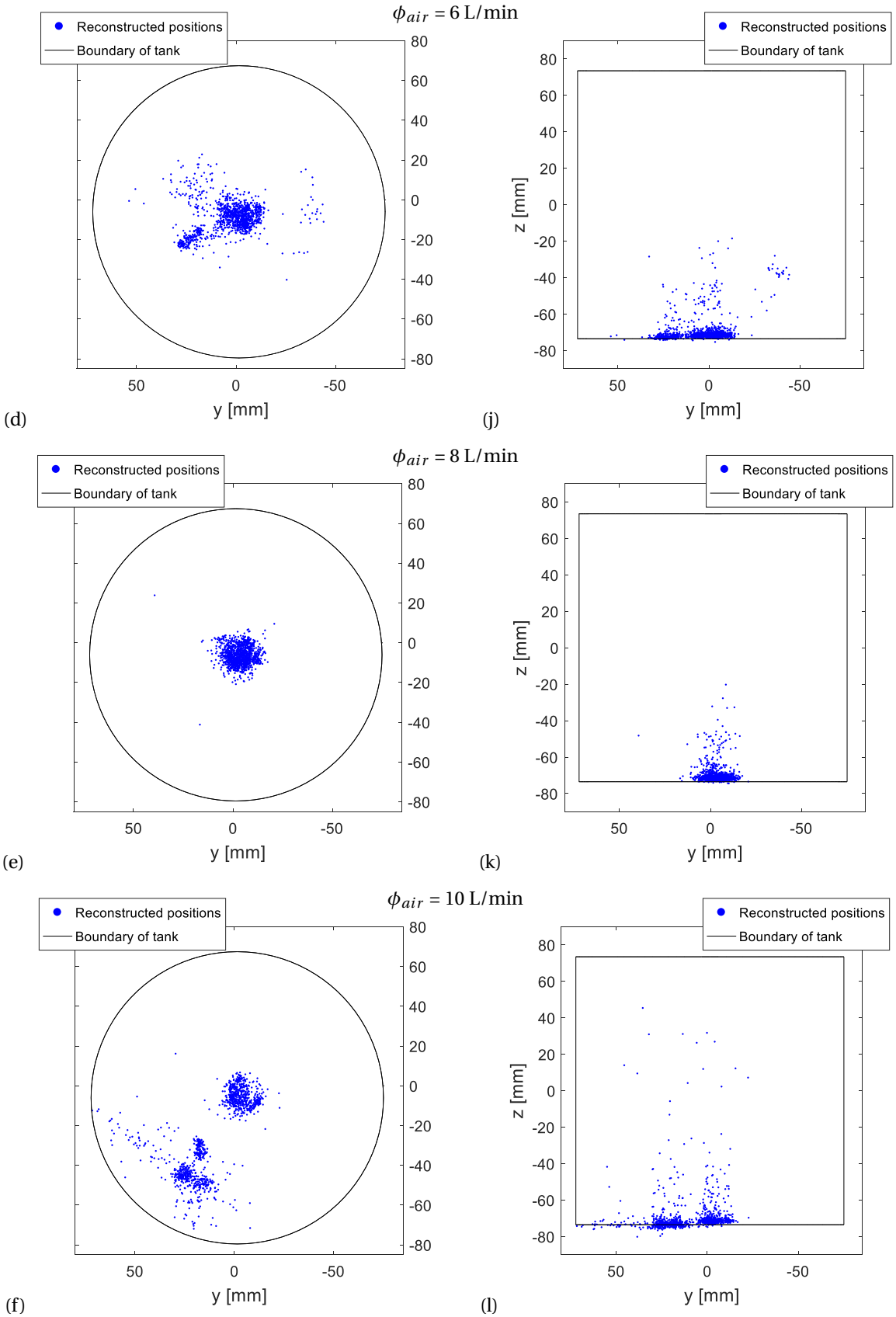

Figure 6.27: The reconstructions of the time frames for a ^{198}Au source of 69 MBq moving freely in a stirred tank with $N = 420$ rpm and $Re = 1.7 \cdot 10^4$ for 60 s using a frame rate of 20 fps, represented by the small blue dots. There are plots for six different air flow rates, ϕ_{air}, with in (a) through (c) the top views and in (d) through (f) the side view. Also the boundary of the tanks are plotted in black.

7

Conclusion and recommendations

7.1. Conclusion

First we looked at a fixed source placed at different positions in air. For the ^{198}Au source of 69 MBq we saw, when using the complete measuring time, a general tendency for the error to increase when the source is horizontally displaced from the origin. The mean errors, taken over the different z'-positions, range from 0.5 up to 4 mm. This is is probably caused by two things, the decrease in the number of detections of one of the detectors and the effect of the inaccuracies in measuring the geometry of the setup increasing farther away from the origin. The error does not seem to depend on the z'-position. The mean error per z'-position ranges from 1 up to 1.5 mm. Overall, 45% of the reconstructions are within an error of 1 mm and 68% within 1.5 mm. For the ^{57}Co of 3.2 MBq we saw this can be increased to respectively 75% and 86% even though less detections are used. This difference is caused by the higher energy of the gamma photons of the ^{198}Au source, causing more photons to travel right through the collimator, resulting in a lot of unwanted detections.

We also looked at how the frame rate influences the error of the reconstructions of the fixed positions compared to the reconstructions using the complete measuring time. Therefore we calculated the mean error and the 95% error over all positions and all time frames for different frame rates. For both we see a linear increase. With the mean error ranging from 0.7 up to 1.7 mm for frame rates of 5 up to 50 fps and the 95% error ranging from 1.2 up to 3.3 mm for the same frame rates. The percentage of NaNs stays almost zero, due to the high detections rate. This is a big difference with what we saw for the ^{57}Co source, where the percentage of NaNs increases rapidly after a frame rate of 25 fps, due to the little number of detections per time frame. The percentage of outliers stays below 11% in all cases. With only 4% at its minimum at a frame rate of 20 fps.

To obtain knowledge about how the error depends on the velocity of the source, we reconstructed the motion of the ^{198}Au source of 45 MBq moving along a known circular trajectory in water. This was done for three different radii. First we used for each radius at each velocity its optimal frame rate. As we would expect, there is a general trend for higher optimal frame rates for higher velocities. The error of the fitted radius does not show a clear tendency, except for the smallest radius where it increases for higher velocities. Most of these errors are about 1 mm or lower. Also the mean radial error and mean error in the z-position increase for higher velocities, as we would expect, since higher frame rates cause less detections per time frame and higher velocities cause more motion blur, even with these optimal frame rates which increase with the velocity. Both effects result in a larger spreading in the reconstructions. Both mean errors are very similar for the different radii and range from 0.8 up to 3 mm. The percentage of NaNs and outliers fluctuate per velocity, but do not show a clear trend. Respectively about 5% and 20% of the reconstructions result in NaN or an outlier for the two largest radii. For the smallest it is about 10% and 20%. Subsequently we used a fixed frame rate of 20 fps for each radius at each velocity since that would also be the case with the source moving freely. The biggest change is that the mean error in the z-position no longer seems to depend on the velocity. Neither does the error of the fitted radius for the smallest radius anymore.

When we tried to reconstruct the velocity of the source moving at the largest radius with a velocity of 122 mm/s only 30% of the reconstructions are found within an error of 20 mm/s. Most reconstructions are to be found with higher velocities.

With the source moving freely in the stirred tank, we saw that increasing Re, the tracer particle starts to move more, but probably following the flow less accurately, since St increases. However it is sometimes

challenging to distinguish errors in the reconstruction from the actual movement.

At last we added bubbles for both experiments with a moving source in water. With the source moving along a known circular trajectory, we saw no significant changes when increasing the air flow rate up to 10 L/min. For the source moving freely, we were not able to verify whether the accuracy of the reconstructions had changed, but we did see a difference in the behavior of the tracer particle. It moved less and less for higher air flow rates, which results in spending more time at the bottom of the tank. This is due to the decrease in the average density that the bubble column is causing, making the tracer particle to heavy to follow the flow.

To conclude, the accuracy that can be achieved when applying Radioactive Particle Tracking using SPECT in a Stirred Tank filled with water, depends on the position of the tracer particle, the frame rate that is used and the velocity of the tracer particle. It is a nice technique to locate the tracer particle at different instances in time in a stirred tank, since it is non-invasive. But due to the inaccuracies in the reconstruction there are a lot of outliers, of which a large part can be filtered out, but which will leave gaps in the reconstructed path. Nevertheless, at some instances in time the position of the source will be known quite accurately. But both the inaccuracies and the gaps make this technique unsuited to reconstruct the velocity of the tracer particle and thus investigate the velocity of the fluid flow. However, there are still a lot of possibilities for improvement. Some of these are discussed in the next section.

7.2. Recommendations

Something that is not addressed that much before, but is very important to be aware of when one wants to perform experiments like done for this research, is the dose one receives from the radioactive source. It is almost unavoidable to receive some dose from it. In total we received an equivalent dose of 10 μSv. On a yearly basis one receives 2.5 mSv in the Netherlands, so the extra those is one and a half times what one receives per day. This is not significant, but one should always be careful and try to avoid as much dose as possible. Each experiment should be prepared very well. One should try to do as much as possible already without the source present and think of each step that has to happen and how it can be carried out best. When handling the source, one should use tongs and tweezers to keep a certain distance between the source and ones hands. Ideally, all actions with the source are done automatically. During the experiments, one should take as much distance from the source as possible. At last one should try to estimate in advance of the experiments the dose one will receive and repeat the calculation afterwards.

The are several ways the accuracy of the reconstructions can be improved. One of them is by reducing the detection of photons which passed right through the collimator. This will make the image of the cross more clear and determining of the center position easier and more accurate. This can be achieved by using a better collimator. One which will absorb more of the gamma photons emitted by the ^{198}Au source, leading to less additional detections. This can be done by using a more absorbing material, so with a higher linear attenuation coefficient. But since lead is already a quit good absorber, it is easier to use thicker lead plates. To obtain the same transmittance as the 2 mm lead has for the photons of the ^{57}Co source, the collimator should consist of 30 mm lead. Notice that this is slightly thicker than the lead blocks that together with the collimator fill up the opening in the front of the casing of the detectors. Another way to reduce the number of additional detections, is by using a radioisotope emitting gamma photons with a lower energy. A large fraction of these photons will be absorbed by the collimator, just like with those of the ^{57}Co source. A nice aspect of ^{198}Au is that it can be put as natural gold inside the tracer particle, activated whenever it is needed and used immediately afterwards. But maybe there is a radioisotope emitting gamma photons with a lower energy for which this is possible as well.

Another way to improve the accuracy, is by improving the way that the geometry of the setup is determined. Using a tape measure gives rise to quite big inaccuracies, resulting in errors in the reconstruction. As we saw with the source at multiple fixed positions, there can be partly compensated for this by using the offset of one of the reconstructions and by subtracting this from all further reconstructions. A better way to determine all variables needed to fully describe the geometry of the setup, would be to do a calibration using the measurements of multiple fixed positions and a least squares method. But due to the high number of variables this is a quite difficult task.

For future experiments with the source moving freely in a stirred tank a better flow follower should be used. Since in our experiments, especially the ones with bubbles, the source was most of the time moving around at the bottom of the tank. The best way to improve the tracer particle is by making its average density lower, by decreasing its mass, but keeping its size the same. The tracer particles we used, consist approximately of 4.2 mg of polystyrene and 2 mg of gold. So one way to achieve a lower density is by using less polystyrene, by

making the sphere more hollow. A disadvantage might be that the golden core will be able to move inside the sphere, making its position inside the sphere less accurately known. But maybe this can be solved. Another way is by reducing the amount of gold that is used. This will require a longer activation time to reach the same activity, but this will not cause any problems. It is important to know accurately the amount of gold that is used. We assumed that each tracer particle would contain 2 mg of gold, but each time the activity came out lower than we had aimed for. Namely, 69 and 45 MBq instead of 100 MBq.

In both experiments where the source was moving, we did not know where it actually was located. While this is needed to determine the accuracy of the reconstructions. This reduced the amount of information we could deduce from our measured data. For the case with the source moving along a known circular trajectory, this will be easier to achieve. Therefore we have to find a device for which besides setting its rotational speed, also its starting position and time can be set. Or one that even registers all locations where it has been. For the case with the source moving freely in a stirred tank, one might use multiple CCD cameras to record the movement from different angles, to reconstruct the movement as well, to compare the reconstructions using RPT with. This can only be done for the case without bubbles. Since with the addition of bubbles, the CCD cameras will not always be able to track the tracer particle, especially for high air flow rates.

At last one would probably want to follow multiple particles at ones. This is still quite challenging. The difficult part is when there are multiple sources, each detector will record multiple images of the cross. One needs to know of each cross to which particle it corresponds, and thus with which other two crosses it should be combined to reconstruct the position. Especially after two particles have passed each other very closely, one might loose the knowledge which cross corresponds to which particle. Already for two particles there are eight possible combinations of the six crosses. Some will eventually lead to reconstructions located outside the domain of the tank. But some might not. Distinction can be made by using sources with different activities, making the number of detections per cross different. However, the number of detections per particle already change a bit due to the varying distance from the detectors. This should be taken into account when choosing the activity difference. Maybe an better solution is using different radioisotopes emitting gamma photons with different energies. This way energy discrimination can be used to determine which cross corresponds to which particle. This however restricts one to only use the photopeaks in the energy distributions, where we also used lower energies, since these also contained information about the image of the cross.

When these changes have been implemented the accuracy might improve enough for the technique of Radioactive Particle Tracking using SPECT to become suited to reconstruct the velocity of the tracer particle and thus investigate the flow velocity in a stirred tank.

Appendices

A

Transmittance

Table A.1: Half Value Layers ($HVLs$) for the energies of the ^{57}Co and ^{198}Au source, respectively 122 keV and 412 keV, and for several materials. The values are obtained via interpolation

Material	Energy (keV)	HVL (mm)	Typical th (mm)	Transmittance (%)
Lead	122	0.181	2	0.0473
			25	$2.75 \cdot 10^{-40}$
	412	2.76	2	60.5
			25	0.188
NaI	122	1.91	10	2.63
	412	17.0		66.5
Pyrex	122	20.5	3	90.3
	412	33.0		93.9
Perspex	122	38.0	30	57.8
	412	57.7		69.7
Water	122	43.3	30	61.8
			75	30.1
	412	66.3	30	73.1
			75	45.6
Air	122	$3.97 \cdot 10^{4}$	660	98.9
	412	$6.10 \cdot 10^{4}$		99.3

B

Traversing sequences

Table B.1: Sequence of positions used for the traversing machine in the experiment with a ^{57}Co source at fixed positions in air.

#	x' (mm)	y' (mm)	z' (mm)	t (s)	#	x' (mm)	y' (mm)	z' (mm)	t (s)
1	-50	0	-50	3	50	0	-50	0	3
2	-20	0	-50	3	51	0	-20	0	3
3	-10	0	-50	3	52	0	-10	0	3
4	0	0	-50	3	53	0	0	0	3
5	10	0	-50	3	54	0	10	0	3
6	20	0	-50	3	55	0	20	0	3
7	50	0	-50	3	56	0	50	0	3
8	0	-50	-50	3	57	-50	0	10	3
9	0	-20	-50	3	58	-20	0	10	3
10	0	-10	-50	3	59	-10	0	10	3
11	0	0	-50	3	60	0	0	10	3
12	0	10	-50	3	61	10	0	10	3
13	0	20	-50	3	62	20	0	10	3
14	0	50	-50	3	63	50	0	10	3
15	-50	0	-20	3	64	0	-50	10	3
16	-20	0	-20	3	65	0	-20	10	3
17	-10	0	-20	3	66	0	-10	10	3
18	0	0	-20	3	67	0	0	10	3
19	10	0	-20	3	68	0	10	10	3
20	20	0	-20	3	69	0	20	10	3
21	50	0	-20	3	70	0	50	10	3
22	0	-50	-20	3	71	-50	0	20	3
23	0	-20	-20	3	72	-20	0	20	3
24	0	-10	-20	3	73	-10	0	20	3
25	0	0	-20	3	74	0	0	20	3
26	0	10	-20	3	75	10	0	20	3
27	0	20	-20	3	76	20	0	20	3
28	0	50	-20	3	77	50	0	20	3
29	-50	0	-10	3	78	0	-50	20	3
30	-20	0	-10	3	79	0	-20	20	3
31	-10	0	-10	3	80	0	-10	20	3
32	0	0	-10	3	81	0	0	20	3
33	10	0	-10	3	82	0	10	20	3
34	20	0	-10	3	83	0	20	20	3
35	50	0	-10	3	84	0	50	20	3
36	0	-50	-10	3	85	-50	0	50	3
37	0	-20	-10	3	86	-20	0	50	3
38	0	-10	-10	3	87	-10	0	50	3
39	0	0	-10	3	88	0	0	50	3
40	0	10	-10	3	89	10	0	50	3
41	0	20	-10	3	90	20	0	50	3
42	0	50	-10	3	91	50	0	50	3
43	-50	0	0	3	92	0	-50	50	3
44	-20	0	0	3	93	0	-20	50	3
45	-10	0	0	3	94	0	-10	50	3
46	0	0	0	3	95	0	0	50	3
47	10	0	0	3	96	0	10	50	3
48	20	0	0	3	97	0	20	50	3
49	50	0	0	3	98	0	50	50	3

Table B.2: Sequence of positions used for the traversing machine in the experiment with a ^{198}Au source at fixed positions in air.

#	x' (mm)	y' (mm)	z' (mm)	t (s)	#	x' (mm)	y' (mm)	z' (mm)	t (s)	#	x' (mm)	y' (mm)	z' (mm)	t (s)
1	-75	0	-75	1	41	-75	0	-35	1	81	-75	0	-20	1
2	-50	0	-75	1	42	-50	0	-35	1	82	-50	0	-20	1
3	-35	0	-75	1	43	-35	0	-35	1	83	-35	0	-20	1
4	-20	0	-75	1	44	-20	0	-35	1	84	-20	0	-20	1
5	-10	0	-75	1	45	-10	0	-35	1	85	-10	0	-20	1
6	0	0	-75	1	46	0	0	-35	1	86	0	0	-20	1
7	10	0	-75	1	47	10	0	-35	1	87	10	0	-20	1
8	20	0	-75	1	48	20	0	-35	1	88	20	0	-20	1
9	35	0	-75	1	49	35	0	-35	1	89	35	0	-20	1
10	50	0	-75	1	50	50	0	-35	1	90	50	0	-20	1
11	0	-75	-75	1	51	0	-75	-35	1	91	0	-75	-20	1
12	0	-50	-75	1	52	0	-50	-35	1	92	0	-50	-20	1
13	0	-35	-75	1	53	0	-35	-35	1	93	0	-35	-20	1
14	0	-20	-75	1	54	0	-20	-35	1	94	0	-20	-20	1
15	0	-10	-75	1	55	0	-10	-35	1	95	0	-10	-20	1
16	0	0	-75	1	56	0	0	-35	1	96	0	0	-20	1
17	0	10	-75	1	57	0	10	-35	1	97	0	10	-20	1
18	0	20	-75	1	58	0	20	-35	1	98	0	20	-20	1
19	0	35	-75	1	59	0	35	-35	1	99	0	35	-20	1
20	0	50	-75	1	60	0	50	-35	1	100	0	50	-20	1
21	-75	0	-50	1	61	-75	0	-25	1	101	-75	0	-10	1
22	-50	0	-50	1	62	-50	0	-25	1	102	-50	0	-10	1
23	-35	0	-50	1	63	-35	0	-25	1	103	-35	0	-10	1
24	-20	0	-50	1	64	-20	0	-25	1	104	-20	0	-10	1
25	-10	0	-50	1	65	-10	0	-25	1	105	-10	0	-10	1
26	0	0	-50	1	66	0	0	-25	1	106	0	0	-10	1
27	10	0	-50	1	67	10	0	-25	1	107	10	0	-10	1
28	20	0	-50	1	68	20	0	-25	1	108	20	0	-10	1
29	35	0	-50	1	69	35	0	-25	1	109	35	0	-10	1
30	50	0	-50	1	70	50	0	-25	1	110	50	0	-10	1
31	0	-75	-50	1	71	0	-75	-25	1	111	0	-75	-10	1
32	0	-50	-50	1	72	0	-50	-25	1	112	0	-50	-10	1
33	0	-35	-50	1	73	0	-35	-25	1	113	0	-35	-10	1
34	0	-20	-50	1	74	0	-20	-25	1	114	0	-20	-10	1
35	0	-10	-50	1	75	0	-10	-25	1	115	0	-10	-10	1
36	0	0	-50	1	76	0	0	-25	1	116	0	0	-10	1
37	0	10	-50	1	77	0	10	-25	1	117	0	10	-10	1
38	0	20	-50	1	78	0	20	-25	1	118	0	20	-10	1
39	0	35	-50	1	79	0	35	-25	1	119	0	35	-10	1
40	0	50	-50	1	80	0	50	-25	1	120	0	50	-10	1

Continuation Table B.2.

#	x' (mm)	y' (mm)	z' (mm)	t (s)	#	x' (mm)	y' (mm)	z' (mm)	t (s)	#	x' (mm)	y' (mm)	z' (mm)	t (s)
121	-75	0	0	1	161	-75	0	20	1	201	-75	0	50	1
122	-50	0	0	1	162	-50	0	20	1	202	-50	0	50	1
123	-35	0	0	1	163	-35	0	20	1	203	-35	0	50	1
124	-20	0	0	1	164	-20	0	20	1	204	-20	0	50	1
125	-10	0	0	1	165	-10	0	20	1	205	-10	0	50	1
126	0	0	0	1	166	0	0	20	1	206	0	0	50	1
127	10	0	0	1	167	10	0	20	1	207	10	0	50	1
128	20	0	0	1	168	20	0	20	1	208	20	0	50	1
129	35	0	0	1	169	35	0	20	1	209	35	0	50	1
130	50	0	0	1	170	50	0	20	1	210	50	0	50	1
131	0	-75	0	1	171	0	-75	20	1	211	0	-75	50	1
132	0	-50	0	1	172	0	-50	20	1	212	0	-50	50	1
133	0	-35	0	1	173	0	-35	20	1	213	0	-35	50	1
134	0	-20	0	1	174	0	-20	20	1	214	0	-20	50	1
135	0	-10	0	1	175	0	-10	20	1	215	0	-10	50	1
136	0	0	0	1	176	0	0	20	1	216	0	0	50	1
137	0	10	0	1	177	0	10	20	1	217	0	10	50	1
138	0	20	0	1	178	0	20	20	1	218	0	20	50	1
139	0	35	0	1	179	0	35	20	1	219	0	35	50	1
140	0	50	0	1	180	0	50	20	1	220	0	50	50	1
141	-75	0	10	1	181	-75	0	35	1	221	-75	0	75	1
142	-50	0	10	1	182	-50	0	35	1	222	-50	0	75	1
143	-35	0	10	1	183	-35	0	35	1	223	-35	0	75	1
144	-20	0	10	1	184	-20	0	35	1	224	-20	0	75	1
145	-10	0	10	1	185	-10	0	35	1	225	-10	0	75	1
146	0	0	10	1	186	0	0	35	1	226	0	0	75	1
147	10	0	10	1	187	10	0	35	1	227	10	0	75	1
148	20	0	10	1	188	20	0	35	1	228	20	0	75	1
149	35	0	10	1	189	35	0	35	1	229	35	0	75	1
150	50	0	10	1	190	50	0	35	1	230	50	0	75	1
151	0	-75	10	1	191	0	-75	35	1	231	0	-75	75	1
152	0	-50	10	1	192	0	-50	35	1	232	0	-50	75	1
153	0	-35	10	1	193	0	-35	35	1	233	0	-35	75	1
154	0	-20	10	1	194	0	-20	35	1	234	0	-20	75	1
155	0	-10	10	1	195	0	-10	35	1	235	0	-10	75	1
156	0	0	10	1	196	0	0	35	1	236	0	0	75	1
157	0	10	10	1	197	0	10	35	1	237	0	10	75	1
158	0	20	10	1	198	0	20	35	1	238	0	20	75	1
159	0	35	10	1	199	0	35	35	1	239	0	35	75	1
160	0	50	10	1	200	0	50	35	1	240	0	50	75	1

C

Rotational speeds of rotator

Table C.1: The rotational speeds of the rotator with the corresponding tangential velocities for the different radii together with the measuring time and the number of rotations for which are measured in the experiment with the source moving along a known circular trajectory.

R (mm)	10.3	Rotational speed (rpm)	32	48	64	96	113	162	211	324	418
		Tangential velocity (mm/s)	35	52	69	104	122	175	228	349	451
		Measuring time (s)	20	13	10	7	6	5	5	5	5
		Number of rotations (-)	10.7	10.4	10.7	11.2	11.3	13.5	17.6	27.0	34.8
	19.4	Rotational speed (rpm)			34	51	60	86	112	172	222
		Tangential velocity (mm/s)			69	104	122	175	228	349	451
		Measuring time (s)			19	13	11	8	6	5	5
		Number of rotations (-)			10.8	11.1	11.0	11.5	11.2	14.3	18.5
	38.8	Rotational speed (rpm)					30	43	56	86	111
		Tangential velocity (mm/s)					122	175	228	349	451
		Measuring time (s)					21	15	12	8	6
		Number of rotations (-)					10.5	10.8	11.2	11.5	11.1

D

Rotational speeds of stirrer

Table D.1: The rotational speeds of the stirrer with the corresponding velocities of the tip of the blades and the *Re* for which are measured for 60 s in the experiment with the source moving freely in a stirred tank.

N (rpm)	180	240	300	360	420	480	540
v (m/s)	0.15	0.20	0.25	0.29	0.34	0.39	0.44
Re (-)	$7.2 \cdot 10^3$	$9.6 \cdot 10^3$	$1.2 \cdot 10^4$	$1.4 \cdot 10^4$	$1.7 \cdot 10^4$	$1.9 \cdot 10^4$	$2.2 \cdot 10^4$

E

Geometry of the setup

Table E.1: Sequence of positions used for the traversing machine in the experiment with a ^{57}Co source at fixed positions in air.

Line	Measured distance (mm)	Reconstructed distance (mm)	Deviation (mm)
R1L2	346.3	345.3	1
R2L3	338.3	339.3	1
R3L1	333.3	337.4	4.1
L1C	272	275	3
L2C	287	284	3
L3C	278	281	3
R1C	290	287	3
R2C	290	291	1
R3C	293	290	3
R1L1	225	225	0
R2L2	225	225	0
R3L3	225	225	0
R1L3	565	564.2	0.8
R2L1	566	562.7	3.3
R3L2	575	569.2	5.8
L1L2	492	487.9	4.1
L1L3	482	480.7	1.3
L2L3	488	486.3	1.7
R1R2	502	501.7	0.3
R1R3	501	500.7	0.3
R2R3	503	500.9	2.1

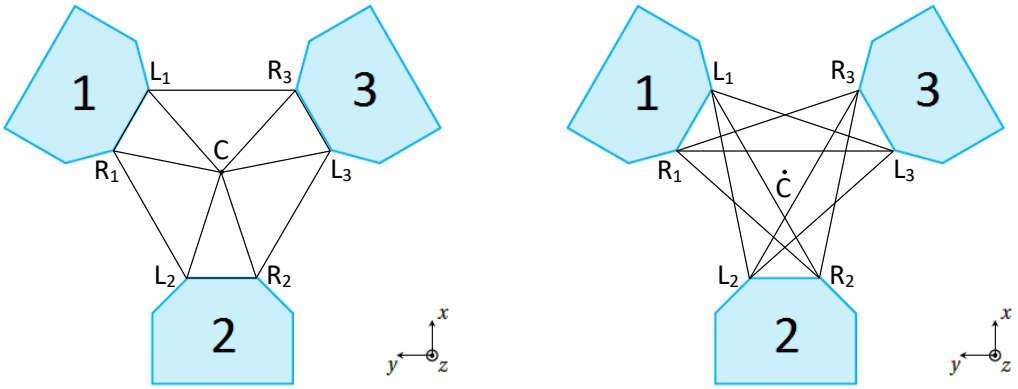

Figure E.1: Measured distances to obtain the geometry of the setup. The ones on the left are used to reconstruct the geometry and the ones on the right are used as an additional check.

F

More elaborate results

F.1. Fixed positions

F.1.1. Maximum time frame length

^{57}Co source

Table F.1: The total error made in the reconstruction of the 49 positions along the x'-axis of the ^{57}Co source of 3.2 MBq at different z'-positions.

z' [mm] \ x' [mm]	-50	-20	-10	0	10	20	50
-50	1.75	0.396	0.232	0.432	0.629	1.03	1.74
-20	1.99	0.652	0.324	0.240	0.520	0.800	1.59
-10	2.14	0.815	0.461	0.307	0.479	0.733	1.51
0	1.94	2.51	4.45	0.0344	0.728	1.25	2.54
10	2.16	0.696	0.358	0.285	0.333	0.701	1.45
20	2.01	0.768	0.473	0.271	0.334	0.509	1.29
50	2.24	0.979	0.651	0.430	0.193	0.429	1.20

Table F.2: The total error made in the reconstruction of the 49 positions along the y'-axis of the ^{57}Co source of 3.2 MBq at different z'-positions.

z' [mm] \ y' [mm]	-50	-20	-10	0	10	20	50
-50	1.43	0.728	0.513	0.450	0.327	0.246	0.583
-20	1.25	0.563	0.454	0.290	0.0686	0.119	0.558
-10	1.22	0.581	0.462	0.347	0.182	0.161	0.506
0	1.15	0.402	0.137	0.0344	0.683	0.635	0.487
10	1.78	0.729	0.453	0.245	0.148	0.136	0.671
20	1.35	0.651	0.390	0.299	0.181	0.205	0.651
50	1.00	0.503	0.444	0.259	0.351	0.345	0.650

Table F.3: The horizontal error made in the reconstruction of the 49 positions along the x'-axis of the ^{57}Co source of 3.2 MBq at different z'-positions.

z' [mm] \ x' [mm]	-50	-20	-10	0	10	20	50
-50	1.65	0.300	0.0115	0.403	0.625	1.02	1.74
-20	1.82	0.537	0.193	0.0719	0.511	0.792	1.59
-10	1.90	0.535	0.152	0.0806	0.431	0.727	1.50
0	1.94	0.614	0.392	0.0301	0.258	0.571	1.34
10	2.09	0.623	0.261	0.114	0.224	0.609	1.34
20	1.90	0.681	0.372	0.0906	0.221	0.435	1.24
50	2.16	0.944	0.638	0.416	0.180	0.421	1.17

Table F.4: The horizontal error made in the reconstruction of the 49 positions along the y'-axis of the ^{57}Co source of 3.2 MBq at different z'-positions.

z' [mm] \ y' [mm]	-50	-20	-10	0	10	20	50
-50	0.950	0.478	0.415	0.420	0.326	0.195	0.291
-20	0.733	0.214	0.284	0.186	0.0667	0.0915	0.350
-10	0.690	0.0983	0.101	0.218	0.0516	0.160	0.346
0	0.622	0.111	0.0254	0.0301	0.123	0.135	0.462
10	0.529	0.0915	0.0374	0.128	0.135	0.120	0.612
20	0.332	0.179	0.0374	0.128	0.138	0.201	0.574
50	0.179	0.292	0.349	0.210	0.351	0.339	0.604

Table F.5: The vertical error made in the reconstruction of the 49 positions along the x'-axis of the ^{57}Co source of 3.2 MBq at different z'-positions.

z' [mm] \ x' [mm]	-50	-20	-10	0	10	20	50
-50	0.582	0.258	0.232	0.157	0.0698	0.0935	0.0532
-20	0.791	0.369	0.260	0.229	0.0956	0.111	0.0301
-10	0.993	0.615	0.435	0.296	0.209	0.0887	0.181
0	0.109	2.43	4.43	0.0167	0.681	1.11	2.16
10	0.521	0.312	0.246	0.261	0.247	0.346	0.537
20	0.646	0.353	0.291	0.255	0.251	0.263	0.361
50	0.583	0.259	0.131	0.109	0.0695	0.0835	0.253

Table F.6: The vertical error made in the reconstruction of the 49 positions along the y'-axis of the ^{57}Co source of 3.2 MBq at different z'-positions.

z' [mm] \ y' [mm]	-50	-20	-10	0	10	20	50
-50	1.07	0.550	0.301	0.163	0.0279	0.150	0.505
-20	1.01	0.520	0.354	0.222	0.0157	0.0757	0.435
-10	1.01	0.573	0.451	0.270	0.175	0.0127	0.368
0	0.972	0.387	0.135	0.0167	0.672	0.620	0.154
10	1.70	0.723	0.452	0.209	0.0598	0.0644	0.276
20	1.31	0.626	0.389	0.270	0.116	0.0418	0.308
50	0.989	0.410	0.274	0.153	0.0154	0.0630	0.240

^{198}Au source

Table F.7: The total error made in the reconstruction of the 120 positions along the x'-axis of the ^{198}Au source of 69 MBq at different z'-positions.

z' [mm] \ x' [mm]	-75	-50	-35	-20	-10	0	10	20	35	50
-75	3.33	1.77	1.18	0.759	0.536	0.395	0.889	1.04	2.06	2.54
-50	3.99	2.70	1.06	0.150	0.174	0.400	1.20	1.12	1.91	2.24
-35	3.65	2.16	1.61	0.586	0.689	0.526	0.914	1.36	2.52	2.32
-25	3.58	2.18	2.26	1.06	0.896	0.712	0.714	1.52	1.64	2.27
-20	3.86	2.36	1.77	1.32	0.676	1.10	1.10	1.54	1.92	1.76
-10	4.33	2.48	1.70	0.564	0.957	0.407	1.37	1.31	1.76	2.17
0	3.71	2.13	1.26	0.126	0.375	0.102	1.19	1.17	1.80	2.30
10	3.64	1.74	1.92	0.969	0.501	0.884	0.523	0.549	1.00	1.78
20	3.67	2.53	1.76	1.04	0.969	1.04	0.898	1.07	1.06	2.43
35	4.21	2.69	1.86	1.13	0.523	0.846	0.721	1.10	1.27	1.26
50	3.92	2.97	1.30	0.800	0.754	0.565	0.461	0.346	1.30	1.94
75	3.90	2.79	2.39	1.63	0.468	0.679	0.721	0.754	0.871	1.60

Table F.8: The total error made in the reconstruction of the 120 positions along the y'-axis of the ^{198}Au source of 69 MBq at different z'-positions.

z' [mm] \ y' [mm]	-75	-50	-35	-20	-10	0	10	20	35	50
-75	2.37	1.89	0.690	0.874	0.598	0.687	1.15	1.08	0.913	0.692
-50	2.86	1.39	0.711	0.797	0.839	0.807	1.38	0.758	1.06	1.05
-35	2.26	1.51	0.742	0.812	0.964	0.560	0.937	0.566	0.489	1.30
-25	2.83	1.94	1.67	1.30	0.860	0.428	0.650	0.850	0.390	0.409
-20	2.51	1.92	1.03	1.36	1.42	1.15	1.13	0.796	0.730	0.488
-10	1.72	1.59	1.26	1.31	0.607	0.638	0.530	0.302	0.671	0.165
0	1.84	0.523	0.398	0.331	0.658	0.102	1.34	0.443	0.961	0.758
10	4.48	1.99	2.20	0.655	1.16	0.463	0.830	0.612	0.775	0.393
20	2.79	2.00	1.46	1.46	0.631	1.01	0.582	1.03	0.324	1.13
35	2.73	1.80	1.25	1.29	0.983	1.16	0.676	0.417	0.574	0.927
50	2.26	1.16	1.34	0.330	0.701	0.451	0.346	0.217	0.217	0.726
75	1.94	1.91	1.64	1.21	1.06	0.923	0.525	0.876	0.946	1.16

Table F.9: The horizontal error made in the reconstruction of the 120 positions along the x'-axis of the ^{198}Au source of 69 MBq at different z'-positions.

z' [mm] \ x' [mm]	-75	-50	-35	-20	-10	0	10	20	35	50
-75	3.22	1.77	1.18	0.633	0.445	0.348	0.830	1.04	1.93	2.48
-50	3.90	2.66	1.04	0.150	0.172	0.365	1.19	1.03	1.88	2.22
-35	3.52	1.98	1.60	0.574	0.689	0.254	0.912	1.27	2.43	2.31
-25	3.40	2.02	2.15	0.745	0.632	0.640	0.712	1.47	1.49	2.21
-20	3.67	2.01	1.42	0.366	0.294	0.522	0.685	1.24	1.60	1.73
-10	4.06	2.29	1.47	0.373	0.536	0.390	1.07	1.17	1.68	2.16
0	3.62	2.09	1.19	0.106	0.370	0.0792	0.725	0.978	1.58	1.56
10	3.61	1.74	1.92	0.955	0.440	0.283	0.447	0.545	0.891	1.70
20	3.20	1.96	1.61	0.756	0.528	0.419	0.305	0.680	0.919	2.34
35	3.69	2.21	1.33	0.0920	0.331	0.351	0.439	0.512	1.10	1.24
50	3.40	2.74	1.25	0.799	0.673	0.463	0.109	0.286	1.00	1.59
75	3.62	2.58	1.76	0.832	0.265	0.501	0.620	0.220	0.725	1.54

Table F.10: The horizontal error made in the reconstruction of the 120 positions along the y'-axis of the ^{198}Au source of 69 MBq at different z'-positions.

z' [mm] \ y' [mm]	-75	-50	-35	-20	-10	0	10	20	35	50
-75	2.17	1.53	0.591	0.749	0.596	0.684	0.919	0.685	0.680	0.142
-50	2.57	1.31	0.673	0.787	0.761	0.715	1.10	0.499	0.695	0.717
-35	1.95	1.48	0.706	0.811	0.925	0.507	0.933	0.521	0.459	0.616
-25	2.20	1.34	0.815	0.636	0.452	0.251	0.577	0.251	0.141	0.401
-20	1.35	1.28	0.303	0.900	0.676	0.511	0.687	0.547	0.368	0.432
-10	1.28	0.909	0.443	0.753	0.0170	0.579	0.395	0.208	0.325	0.109
0	1.71	0.383	0.336	0.253	0.614	0.079	0.676	0.411	0.305	0.511
10	1.98	0.739	0.496	0.442	0.289	0.437	0.830	0.604	0.0516	0.370
20	1.79	0.989	0.0325	0.135	0.142	0.248	0.206	0.599	0.305	1.13
35	2.20	1.02	0.573	0.676	0.387	0.635	0.203	0.103	0.548	0.923
50	1.43	0.659	0.422	0.0774	0.459	0.403	0.120	0.209	0.211	0.677
75	1.31	0.643	0.351	0.567	0.669	0.292	0.240	0.216	0.507	1.03

Table F.11: The vertical error made in the reconstruction of the 120 positions along the x'-axis of the ^{198}Au source of 69 MBq at different z'-positions.

z' [mm] \ x' [mm]	-75	-50	-35	-20	-10	0	10	20	35	50
-75	0.844	0.0194	0.0720	0.418	0.300	0.187	0.320	0.0835	0.697	0.569
-50	0.823	0.439	0.159	0.00633	0.0209	0.164	0.0608	0.441	0.295	0.303
-35	1.00	0.864	0.128	0.117	0.0133	0.460	0.0713	0.470	0.644	0.258
-25	1.14	0.828	0.726	0.759	0.635	0.312	0.0541	0.401	0.690	0.527
-20	1.20	1.24	1.05	1.26	0.608	0.972	0.857	0.904	1.07	0.354
-10	1.53	0.949	0.838	0.424	0.794	0.115	0.848	0.597	0.529	0.152
0	0.809	0.418	0.418	0.0688	0.0610	0.0636	0.941	0.649	0.867	1.68
10	0.427	0.0754	0.0598	0.162	0.240	0.837	0.271	0.061	0.456	0.536
20	1.78	1.60	0.717	0.714	0.813	0.953	0.845	0.826	0.521	0.620
35	2.02	1.53	1.30	1.12	0.405	0.770	0.573	0.977	0.631	0.255
50	1.94	1.14	0.337	0.0386	0.340	0.324	0.448	0.194	0.837	1.10
75	1.43	1.04	1.62	1.40	0.385	0.458	0.368	0.721	0.483	0.413

Table F.12: The vertical error made in the reconstruction of the 120 positions along the y'-axis of the ^{198}Au source of 69 MBq at different z'-positions.

z' [mm] \ y' [mm]	-75	-50	-35	-20	-10	0	10	20	35	50
-75	0.940	1.10	0.357	0.450	0.0418	0.0662	0.695	0.842	0.610	0.677
-50	1.24	0.470	0.227	0.122	0.353	0.373	0.830	0.571	0.795	0.769
-35	1.14	0.268	0.231	0.0365	0.271	0.236	0.0871	0.222	0.170	1.14
-25	1.79	1.41	1.46	1.13	0.731	0.347	0.298	0.813	0.363	0.0829
-20	2.11	1.44	0.983	1.01	1.25	1.02	0.901	0.579	0.631	0.227
-10	1.15	1.30	1.18	1.08	0.606	0.267	0.353	0.219	0.587	0.124
0	0.684	0.356	0.213	0.213	0.239	0.0636	1.15	0.166	0.911	0.560
10	4.01	1.85	2.14	0.484	1.12	0.154	0.0260	0.0962	0.773	0.134
20	2.14	1.74	1.46	1.46	0.614	0.984	0.544	0.843	0.111	0.0626
35	1.62	1.48	1.11	1.10	0.903	0.976	0.645	0.405	0.171	0.0907
50	1.75	0.953	1.27	0.321	0.530	0.202	0.325	0.0601	0.0518	0.262
75	1.43	1.79	1.60	1.07	0.817	0.876	0.467	0.849	0.798	0.545

Bibliography

[1] S. Bechan. Multi-particle tracking using spect. Master's thesis, Delft University of Technology, Delft, 2016.

[2] T.J. Chung. *General Continuum Mechanics*. Cambridge Universiy Press, Cambridge, 2007.

[3] C.J. Elkins and M.T. Alley. Magnetic resonance velocimetry: applications of magnetic resonance imaging in the measurement of fluid motion. *Experiments in Fluids*, 43:823–858, 2007.

[4] R. Fishwick, M. Winterbottom, D. Parker, X. Fan, and H. Stitt. The use of positron emission particle tracking in the study of multiphase stirred tank reactor hydrodynamics. *The Canadian Journal of Chemical Engineering*, 83:97–103, 2005.

[5] I. Fogelman, G. Gnanasegaran, and H. Van der Wall. *Radionuclide and Hybrid Bone Imaging*. Springer-Verlag Berlin Heidelberg, Heidelberg, 2012.

[6] G.R. Gilmore. *Practical Gamma-ray Spectrometry*. John Wiley & Sons, Chichester, 2nd edition, 2008.

[7] N. Harnby, M.F. Edwards, and A.W. Nienow. *Mixing in the Process Industries*. Elsevier Science & Technology, Amsterdam, 1992.

[8] G.V. Heller and R.C. Hendel. *Handbook of Nuclear Cardiology*. Springer-Verlag London, London, 2013.

[9] K. Herrmann, O.E. Nieweg, and S.P. Povoski. *Radioguided Surgery*. Springer International Publishing Switzerland, Basel, 2016.

[10] C.H. Holbrow, J.N. Lloyd J.C. Amato, E. Galvez, and M.E. Parks. *Modern Introductory Physics*. Springer Science+Business Media, Dordrecht, 2nd edition, 2010.

[11] J.H. Hubbell. *Photon cross section, attenuation coefficients and energy absorption coefficients from 10 keV to 100 GeV*. National Bureau of Standards, Washington, D.C., 1969.

[12] S.A. Huijs. X-ray particle tracking velocimetry: Assessment of applicability. Master's thesis, Delft University of Technology, Delft, 2017.

[13] M. Jahanmiri. Particle image velocimetry: Fundamentals and its applications. Technical report, Chalmers University of Technology, Göteborg, 2011.

[14] L.P.B.M. Janssen and M.M.C.G. Warmoeskerken. *Transport Phenomena Data Companion*. VSSD, Delft, 3rd edition, 2006.

[15] G.R. Kasat and A.B. Pandit. Review on mixing characteristics in solid- liquid and solid-liquid-gas reactor vessels. *The Canadian Journal of Chemical Engineering*, 83:618–643, 2005.

[16] H. Kato. Production of gold-198 grains. *Gold Bulletin*, 11(3):86–87, 1978.

[17] M.F. L'Annunziata. *Radioactivity - Introduction and History*. Elsevier Science & Technology, Amsterdam, 2007.

[18] K.C. Lee and M. Yianneskis. Turbulence properties of the impeller stream of a rushton turbine. *AIChE Journal*, 44(1):13–24, 1998.

[19] W. Lu and H. Chen. Flooding and critical impeller speed for gas dispersion in aerated turbine-agitated vessels. *The Chemical Engineering Journal*, 33:57–62, 1985.

[20] E.E. Michaelides, C.T. Crowe, and J.D. Schwarzkopf. *Multiphase Flow Handbook*. CRC Press, Boca Raton, 2nd edition, 2016.

[21] MiLabs. *Construction drawings*. MiLabs, 2012.

[22] A.W. Nienow. Hydrodynamics of stirred bioreactors. *Applied Mechanics Reviews*, 51(1):3–32, 1998.

[23] NIST. X-ray mass attenuation coefficients, 2004. URL `https://www.nist.gov/`.

[24] R. Noordman. Setting up spect measurements tracking particles inside fluidized beds. Master's thesis, Delft University of Technology, Delft, 2014.

[25] ORTEC. *Managing Dead Time Errors in Gamma-Ray Spectroscopy*. AZoM, Manchester, 2017.

[26] Photonis. *Photomultiplier tubes basics*. Photonis, 2010.

[27] E.B. Podgoršak. *Radiation Physics for Medical Physicists*. Springer International Publishing Switzerland, Basel, 3rd edition, 2016.

[28] B. Sokoray-Varga and J. Józsa. Particle tracking velocimetry (ptv) and its application to analyse free surface flows in laboratory scale models. *Periodica Polytechnica Civil Engineering*, 52(2):63–71, 2008.

[29] G.P. Towler and R.K. Sinnott. *Chemical engineering design: principles, practice, and economics of plant and process design*. Elsevier Science & Technology, Amsterdam, 2nd edition, 2012.

[30] C. Tropea. Laser doppler velocimetry. *Encyclopedia of Aerospace Engineering*, 2010.

[31] C. Tropea, A.L. Yarin, and J.F. Foss. *Springer Handbook of Experimental Fluid Mechanics*. Springer-Verlag Berlin Heidelberg, Heidelberg, 2007.

[32] R. Wolfson. *Essential University Physics*, volume 2. Pearson Education, San Francisco, 2nd edition, 2012.

[33] Th.N. Zwietering. Suspending of solid particles in liquid by agitators. *Chemical Engineering Science*, 8: 244–253, 1958.